UC San Diego
UC San Diego Electronic Theses and Dissertations

Title

Molecular Beam Epitaxy of Dilute Nitride GaNAsP as Intermediate Band Solar Cell Materials /

Permalink

https://escholarship.org/uc/item/69g4884j

Author

Kuang, Yanjin

Publication Date

2014

Peer reviewed|Thesis/dissertation

UNIVERSITY OF CALIFORNIA, SAN DIEGO

Molecular Beam Epitaxy of Dilute Nitride GaNAsP as Intermediate Band Solar Cell Materials

A dissertation submitted in partial satisfaction of the
requirements for the degree
Doctor of Philosophy

in

Physics

by

Yanjin Kuang

Committee in charge:

Professor Charles W. Tu, Chair
Professor Sunil Sinha, Co-Chair
Professor Prabhakar Bandaru
Professor Leonid Butov
Professor Oleg Shpyrko

2014

The dissertation of Yanjin Kuang is approved, and it is acceptable in quality and form for publication on microfilm and electronically:

_____

_____

_____

_____
Co-Chair

_____
Chair

University of California, San Diego

2014

DEDICATION

To Yicong.

EPIGRAPH

Beneath this mask there is an idea.

And ideas are bulletproof.

—V

TABLE OF CONTENTS

LIST OF FIGURES

LIST OF TABLES

ACKNOWLEDGEMENTS

In the past few years, I had the privilege to work with a few collaborators whom I am truly grateful to. I want to sincerely thank Dr. Kin Man Yu and Dr. Wladek Walukiewicz for their measurement on the GaNAsP material and the critical guidance out of the maze on the IBSC device structure. I also thank Dr. Robert Kudrawiec for the optical study on the band structure of GaNAsP. I want to thank Alex Luce for being a very nice and supportive collaborator on the GaNAsP IBSC project. Sincere acknowledgments also goes to Prof. Irina Buyanova, Prof. Weimin Chen and their group members in Sweden for their measurement and insight about the Ga(N)P nanowires. I owe my special thanks to Dr. Ke Sun and Prof. Nathan Lewis in Caltech, who expedited the solar cell device measurement. I also thank Prof. Shadi Dayeh, Dr. Binh-Minh Nguyen and Prof. Bong-Joong Kim for their TEM study on the GaNAsP material system. A very special thank is due to Dr. Paothep Pichanusakorn. The international friendship that started from the GaNAs collaboration has made my life at UCSD more colorful. I would like to acknowledge Prof. Itaru Kamiya and his student Ko Takabayashi for starting the collaboration on the quantum dots project during the summer in 2013. Ko was a very fun lab buddy to work with.

I cannot thank enough my family-like friends in the US. Their company has encouraged and enriched me along this journey.

This thesis could have never been possible without the love and support from my family. My deepest gratitude is beyond words to my parents and parents in law for their understanding. And in retrospect, the burning fire of coming to the US for a PhD degree traces all the way back to the enlightening spark in my childhood from my cousin Angela, to whom I'll be forever indebted to.

Most of all, I would like to thank my wife Yicong for the love, care and passion she brings to life, and for her always company of laughing together, shedding tears together, daydreaming together and above all boating against the current together.

Materials in this dissertation (chapter 3 and Appendix) were partially published in *J. Vac. Sci. Technol. B*, 30, 02B121 (2012), *Appl. Phys. Lett.*, 102,

112105 (2013) and *Appl. Phys. Lett.*, 100, 053108 (2012).

2007	B. S. in Applied Physics, University of Science and Technology of China, Hefei, China
2009	M. S. in Physics, University of California, San Diego
2014	Ph. D. in Physics, University of California, San Diego

PUBLICATIONS

Y.J. Kuang, C.W. Tu, "Silicon dopant passivation by nitrogen during molecular beam epitaxy of GaNAs", submitted.

Y.J. Kuang, K.M. Yu, R. Kudrawiec, A.V. Luce, M. Ting, W. Walukiewicz, and C. W. Tu, "GaNAsP: An intermediate band semiconductor grown by gas-source molecular beam epitaxy, *Appl. Phys. Lett.*, 102, 112105 (2013).

Y.J. Kuang, S. Sukrittanon, H. Li, C.W. Tu, "Growth and photoluminescence of catalyst-free GaP/GaNP core/shell nanowires on Si (111) by gas source molecular beam epitaxy", *Appl. Phys. Lett.*, 100, 053108 (2012).

Y.J. Kuang, S.-W. Chen, H. Li, S.K. Sinha, C.W. Tu, "Growth of $GaN_xAs_yP_{1-x-y}$ alloys on GaP (100) by Gas-source Molecular Beam Epitaxy", *J. Vac. Sci. Technol. B*, 30, 02B121 (2012).

R. Kudrawiec, A. Luce, M. Gladysiewicz, M. Ting, **Y.J. Kuang**, C.W. Tu, O. D. Dubon, K. M. Yu and W. Walukiewicz, "Electronic Band Structure of $GaN_xAs_yP_{1-x-y}$ Highly Mismatched Alloys", submitted.

S. Sukrittanon, **Y.J. Kuang** and C.W. Tu, "Growth and characterization of GaP/GaNP core/shell nanowires", *J. Vac. Sci. Technol. B*, 31, 03C110 (2013).

A. Dobrovolsky, S. Chen, **Y.J. Kuang**, S Sukrittanon, C.W. Tu, W.M. Chen and I.A. Buyanova, "Optical properties of GaP/GaNP core/shell nanowires: a temperature-dependent study", *Nanoscale Res. Lett.*, 8, 239 (2013).

P. Pichanusakorn, **Y.J. Kuang**, C. Patel, C.W. Tu and P.R. Bandaru, "Feasibility of enhancing the thermoelectric power factor in GaNAs", *Phys. Rev. B.*, 86, 085314 (2012).

A. Dobrovolsky, J.E. Stehr, S. L. Chen, **Y.J. Kuang**, S. Sukrittanon, C.W. Tu, W.M. Chen, and I.A. Buyanova, "Mechanism for radiative recombination and defect properties of GaP/GaNP core/shell nanowires", *Appl. Phys. Lett.*, 101, 163106 (2012).

P. Pichanusakorn, **Y.J. Kuang**, C. Patel, C.W. Tu, P.R. Bandaru, "The influence of dopant type and carrier concentration on the effective mass and Seebeck coefficient of GaNAs thin films", *Appl. Phys. Lett.*, 99, 072114 (2011).

PATENTS

US/61/908,342 — Luminescent Nanowire ID Markers and Method for Secured ID of Articles, provisional filing (2013).

CONFERENCE PRESENTATIONS

S. Sukrittanon, **Y. J. Kuang**, C. W. Tu, "Dilute nitride GaNP nanowire growth on Silicon by gas-source molecular beam epitaxy", North American Molecular Beam Epitaxy Conference 2013, Banff, Alberta, Canada.

Y. J. Kuang, K.M. Yu, R. Kudrawiec, A.V. Luce, M. Ting, W. Walukiewicz, and C. W. Tu, "GaNAsP: An Intermediate Band Semiconductor Grown by Gas-Source Molecular Beam Epitaxy", Electronic Materials Conference 2013, South Bend, IN, USA.

A.V. Luce, **Y.J. Kuang**, K.M. Yu, R. Kudrawiec, M. Ting, O. Dubon, C. W. Tu and W. Walukiewicz, "Optical Properties of Highly Mismatched GaNAsP Alloys for Intermediate Band Solar Cell", Electronic Materials Conference 2013, South Bend, IN, USA.

J. E. Stehr, A. Dobrovolsky, **Y.J. Kuang**, S. Sukrittanon, C.W. Tu, W.M. Chen, I.A. Buyanova, "Optically detected magnetic resonance investigation of GaP and GaP/GaNP/GaNP Nanowires", 2013 MRS Fall Meeting, Boston, MA, USA.

A. Dobrovolsky, P. Persson, **Y. J. Kuang**, S. Sukrittanon, C. W. Tu, W. M. Chen, I. A. Buyanova, "Signatures of N incorporation in Raman and optical properties of GaP/GaNP core/shell nanowires", 2013 MRS Fall Meeting, Boston, MA, USA.

A. Dobrovolsky, **Y. J. Kuang**, S. Sukrittanon, C. W. Tu, W. M. Chen, I. A. Buyanova, "Effects of N incorporation on Raman properties and band structure of GaP/GaNP core/shell nanowires", International Conference on One-dimensional nanomaterials 2013, Annecy, France.

Y. J. Kuang, S. Sukrittanon, A. Dobrovolsky, S. Chen, W.M. Chen, I.A. Buyanova and C.W. Tu, "Gas-Source Molecular Beam Epitaxy of GaP/GaNP Core/Shell Nanowires: Growth, Structure Analysis and Optical Properties", North American Molecular Beam Epitaxy Conference 2012, Stone Mountain Park, GA, USA.

Y. J. Kuang, K. M. Yu, <u>C. W. Tu</u>, "Optical properties of intermediate band solar cell material GaNAsP by gas source molecular beam epitaxy", International Conference on Molecular Beam Epitaxy 2012, Nara, Japan.

Y. J. Kuang, S. Sukrittanon, C. W. Tu, "Gas-source molecular beam epitaxy of GaP/GaNP core/shell nanowires: growth, structure analysis and optical properties", International Compound Semiconductor Conference 2012, Santa Barbara, CA, USA.

Y. J. Kuang, K.M. Yu, C.W. Tu, "$GaN_xAs_yP_{1-x-y}$ alloys on GaP (100) by Gas-source Molecular Beam Epitaxy and its intermediate band characteristics", Electronic Materials Conference 2012, State College Park, PA, USA.

Y. J. Kuang, S. Sukrittanon, H. Li, C.W. Tu, "GaP/GaNP core/shell nanowires on Si (111)", North American Molecular Beam Epitaxy 2011, La Jolla, CA, USA.

Y. J. Kuang, S.-W. Chen, H. Li, S.K. Sinha, C.W. Tu, "Growth and characterization of $GaN_xAs_yP_{1-x-y}$ alloys on GaP (100) by Gas-source Molecular Beam Epitaxy", North American Molecular Beam Epitaxy Conference 2011, La Jolla, CA, USA.

Y. J. Kuang, S. Sukrittanon, H. Li, C.W. Tu, "Growth and Photoluminescence of GaP/GaNP Core/Shell Nanowires on Si(111) by Gas-source Molecular Beam Epitaxy", Electronic Materials Conference 2011, Santa Barbara, CA, USA.

<u>P. Pichanusakorn</u>, **Y. J. Kuang**, H. Li, C.J. Patel, C.W. Tu, P.R. Bandaru, "Non-Monotonic Change/Variation in the Seebeck Coefficient of $GaAs_{1-x}N_x$ Thin Film Thermoelectrics Due to the Addition of N (x=0.5% to 1.5%)", Electronic Materials Conference 2011, Santa Barbara, CA, USA.

ABSTRACT OF THE DISSERTATION

Molecular Beam Epitaxy of Dilute Nitride GaNAsP as Intermediate Band Solar Cell Materials

by

Yanjin Kuang

Doctor of Philosophy in Physics

University of California, San Diego, 2014

Professor Charles W. Tu, Chair
Professor Sunil Sinha, Co-Chair

Intermediate band solar cells (IBSC) have been proposed as a promising candidate to exceed the Shockley-Queisser limit of photovoltaic cells and they have caught a lot of attention in the research community. Besides the quantum dot system, highly mismatch alloys (HMAs) such as dilute nitrides, which undergo conduction band splitting during alloying, have been proven as ideal platforms to achieve IBSCs. Dilute nitride GaNAs has been made into IBSC device, but the band spacing in GaNAs cannot meet the limiting efficiency requisite for a 3-band IBSC (63%). By adding P, GaNAsP then falls into the IBSC ultimate efficiency development road-map. This thesis is devoted to the study on the growth of high-

quality GaNAsP and the fabrication and measurement of GaNAsP based IBSCs.

The thesis is divided into two major parts. In the first part, the rationale and the theoretical framework of the GaNAsP material system is laid out. The material compositions that lead to high efficiency is simulated and discussed. GaNAsP material growth by gas-source molecular beam epitaxy is studied. An in situ and ex situ composition control is demonstrated and the metamorphic buffer is characterized by X-ray reciprocal space mapping. Optical properties as well as annealing technique to improve them are investigated. The IB characteristic of GaNAsP is demonstrated by photoreflectance and photoabsorption. In the second part, the general IBSC design principles on GaNAsP is discussed, followed by the bandgap engineering for GaNAsP IBSC device. Particular attentions are paid to important issues, such as Si doping efficiency in dilute nitrides and IB electron blocking, which are the keys of IBSC design. An iteration on optimizing the IBSC deice structure has been run and the measurement and evaluations on these IBSC devices are presented. GaNAsP IBSCs with an open circuit voltage as high as 1.2 V and a fill factor of 0.66 have been obtained, which are the highest reported to date for HMA based IBSC.

1 Introduction

Kuafu cherished a great ambition,

He then competed with the sun in a race.

—Tao Yuanming

1.1 The needs for higher efficiency solar cells

The energy consumption of mankind grows as the economic activities and industrial development grow along with the world population. Our energy consumption is monopolistically dominated by fossil fuels (figure 1.1)[1]. However, many studies suggest that the peak of oil and coal production is happening or has already happened and an exhaustion phase of oil will follow. A civilization with a continuously growing demand for energy that depends heavily on a limited and non-renewable energy source is not sustainable. Moreover, the air emission during the burning of fossil fuels is problematic and causes environmental issues. The greenhouse gases concentration, mainly carbon dioxide, has been sharply increasing since the industrial revolution. The positive correlation between greenhouse gases concentration in the atmosphere and global warming is backed by a considerable amount of scientific studies. Power generation from nuclear fission has been introduced and deployed for several decades. However, the limited reserve of Uranium and the recent Fukushima incident have placed a shadow and uncertainty on nuclear utilities. Therefore, the quest beyond fossil for alternative energy for mankind is a must. And the answer is the sun.

The power received by the earth from the sun is around 6000 times our present consumption [1] and if it can be converted to usable power in an efficient

Renewable

Biomass	9.30%
Bio-heat	3.78%
Bio-power generation	0.35%
Wind power	0.56%
Solar PV	0.08%
Solar CSP	0.004%
Ocean power	0.001%
Geothermal electricity	0.07%
Hydropower	3.73%
Solar hotwater	0.22%
Geothermal heat	0.14%
Ethanol	0.55%
Biodiesel	0.23%

Total World Energy Consumption by Source (2011)

Total

Fossil	78.2%
Nuclear	2.8%
Renewable	19.0%
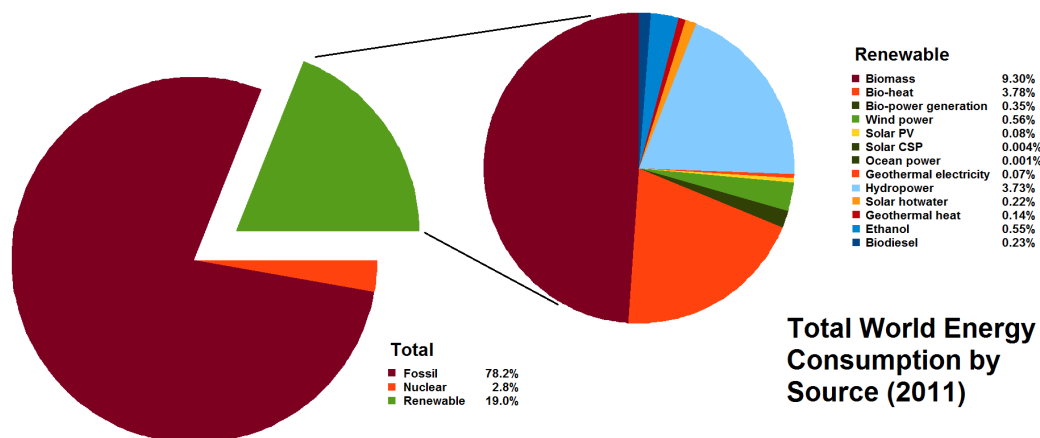
Figure 1.1: Breakdown of the world total energy consumption.

way, the global energy crisis can be solved. Biomass comprises a big share in renewable energy sector but it falls into the low conversion efficiency regime. In fact, if the global energy consumption were to be replaced solely by solar energy, the conversion efficiency would have to be higher than 0.02% to sustain the current amount of consumption. But taking into account that not all sun power received by the earth is convertible, the efficiency has to be a lot higher as a sustainable source.

In contrary to the low power conversion efficiency of biomass and wind power, photovoltaic (PV) can provide high efficiency needed. The higher efficiency from PV has made it an ideal candidate for renewable energy. Its advantages also come from its capability of distributed electricity generation. Isolated homes, buildings in rural areas, remote electronics and so forth can all be powered by PV. The small share of PV in the total energy consumption comes mainly from its cost. PV plants take up a considerable amount of land and the period of return on investment is fairly long. Given the same amount of land for PV plants, PV with higher conversion efficiency has an obvious advantage with higher energy output per unit land occupied. And it is predicted that the 3rd generation of PV with efficiency higher than 38% would drive down the cost a lot [2].

1.2 Solar cell conversion limit

Similar to the Carnot efficiency of thermal engine, there is a theoretical limit on how much sun light a solar power converter can achieve. However, the calculation is not simply done by assigning the sun temperature and ambient temperature to the Carnot equation, because a solar converter also emits radiation governed by the Planck law. Landsberg and Tonge [3] has calculated the thermal dynamic limit on efficiency for a solar converter when the device produces zero entropy and emits its radiation to the sun,

$$\eta_{Landsberg} = 1 - \frac{4}{3}(\frac{T_{ambient}}{T_{sun}}) + \frac{1}{3}(\frac{T_{ambient}}{T_{sun}})^4. \tag{1.1}$$

If 6000K and 300K were assigned to the sun and ambient temperature, the thermal dynamic limit on efficiency is 93.33% instead of 95% given by the Carnot equation.

When a semiconductor is used to fabricate a solar cell, its valence band and conduction band are used as two energy levels to store the chemical potentials and its p-n junction asymmetry is used as the major photon-generated electron-hole pair separation mechanism. Back in 1960s, Shockley and Queisser calculated the limit on solar cell efficiency by a detailed balance model [4]. As mentioned above, a solar cell not only convert solar radiation into electricity it also emits light. Shockley and Queisser elegantly avoided the tedious and laborious calculation to account for the micro processes of electrons and holes inside the semiconductor. Instead, they argued that the major carrier recombination processes could be accounted for by calculating the black body radiation from the solar cell under equilibrium. They assumed infinite mobility and all non-radiative recombination process are suppressed and that radiative recombination is only produced by radiation that escapes by the cell surface. Under these assumptions, the efficiency limit on a semiconductor solar cell was calculated to be around 33%. Figure 1.2 shows how the sun light energy goes for semiconductors with different bandgap energies. The green region at the bottom represents the sunlight energy portion that is converted to usable electricity. It increases as bandgap energy goes from 0.4 eV to about 1.2 eV then declines afterwards. There are two reasons for the limit on a single bandgap semiconductor solar cell even if it is ideal. The first is that those sub-bandgap pho-
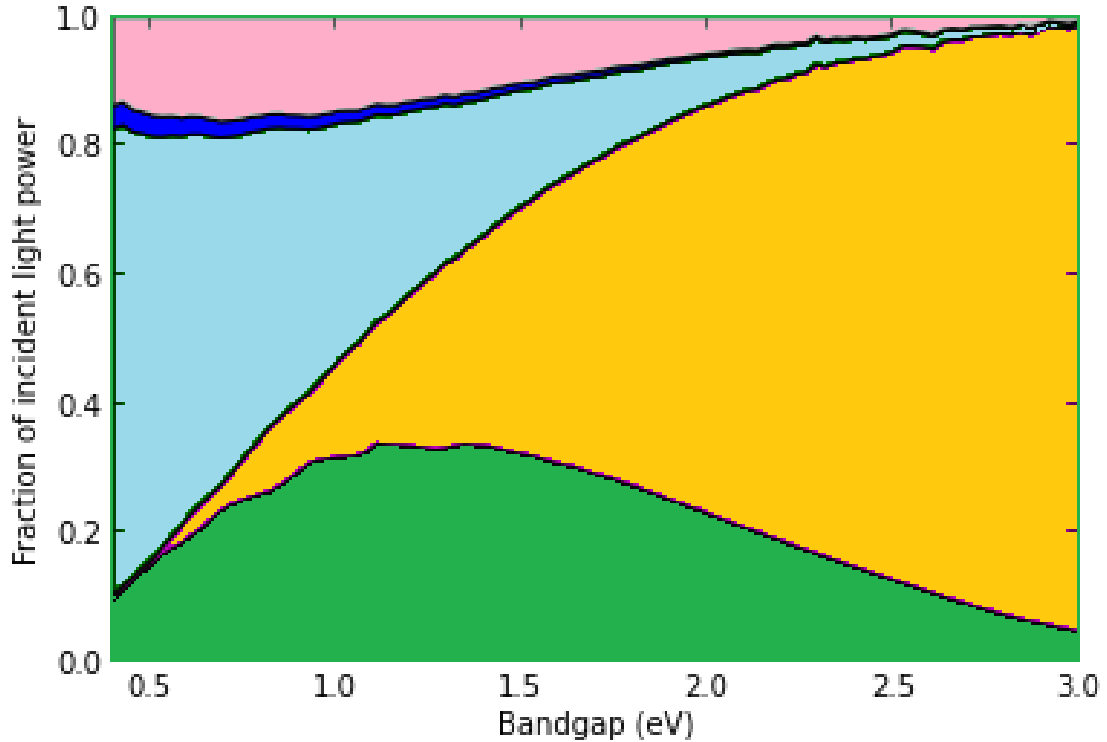
Figure 1.2: Semiconducotr solar cell efficiency as a function of bandgap by Shockley-Queisser detailed balance model. The different colors represent the energy flow as follows: green, useful electricity; yellow, below-gap photons; light blue, electron and holes thermalization to the bad edges; dark blue, current loss from radiative recombination; pink, voltage is less than bandgap.

tons are not absorbed (yellow region). The second is due to the entropy generated during the thermalization of hot carriers (light blue region). The electricity output from a solar cell can only be delivered with a voltage smaller than its bandgap. The ideal output voltage cannot exceed $V_{OC} = E_G(1 - T_{ambient}/T_{sun})$. Other limitations on output voltage come along when solar cell devices have defects.

1.3   Go beyond the Shockley-Queisser Limit

The basic assumption based on which the Shockley-Queisser limit is calculated is that the semiconductor is of a two-band system. If the wasted energies from sub-bandgap photons and the hot carrier thermalization could be saved, the 33% cap would surely be removed. The following are a few promising proposals.

Multijunction solar cell. A multijunction solar or a tandem solar cell is made by stacking one p-n junction on top of another [5]. The bandgap of each material is different and typically the sun light passes through the solar cell in the order from high bandgap to low bangap. In this case, photons with energy higher than the 1st bandgap will be absorbed while those with energy lower than the 1st bandgap will pass on and be absorbed by the 2nd material. This process goes on until the last p-n junction. An intuitive thinking will tell us that the wasted thermalization and sub-bandgap photon energy can be harvested and therefore the efficiency can be increased. But a closer look reveals that multijunction solar sells are subjected to current matching conditions across the many junctions [6]. In other words, the extracted current is determined by the smallest photo current generated within one of the few p-n junctions. So why can multijunction solar cells go beyond the Shockley-Queisser limit? The answer is the output voltage. In a single junction solar cell, the output voltage is determined by the quasi-Fermi level splitting between the n and p regions. A multijunction solar cell, however, allows multiple hikes on the splitting across the junctions and it gains a higher output voltage than a single junction solar cell. A double-junction solar cell has an limiting efficiency of 55% and a triple-junction 63%. Yet the limiting efficiency does not increase much after triple-junction and has the difficulty of stacking more than 3 junctions surges. In fact, the highest efficiency to date ($\sim 44\%$) is achieved by InGaP/GaAs/GaInNAsSb triple junction solar cell. Because a multijunction solar cell involves complicated structures (a triple-junction solar cell has more than 20-epi layers and the numbers are increasing during the efficiency race), it is difficult to drive down the cost.

Intermediate band solar cell (IBSC). The IBSC concept was proposed as an alternate approach for solar cells with efficiency exceeding the Shockley-Queisser limit [7]. In IB solar cells, one or more energy levels inside the bandgap serve as stepping stones for promoting electrons from the valence band to the conduction band with sub-bandgap, low energy photons, better utilizing the infrared portion of the solar spectrum. Photons with energies smaller than the bandgap, which will otherwise be wasted, can now contribute to the final photo-current in

the solar cell by pumping electrons from the valence band to the IB and then from the IB to the conduction band. Figure 1.3 shows a band diagram schematic of an IBSC material. The generation of photo-current can still take place even if the photons have energy less than the bandgap and as long as the radiation flux have photons with energy higher than E_L and E_H. By introducing an IB, the limiting efficiency can be pushed to about 63% if the IB is properly located within the bandgap [2]. Unlike multijunction solar cells, the gain in the efficiency mainly comes from the extra photo-current. Materials that are suitable for IBSC are generally categorized into three groups: 1. nanostructures, such as quantum dots (QDs); 2. highly mismatched alloys (HMAs), such as dilute nitrides and dilute oxides; 3. semiconductor bulk materials with a high density of deep-level impurities. In quantum dot systems, a miniband located in the middle of the bandgap of the barrier material is formed from quantum dot confined states (usually the (1,1,1) ground state). Absorption extending to the infrared region by the miniband in a solar cell structure fabricated using InAs quantum dots within GaAs has been demonstrated [8]. However, an IB cell with InAs quantum dots has limitations on the tunability of IB location, the low open circuit voltage and limited absorption. In the case of HMAs, the conduction bands undergo a anti-crossing process and are split into two subbands, i.e. E_- and E_+, due to the strong interaction between isoelectronic impurity states and the matrix conduction bands. The E_- band serves as the IB between valence band and conduction band, enabling the electron transition process shown in figure 1.3. Both dilute oxide and dilute nitrides have demonstrated such optical behavior and have been fabricated into PV devices. As to using bulk material with deep level impurities to fabricate devices, it generally require such a high density of impurities so that the material is degraded in general [8]. Although proof-of-concept devices have been demonstrated, they are of the least investigated class.
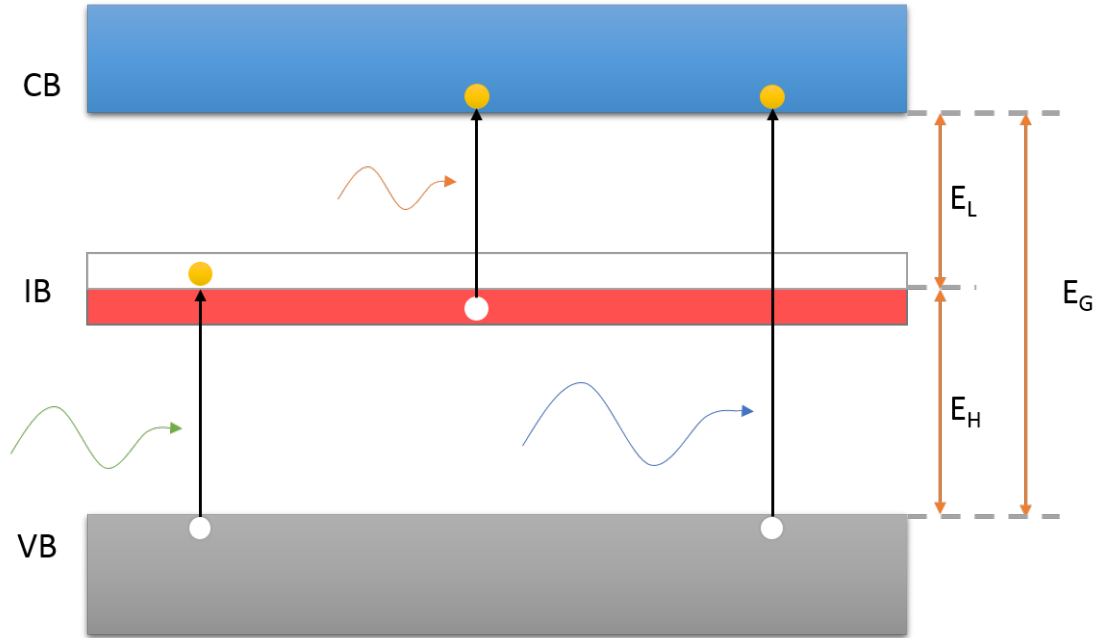
Figure 1.3: Schematics of intermediate band solar cell band diagram and the three absorption.

1.4 Dilute nitride introductions

Dilute nitrides, as a group of the HMA family has distinct properties that overlap with the IBSC demands. But to understand the technical importance of dilute nitrides, it would be helpful to step back on history and look at how it gained immense research attention outside PV but in telecommunication at the very beginning.

Silica fiber has been widely adopted as the transmitting medium for optical networks. Bandwidth and repeater-less transmission distance, limited by dispersion and attenuation, then become very important parameters in evaluation on networks. It has been found that there are three good options for the transmission wavelength inside a silica fiber: 850 nm, 1.31 μm and 1.55 μm [9]. 850 nm is a good candidate from a materials/devices perspective. zero dispersion in optical fiber is achieved at 1.31 μm and minimum attenuation at 1.55 μm. When bit rates and transmission distance are combined to evaluate these three choices, 1.31 μm and 1.55 μm clearly stand out with 1.55 μm as the best choice. However, ma-

terials that are suitable for 1.31 and 1.55 μm emissions are limited (figure 1.4). People have successfully grown InGaAsP lattice-matched to InP with 1.31 μm and 1.55 μm and fabricated them into laser devices as the light sources in optical connect [10]. Vertical-cavity surface-emitting lasers (VCSELs)[11] become an obvious choice as the requirements on power and modes increases. Yet issues arise in the InP-based InGaAsP material system when it is made into VCSELs and the major issue is the vertical cavity mirror system. AlAsSb/AlGaAsSb, InAlGaAs/InP and InGaAsP/InP have been deployed as the mirror systems and they suffer from a series of complications in terms of index contrast, growth and thermal conductivity. Compared to the mirror system above, AlGaAs/GaAs distributed Bragg reflectors (DBRs) [12] has clear advantages on various issues but it is not lattice-matched to InP. A more cost-effective way to make VCSELs is to change the laser gain media to GaAs based materials instead of bonding AlGaAs/GaAs mirror onto an epitaxial grown InGaAsP wafer.

Soon after Weyes et. al.'s discovery [13] on the large bandgap reduction by adding a dilute amount of N into GaAs, Kondow et. al. [14] added In in GaNAs to further reduce the bandgap to 1.3 μ emission and balance the tensile strain induced by N. Such GaInNAs lattice-matched to GaAs is totally compatible with the GaAs-based DBR system. GaInNAs VCSELs have been made and sold on the market. The prospect also spurred intensive research on dilute nitride materials beyond telecommunication over a wide spectrum: theories to explain the uncommon properties of its class, advanced techniques to grow dilute nitrides, bandgap and density of states engineering on dilute nitrides, next generation solar cells, integration of III-V on silicon, etc.

The peculiar bandgap reduction by N incorporation, in contradiction to an increment predicted by Vegard's law, comes from the nature of the N atom as an isovalent impurity in conventional III-V materials. When the substitutional impurity atom has the same valence as the host atom, it is referred to as an isovalent or isoelectronic impurity. The s-state of the isovalent impurity interacts with the surrounding dangling sp^3-orbitals and its energy level is pushed upward on top of the conduction band of the host. Due to the large electronegativity of N, its states
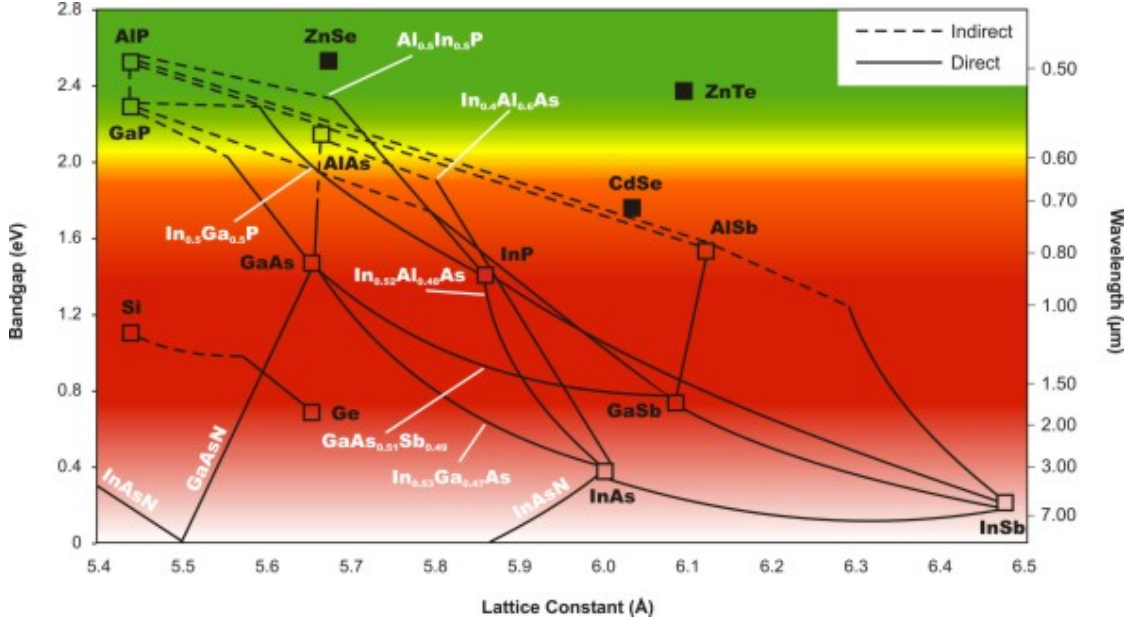
Figure 1.4: Bandgap-lattice relations for III-V semiconductors.

are highly localized in real space while extend flatly in k space (figure 1.5). In the case of GaAs (figure 1.5), the N level anti-crosses the conduction band. The N level retains s-like character and interacts strongly with the conduction band. When the amount of isovalent increases to the point of forming random alloys, these couple states begin to evolve into two new bands, E_- and E_+, with the lower one lying below the original conduction band. So far, the most efficient model to predict the locations of the two newly formed bands is the empirical band-anticrossing model [15]. The interaction is described by a perturbation Hamiltonian,

$$\begin{pmatrix} E_C(k) & C_{NM}\sqrt{x} \\ C_{NM}\sqrt{x} & E_N \end{pmatrix},$$

where E_C is the matrix conduction band, E_N is the N level, C_{NM} is the interaction coefficient of the matrix conduction band and the N energy level and x is the N content. Solving for the eigen values of the perturbation matrix above gives the E-k expression for the dilute nitride alloy,
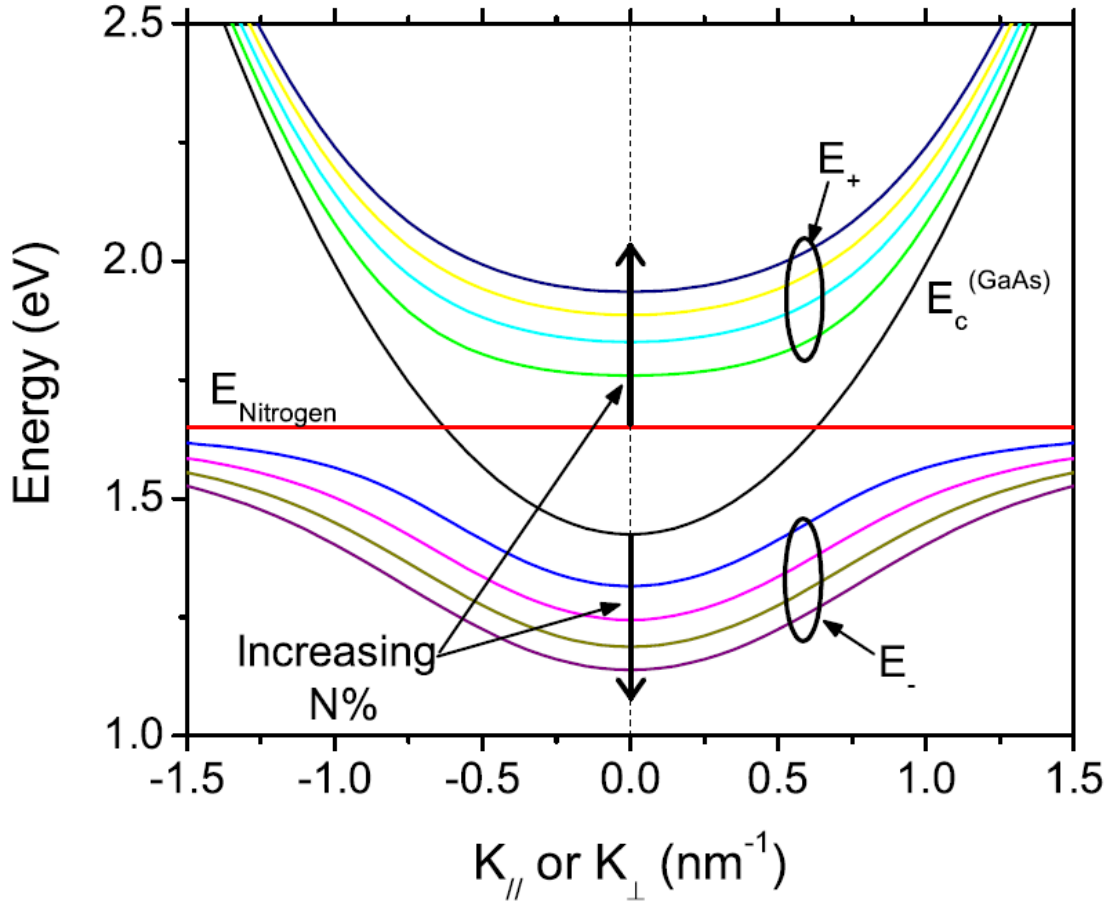
Figure 1.5: The energy-momentum diagram of GaNAs. The two bands formed after alloying are referred to as E_- and E_+.

$$E_\pm(k) = \frac{1}{2}\{[E_C(k) + E_N] \pm \sqrt{[E_C(k) - E_N]^2 + 4C_{NM}^2 \cdot x}\}. \qquad (1.2)$$

There are a few immediate observation on equation 3.1 and figure 1.5. First of all, the change in the band structure only happens in the conduction band. The E_- band lies below the original conduction band and accounts for the bandgap reduction. Secondly, the band curvature is reduced (an increase in effective mass), and both E_- and E_+ become significantly nonparabolic away from zone center. And thirdly, as N content increases, all the phenomena increase accordingly.

The effects from N leads to opportunities on device application. For example, the bandgap reduction enables 1.31 μm or 1.55 μm emission that are good

for telecommunication. The increase in effective mass leads to a higher predicted figure of merit in thermoelectrics. The slitting of the conduction band provides a platform for devices that require multiband system, e.g. IBSC.

1.5   Thesis proposal and outline

Given the promising properties of dilute nitrides, the purpose of this thesis is to investigate an IBSC material candidate, GaNAsP. This material system was firstly proposed by Yu et. al. through a N ion implantation demonstration. However, it had not been epitaxially grown with the favored constituent compositions and fabricated into IBSC device prior to the study of this thesis. Therefore, the goal of this thesis is to use an advanced thin film growth technique, i.e. molecular beam epitaxy (MBE), to grow this novel HMA and perform in-depth study of its structural, optical and electrical properties. All the studies involved serve to one underlying philosophy — to make a GaNAsP based IBSC device. The thesis is then organized in the following chapters. In chapter 2, the experimental techniques involved in this thesis study, i.e. MBE, X-ray diffraction, photoluminescence, etc., are briefly introduced. In chapter 3, the reason of using GaNAsP as IBSC and the material design and modeling on GaNAsP will be firstly discussed. And the material growth, composition monitoring and control technique, structural characterization, optical characterization, band structure and material-wise proof-of-concept on IBSC will be followed. Chapter 4 mainly focuses on IBSC device. The device design principle for IBSC will be firstly discussed and a few issues in dilute nitride, including the n-type dopiing efficiency, will be discussed. A variety of device structures will be compared and the electrical measurement on IBSC device will be described. And finally, chapter 5 promotes a few possible optimization means on the GaNAsP device.

2 Experimental Procedures

A robot must obey the orders given to it by human beings,
except where such orders would conflict with the First Law.

—Isaac Asimov

2.1 Overview

Since its invention in the late 1960s at AT & T Bell Labs by Cho and Arthur [16], Molecular Beam Epitaxy (MBE) has been widely used as an advanced technique to grow high-quality semiconductor thin films for fundamental scientific studies and various applications. A typical MBE machine consists of the following basic components: a high vacuum (HV) or ultra-high vacuum (UHV) growth chamber, effusion cells as material sources and shutters, a substrate holder/heater, vacuum gauges and elements to achieve an HV or UHV environment (cryogenic pumps, turbo pumps, ion pumps and liquid nitrogen cryo-shroud, etc).

The HV or UHV environment allows a few surface monitoring techniques to provide in-situ information and feedback during material epitaxy. A popular and widely adopted technique is Reflection High Energy Electron Diffraction (RHEED) [17] and most MBEs are equipped with a RHEED gun and a phosphorous coated viewport for surface morphology monitoring. Other in-situ monitoring techniques include X-ray diffraction/reflection, Auger probe, etc.

All samples studied in this thesis were grown with a gas-source MBE (GSMBE) and characterized with high resolution X-ray diffraction (XRD), photoluminescence (PL), photoreflectance (PR), photoabsorption (PA) and atomic force microscopy (AFM). This chapter is devoted to an introduction of the GSMBE system

and some of the characterization techniques mentioned above.

2.2   Gas-source Molecular Beam Epitaxy

The GSMBE was introduced in the 1980s by Panish in the movivation of growing high quality phosphorous containing compounds [18]. Before the phosphorous valved cracker was invented, red phosphorous was evaporated into gaseous tetramer P_4. P_4 has an extremely low sticking coefficient on InP surface, therefore, high-quality InGaAsP/InP had not been obtainable by traditional solid source MBE. GSMBE was then introduced with the advantage of providing P_2 to grow high-quality phosphides. Additional benefits of using GSMBE include the capability of abrupt change on both type and flux of group-V sources and reduction on the frequency of growth chamber opening for recharging group-V sources.

In general, group-III, group-V and dopants can all be replaced by gas sources in GSMBE. The following description only applies to the GSMBE reactor involved in this thesis project. Figure 2.1 shows a schematic of a Varian Gen-II GSMBE modified to handle group-V gaseous phase source. Solid elemental Al, Ga and In and solid Si and Be are used as group-III and dopant sources. Their fluxes are generated by Knudsen effusion cells and controlled by their temperature. AsH_3 and PH_3 are introduced into the growth chamber through hydride injectors and thermally cracked at 1000°C by cracker cells into As_2 and P_2, along with H_2, before reaching the substrate. The As_2 and P_2 dimer fluxes are controlled by the AsH_3 and PH_3 flow rate through mass flow controllers (MFCs). The full scale of the mass flow controllers are 5 sccm and 20 sccm for As_2 and P_2, respectively. Typical settings for growth of arsenides and phosphides are in the 0.5-2 sccm and 4-6 sccm range, respectively. Because of the gas sources, the growth pressure during MBE is $\sim 10^{-5}$ Torr and is generally higher than solid source MBE. In front of all cells are installed pneumatic shutters, whose operation sequences are controlled by a home-made programmable shutter control circuit box that allows precise growth recipe. Manual control is also possible.

The growth chamber vacuum is maintained by a Ebara cryo-pump with

a pumping speed of 2200 l/s and a Pfeiffer Model TMU1600 turbo molecular pump with a pumping speed of 1500 l/s. A liquid nitrogen source shroud and a central shroud are also equipped to condense background residual gases to reduce contaminants during epitaxy. The background pressure is normally in the mid-10^{-9} Torr with cryo-shroud filled with liquid nitrogen and furnaces heated to running temperature.

Also installed is an RF plasma source (Oxford Applied Research Model MPD21). Some of its features include: electrode-free to avoid contamination; UHV-compatible for operation at pressure $< 10^{-5}$ Torr and a wide range of beam flux of 0-5 sccm. Ultra-high purity (4N) N_2 gas first goes through a regulator, in which the pressure is modulated at a pressure of 50 psi, and a purifier (Matheson Gases & Equipment, 6190-V4MM Membrane Type) to remove water vapor and oxygen. Then nitrogen gas goes through an MFC and finally arrives at the RF plasma source. There nitrogen radicals are generated and injected by pressure gradient into the growth chamber through a beam exit aperture with 16 holes, each of which has a diameter of 0.3 mm. Such a configuration is to maintain the pressure difference across the aperture interface. In front of the aperture is a shutter to cut off N source when no N is needed during growth. An manual inlet valve is also installed on the N_2 gas tubing right in front of the RF cell to isolate N_2 source and the growth chamber in idle state.

During growth, the N plasma is discharged by inductively-coupled RF electromagnetic (EM) field (13.56 MHz) inside a pyrolytic boron nitride (PBN) tube. The RF EM excitation produces three species: 1. N radicals that can actually incorporate into films; 2. N_2 ions that do not contribute to N incorporation but damage sample surface by ion bombardment and 3. N_2 molecules whose bonds are not fully broken by the RF EM field and do not incorporate into films either. To prevent ion bombardment from the ionized N_2 molecules, a set of parallel deflectors biased by a certain voltage is installed right in front of the aperture. The electric field across the two deflector plates will accelerate ionized N_2 molecules and distort their beam path. The ions hence miss the substrate target and do not cause surface damage. Such a deflector configuration is not equipped in the
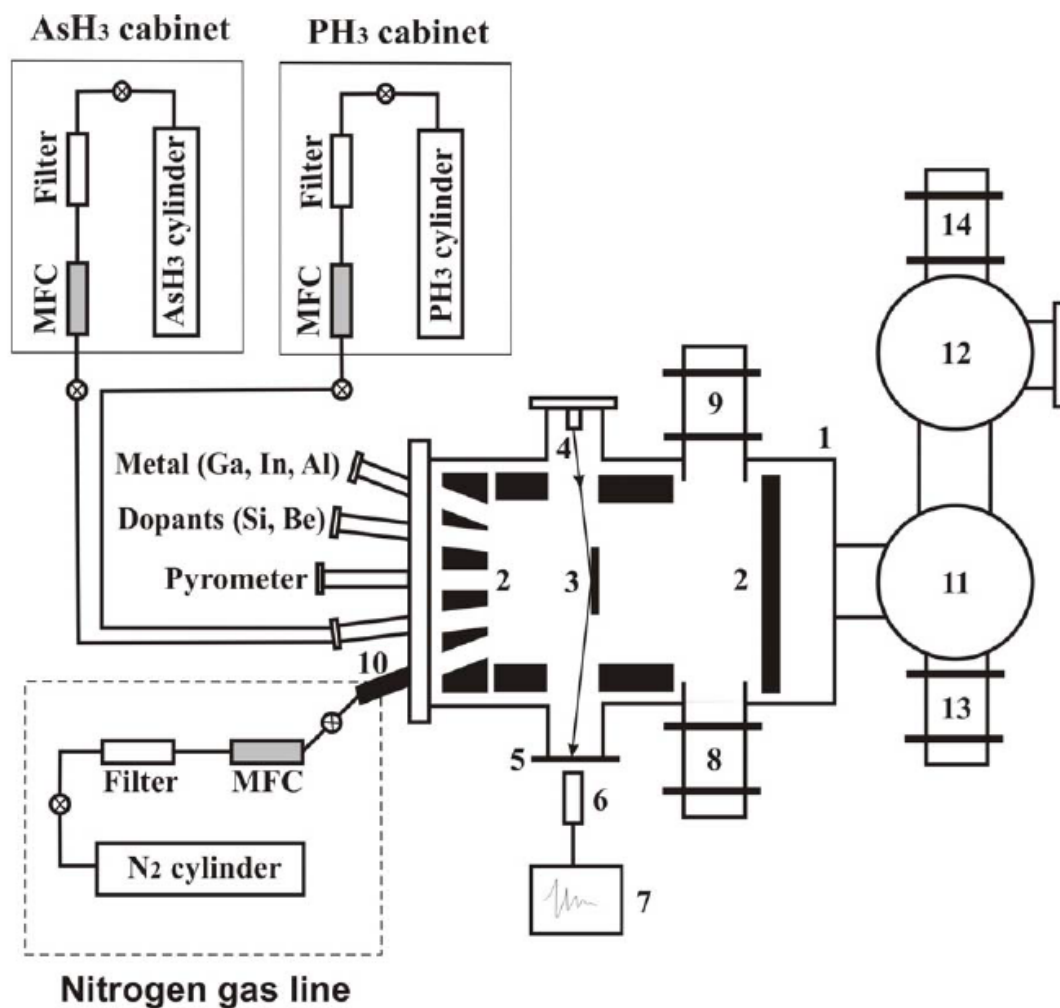
15

Figure 2.1: Schematics of the modified Varian Gen-II Gas-source Molecular Beam Epitaxy system.

MPD21 model.

A certain flow rate of N_2 gas needs a corresponding RF power to discharge. A typical relation between these two parameters is quantified by measuring the plasma discharge emission intensity as a function of RF power supplied and N_2 flow rate. Such a relation has been determined experimentally in our Gen-II chamber, shown in figure 2.2. On the lower right hand side are regions where N_2 flow rate is so high that RF power module can merely sustain (low intensity mode) or cannot trigger the discharge (no discharge region). While on the upper left corner lies the high intensity region where higher RF power is supplied to discharge a relatively small flow of N_2 gas. Between the two extreme regions is the usual operation region, where one can find many sets of (RF, flow rate) values that can produce the same plasma intensity. Since the active N radical species are proportional to the plasma intensity, in other words, various settings can produce films with the same N composition (given other growth conditions are the same). The general guideline for choosing a RF power and a N_2 flow rate is to sustain a stable plasma discharge while minimize chamber pressure and ion bombardment to ensure high-quality films. It narrows down to the violet color area marked in figure 2.2. Fine tuning of the plasma condition inside the region is based on film crystal quality and optical properties.

2.3   Reflection High Energy Electron Diffraction

A RHEED gun is used for in-situ monitor of sample surface condition during growth. The high energy electrons hit a sample at a grazing angle and the reflected beam of electrons construct a reciprocal space map of the sample on the phosphorous screen. More discussion about the reciprocal space map can be found in the next section.

When a film is undergoing a layer by layer growth, RHEED patterns are streaky and a RHEED intensity oscillation is usually seen. Such a RHEED intensity oscillation can be induced by group-III flux on a group-V terminated surface and vice versa. The traditional RHEED intensity oscillation is generally referred
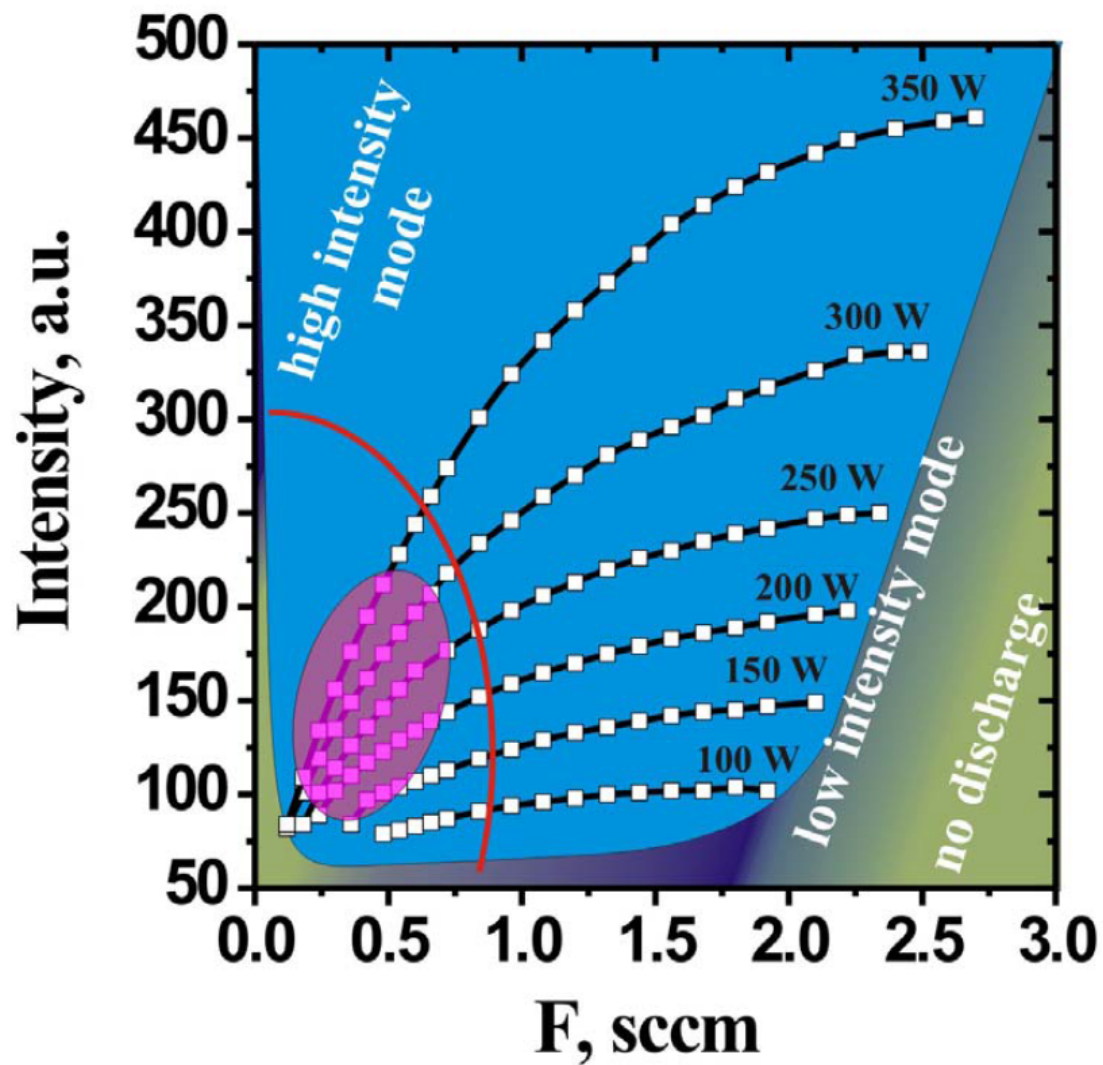
Figure 2.2: The optical intensity - nitrogen flux diagram for the nitrogen plasma (adapted from V. Odnoblyudov's PhD thesis, UCSD, 2006).
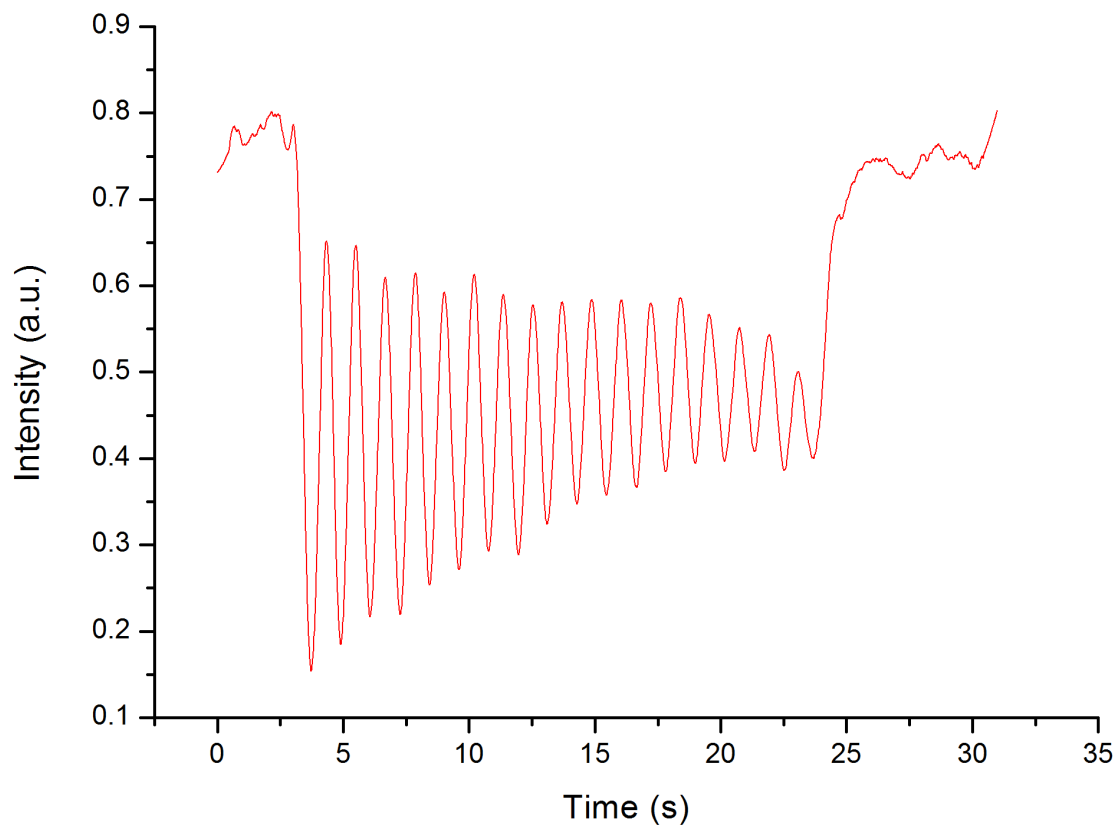
Figure 2.3: A RHEED intensity oscillation is triggered by opening the Ga shutter after a growth interruption. The intensity recovers fully after the Ga shutter is closed again.

to the first case, see figure 2.3. After a growth interruption, the group-III shutter is re-opened and a group-III induced RHEED intensity oscillation allows one to calculate the growth rate, R_{III}, by measuring the oscillation period, since III-V semiconductor growth is group-III rate limited in general. Group-V induced RHEED intensity oscillation is not common but it is easily seen in GSMBE with a swift group-V gas capability. It requires a deposition of a few monolayers of group-III atoms on a sample surface with the group-V shutter closed, and a RHEED intensity oscillation is triggered when the group-V shutter is opened. The group-V growth rate, R_V, can be calculated in the same manner for group-III. An accurate V/III incorporation ratio then follows $\dfrac{R_V}{R_{III}}$.

Other information, including surface reconstruction, strain, lattice constant and crystal orientation, etc., can all be observed in-situ by RHEED patterns.

2.4   X-ray diffraction and reciprocal space mapping

X-ray is a widely used tool as a non-destructive way to extract crystal structural information. When used in a diffraction geometry, a diffraction happens as the incoming and outgoing wavevectors, k_i and k_o, satisfy k_o-k_i=$\mathbf{G}$, where $\mathbf{G}$ is a reciprocal space lattice vector. The reciprocal space is a Fourier transform of the real lattice space as defined in the following manner:

$$\mathbf{R} = n_1\mathbf{a}_1 + n_2\mathbf{a}_2 + n_3\mathbf{a}_3, \tag{2.1}$$

$$\mathbf{G} = h\mathbf{b}_1 + k\mathbf{b}_2 + l\mathbf{b}_3, \tag{2.2}$$

And vectors $\mathbf{R}$ and $\mathbf{G}$ then follow:

$$\mathbf{a}_i \cdot \mathbf{b}_j = 2\pi\delta_{ij}, \tag{2.3}$$

$$exp(i\mathbf{G} \cdot \mathbf{R}) = 1. \tag{2.4}$$

For cubic phase III-V semiconductor, the most common XRD scans are rocking curve scan (ω scan) and $\omega/2\theta$ scan in a symmetric scan geometry. ω scan is usually used to evaluate crystallinity while $\omega/2\theta$ scan is used to calculate the d-spacing by the Bragg diffraction equation,

$$2d\sin(\theta) = n\lambda, \tag{2.5}$$

where λ is the wavelength of Cu K_α (1.5406 $\mathring{A}$ within the scope of discussion of this thesis). A $\omega/2\theta$ scan is most commonly done on (004) planes for Zinc Blende structure and the lattice constant can be determined if the material is strain-free. When strain is involved, the out of plane lattice constant cannot be determined solely from symmetric $\omega/2\theta$ scans.

A 2D scan, reciprocal space map (RSM), is a more general scan and can bring more information, including strain/relaxation and lattice tilt, and it is of great interest particularly for metamorphic growth. Figure 2.4 shows a pseudomorphic layer, a completely relaxed layer and their corresponding RSMs. In the case of pseudomorphic strained layer, epilayer shares the same in plane lattice constant and takes a different out of plane lattice constant. Therefore, the q_y values are the same and the q_z values are different for every plane. In the completely relaxed case, epilayer layer and substrate diffraction nodes form a strait line with the origin. The quantitative description can be referred to the following q_y and q_z definition. When a layer is partially relaxed, the lattice takes a form between the two end points described above. Figure 2.5 shows an RSM of (004) and (224) planes of a layer not lattice matched to the substrate [19]. The asymmetric (224) RSMs can reveal relaxation information while the (004) RSMs are sensitive to crystal plane tilt information.

$$\Delta q_y = \frac{2}{\lambda}\sin(\theta + \Delta\theta) \times sin(\Delta\omega - \Delta\theta), \tag{2.6}$$

$$\Delta q_z = \frac{2}{\lambda}[\sin(\theta + \Delta\theta) \times cos(\Delta\omega - \Delta\theta) - sin(\theta)]. \tag{2.7}$$
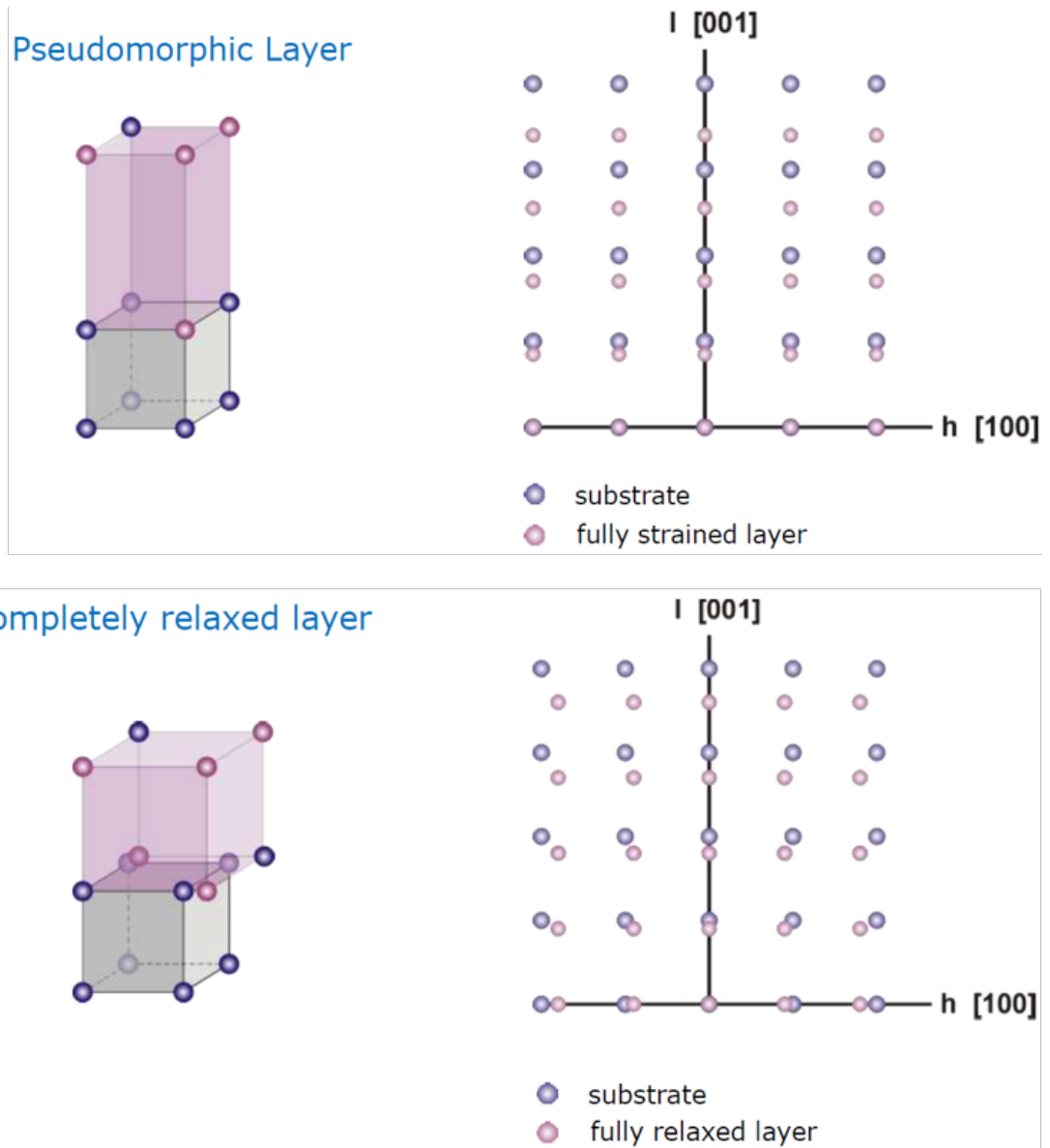
Figure 2.4: Reciprocal space schematics of pseudomorphic strained layer and fully relaxed layer.
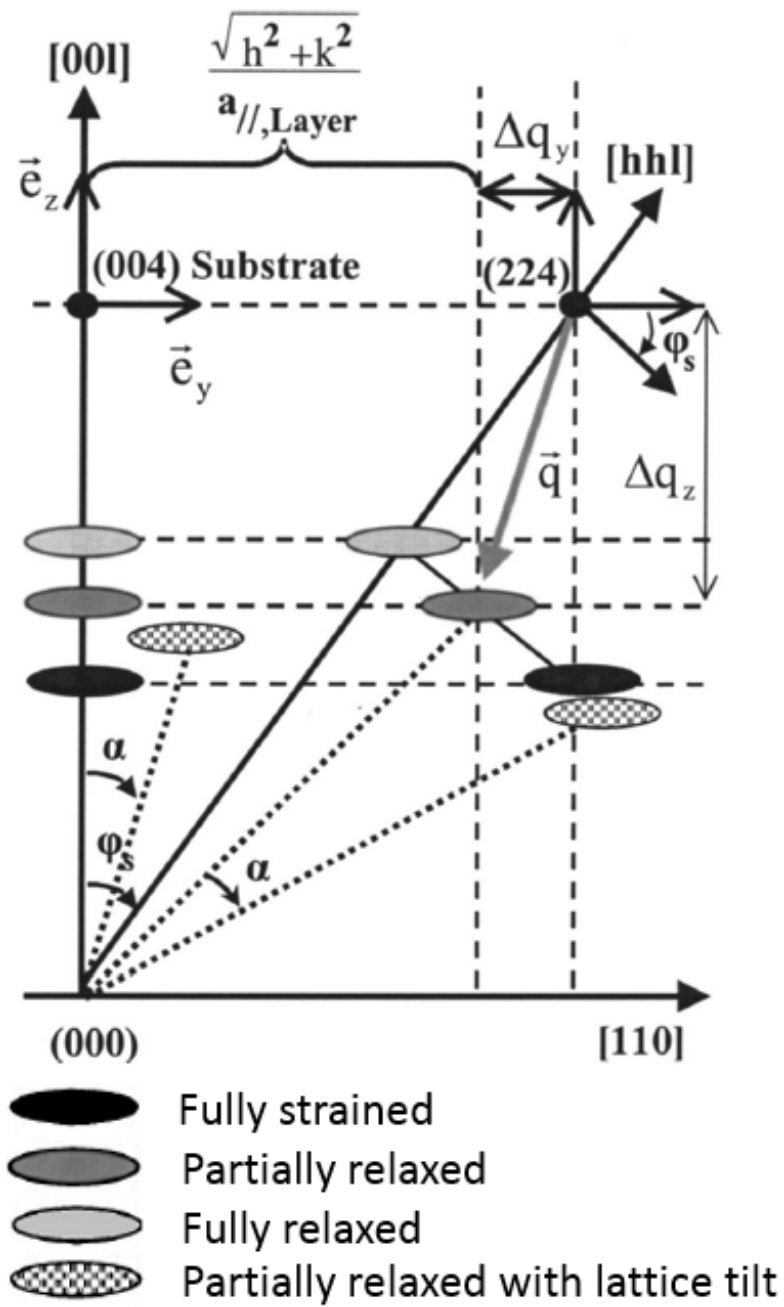
Figure 2.5: Diffraction nodes schematics of (004) and (224) planes. The four cases, fully strained, fully relaxed, partially relaxed and tilted layers are shown. [19]
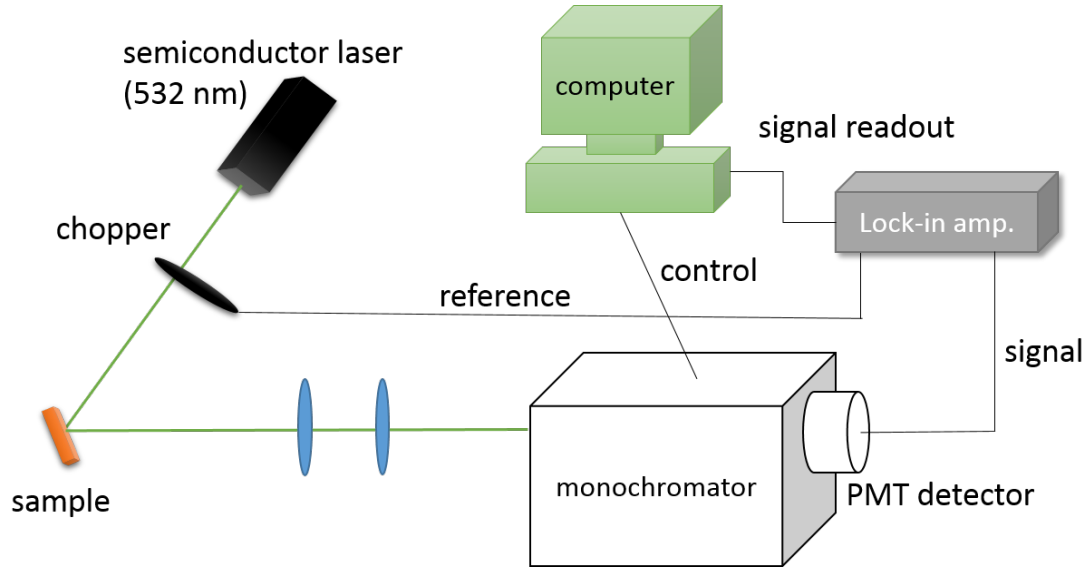
Figure 2.6: Schematics of the PL setup used in this study.

2.5 Photoluminescence

When photons pass through semiconductor materials, they create electron-hole pairs if they bear energy higher than the semiconductor bandgap. Such photo-generated electron-hole pairs partially recombine radiatively. Such a process is called photoluminescence (PL) [20]. Because PL is a sensitive and non-destructive way to detect semiconductor material quality, it is the main optical characterization technique employed in this study. A 532 nm semiconductor laser is used as the optical pump in the PL set-up. The laser goes through a chopper that sets the reference frequency for the lock-in amplifier, and then hit on a sample. The emission signal is dispersed inside a SPEX 1870 monochrameter and collected by a Hamamatsu R636-10 photomultiplier tube (PMT) through a lock-in technique. The signal intake and wavelength control are both computerized by a Matlab program. For temperature dependent PL study, a sample is mounted on a cold finger and enclosed in a cryo-stat.
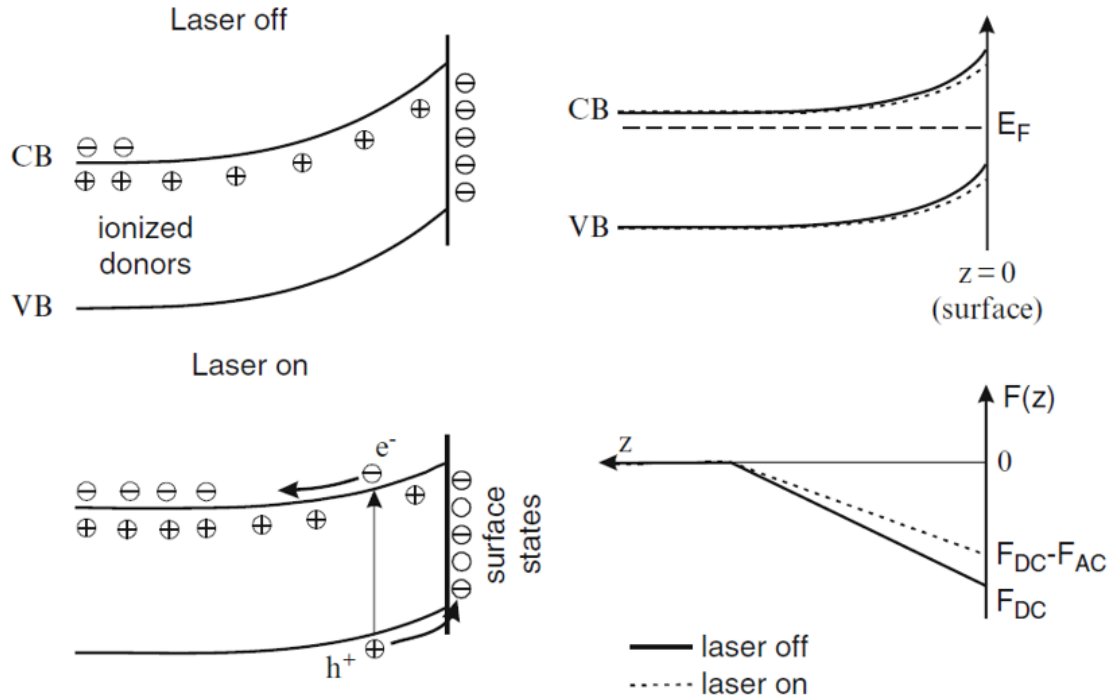
Figure 2.7: Band bending modulation of photoreflectance on a n-type semiconductor.

2.6 Photoreflectance

Photoreflectance (PR) is a kind of electro-modulated spectroscopy [21]. A laser is used as an electron-hole pair generation pump to modulate the internal electric filed near a sample surface (due to Fermi level pinning) during a reflectance spectrum measurement (figure 2.7). The derivative-like character of modulated PR ($\Delta R/R$) filters out the background signal and enhances the optical transition signal which is otherwise too weak to see in reflectance alone (R). Two reflectance signals are taken when the modulation laser is on and off, $I_0 R^{on}, I_0 R^{off}$, where I_0 is the spectral characteristic of the experimental setup. And the changes in reflectance from the modulation is $\Delta R = R^{off} - R^{on}$. The signal purely from a sample can be obtained when ΔR is divided by R,

$$\frac{\Delta R}{R} = \frac{I_0 \Delta R}{0.5(I_0 R^{off} + I_0 R^{on})}. \tag{2.8}$$

The energies of optical transition can then be extracted by fitting the PR spectra with Aspnes formula,

$$\frac{\Delta R}{R}(E) = Re[Ce^{i\vartheta}(E - E_j + i\Gamma)^{-m}], \tag{2.9}$$

where C and ϑ are the amplitude and phase of the resonance, and E_j and Γ are the energy and the broadening parameter of the optical transition, respectively. Depending on the transition type, m takes 2, 2.5, 3 for an excitonic transition, a 3-D critical point one-electron transition and a 2-D critical point one-electron transition, respectively.

3 Growth and characterization of GaNAsP

If at first the idea is not absurd, then there is no hope for it.

—Albert Einstein

3.1 Overview

This chapter is devoted to the study of intermediate band solar cell (IBSC) material GaNAsP. First, the special band structure of GaNAsP is described based on the band anti-crossing (BAC) model and its suitability as an IBSC material is discussed and compared to GaNAs. The bandgap engineering of GaNAsP to optimize intermediate band solar cell conversion efficiency is then followed based on a 3-band material model. The challenge in GaNAsP material synthesis is later elaborated. And then the structural design for metamorphic growth and the description of growth procedure by GSMBE, alloy composition and optical property characterization are finally detailed in the following sections.

3.2 Bandgap design

Given the suitability of band structure of dilute nitride GaNAs in chapter 1 [22], it is not the ideal material system for IBSC. The reasons are as follows:
1. The N energy level lies above the conduction band minimum of GaAs, which makes E_- band relatively broader compared to the case when N energy level is below the matrix conduction band minimum. A broad band is not favored as an IB
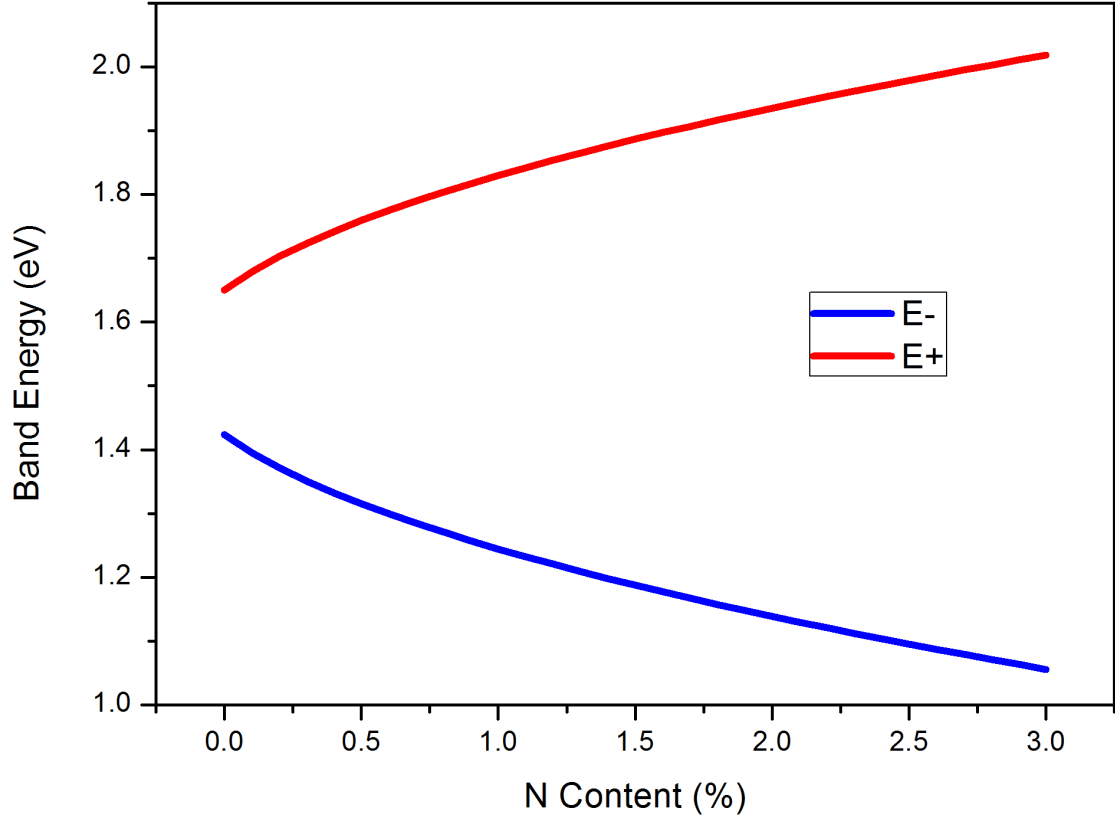
Figure 3.1: E$_-$ and E$_+$ as N composition changes in GaNAs.

because it allows "hot electron" thermalization within the IB. Such wasted thermal energies cannot contribute to final power conversion without using thermal cells. 2. GaAs has a bandgap of 1.42eV and in alloying with N will form E$_-$ and E$_+$ bands. Figure 3.1 shows the E$_-$ band and E$_+$ band for the N composition range from 0% to 3%. E$_-$ band goes from the GaAs bandgap 1.42 eV at N of 0% to 1.06 eV at N of 3%. While E$_+$ band goes from 1.65 eV at N of 0% to 2.02 eV at N of 3% (Note that at N of 0% E$_+$ does not exist yet. E$_+$ shown here is for energy range demonstration purpose only). The margin within which the E$_-$ and E$_+$ bands can vary is still far away from the optimal configuration by Luque et. al.'s calculation on 3-band-system [7].

These two characteristics of the band structure of GaNAs significantly limit the final power conversion efficiency. A possible solution is to add one more con-stituent to form quaternary alloy and further tailor the band structure. Indeed,

adding P into GaNAs will solve the two problems listed above and GaNAsP has the following advantages over GaNAs.

1. The N energy level with respect to the conduction band edge of the matrix is a function of the As composition and it lies below the matrix conduction band within a specific range of As composition, specifically [As] < 0.68 (see figure 3.2). When the N level lies below the conduction band edge, the E$_-$ band after alloying inherits more characteristics from the N energy level. In other words, E$_-$ band becomes more localized and is narrower compared to E$_+$. A narrow band is more beneficial as an IB because it provides a well defined energy level as a stepping stone for the sub-bandgap energy photons while limits the energy wasted within the band during "hot electrons" thermalization. Generally speaking, the narrower the IB is, the better it is for power conversion [2]. However, there are other restrictions on IB design (half-filled) and they will be discussed in the next chapter when an IBSC device structure fully comes into the picture.

2. Thanks to the extra degree of freedom from the P composition, the energy level of E$_-$ and E$_+$ can be tuned into a much wider range and can fall into the optimal configuration for a 3-band solar cell system. With the BAC model [15], the E$_-$ and E$_+$ bands can also be calculated with the following equation,

$$E_\pm(k) = \frac{1}{2}\{[E_C(k) + E_N] \pm \sqrt{[E_C(k) - E_N]^2 + 4C_{NM}^2 \cdot x}\}. \qquad (3.1)$$

The E_C is the matrix lowest conduction band. And E_N is the N level in the GaAsP alloy, which is a function of As composition as shown previously. C_{NM} is the interaction coefficient of the matrix conduction band and the N energy level. And x is the N content.

For the whole As composition range in GaAsP, the band nature does not stay the same. As shown in figure 3.2, GaAsP is an indirect bandgap material with X band as the lowest conduction band for [As] < 52%. The Γ and X band crossover occurs when [As] goes beyond 52% [24]. When the BAC model was first introduced [15], it was intended to model the interaction between the conduction band states (Γ band) and the N states in GaAs. Yet later it was shown that similar approach could be applied to describe the BAC interaction with the minima at X
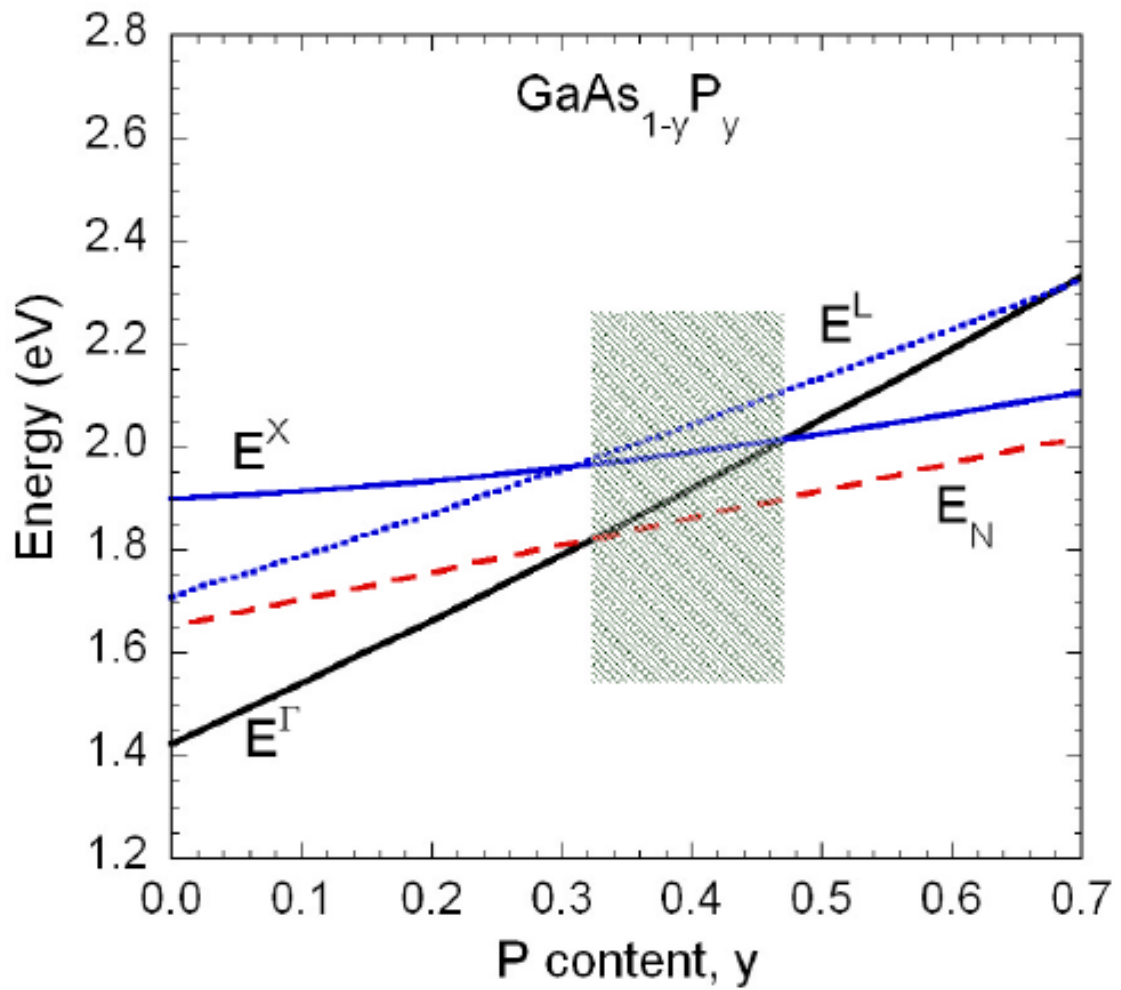
Figure 3.2: The N energy level position relative to the Γ band and the X band and the L band with different As composition in the GaAsP alloy. [23]

and L points of the Brillouin zone. The only difference is that the interaction coefficient, C_{NM}, has to be modified since the conduction band states lose the s-like character with the A_1 symmetry. It was observed that the interaction between N-related states and conduction band states at the boundary of Brillouin zone still exists for dilute nitrides. Some experimental evidence of this interaction has been provided by Seong et. al. using Raman scattering and Perkins et. al. using electroreflectance technique [25, 26]. Thus, a non-zero element is expected for electron states at the boundary of Brillouin zone. It has been found [27] that the coefficient can be expressed as

$$C_{NM}(k) = \frac{C_{N\Gamma}}{[1 + (ak)^2]^2},\tag{3.2}$$

where a is the parameter of the order of lattice constant describing the spatial extent of the N localization wave function and $C_{N\Gamma}$ is the C_{NM} for k=0, which should be determined from measurements of the BAC interaction in the conduction band at the Γ point. Yet experimental findings conclude that $C_{NM}(k)$ at the X point is 3-4 times smaller than $C_{N\Gamma}$ and the splitting is at least one order of magnitude smaller [27]. Therefore, the slitting on X band can be safely ignored.

Material parameters used for the following calculations were taken from Ref. [24] and BAC parameters (E_N and C_{NM}) for $GaN_xP_yAs_{1-x-y}$ have been calculated as linear interpolation of the BAC parameters for GaNAs (E_N =1.65 eV and C_{NM}=2.8 eV [28, 29]) and GaNP (E_N =2.18 eV and C_{NM}=3.05 eV [29]).

Figure 3.3 shows the calculated dispersion relations for the conduction and the valence bands close to the Γ point of the Brillouin zone. The band structure of the $GaAs_{0.6}P_{0.4}$ was obtained within the 8-band k·p Hamiltonian. The dispersion relations of $GaN_{0.02}As_{0.58}P_{0.4}$ were calculated using the BAC model. It is seen in figure 3.3 that the BAC produced splitting of the conduction band results in formation of a narrow IB (E_-) well separated from the upper conduction band (E_+). This is a band structure configuration envisioned for the intermediate band solar cell concept described previously.

Based on the BAC model, one is able to calculate the energy levels of IB (E_-) and the conduction band (E_+) for various [N] and [As] in the GaNAsP
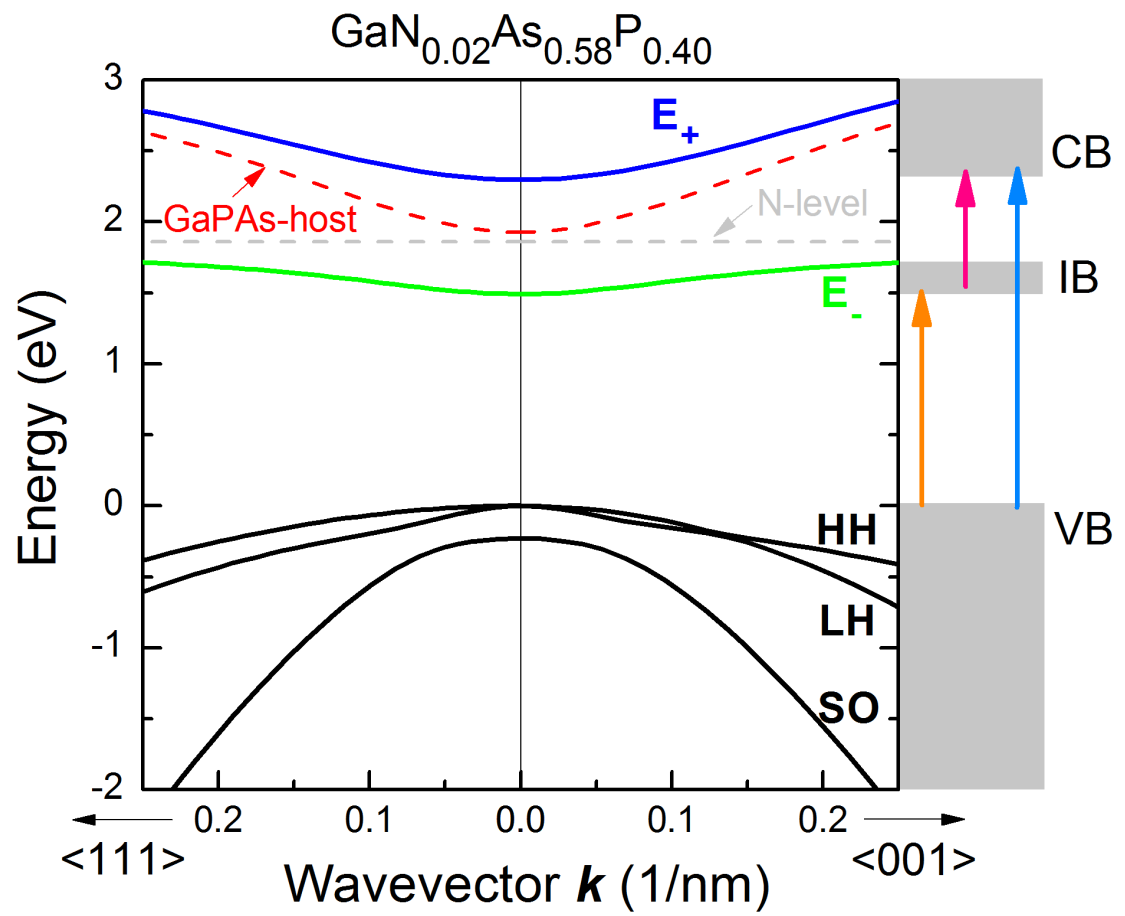
Figure 3.3: Band structure of $GaAs_{0.6}P_{0.4}$ host (red dash lines) obtained within the 8-band k·p model and $GaN_{0.02}As_{0.58}P_{0.4}$ (black lines) calculated within the BAC model.

material system after the dilute nitride alloy formation. Figure 3.4 shows such a calculation on an energy contour map. The x-axis is the N composition while the y-axis is the As composition. The solid lines and the dash lines are transition energies from the valance band to IB and from IB to conduction band respectively, which are schematically shown on the right hand side of the figure. According to our previous discussion, GaAsP with As composition larger than 52% has a direct bandgap and GaAsP with As composition less than 68% has a narrow IB. Such a range on As composition is marked out by an orange color zone in figure 3.4. Previous findings suggest that N incorporation larger than 0.5% changes the band nature from indirect to quasi-direct in GaP. Therefore, the lower bound restriction on As composition is actually not very stringent. According to Luque's and Shaw's calculation on power conversion efficiency of a 3-band system, the two lowest energy threshold combination with theoretical efficiency more than 60% is mapped with a blue shade in figure 3.4. There is an overlap area of the blue zone and orange one, which satisfies both high predicting efficiency and narrow IB conditions. The overlap zone is of highest interest when tuning the N and As composition during growth. However, as described in chapter 1, GaNAsP is a highly mismatch alloy and introducing N tend to degrade material quality and increase electron scattering (lower carrier diffusion length). Hence the upper left corner in the overlap zone with fewer N content is more desired.

3.3 Growth and characterization of GaNAsP

Given the desired N and As composition in GaNAsP, the lattice constant is $\sim$ 5.54-5.56$\mathring{A}$ and there is no commercial substrate available for such a range. GaNAsP with a lattice constant of 5.56$\mathring{A}$ is lattice mismatched to GaAs ad GaP by $\sim$ 1.1% and $\sim$ 2.0%, respectively. From Matthews and Blakeslee's model [30], the critical thickness, below which the strained filmed can endure without generating misfit dislocation, can be calculated by the following transcendental equation,

$$h_C = \frac{b}{2\pi f} \frac{(1 - \nu cos^2\alpha)}{(1 + \nu)cos\lambda}(ln\frac{h_C}{b} + 1), \tag{3.3}$$
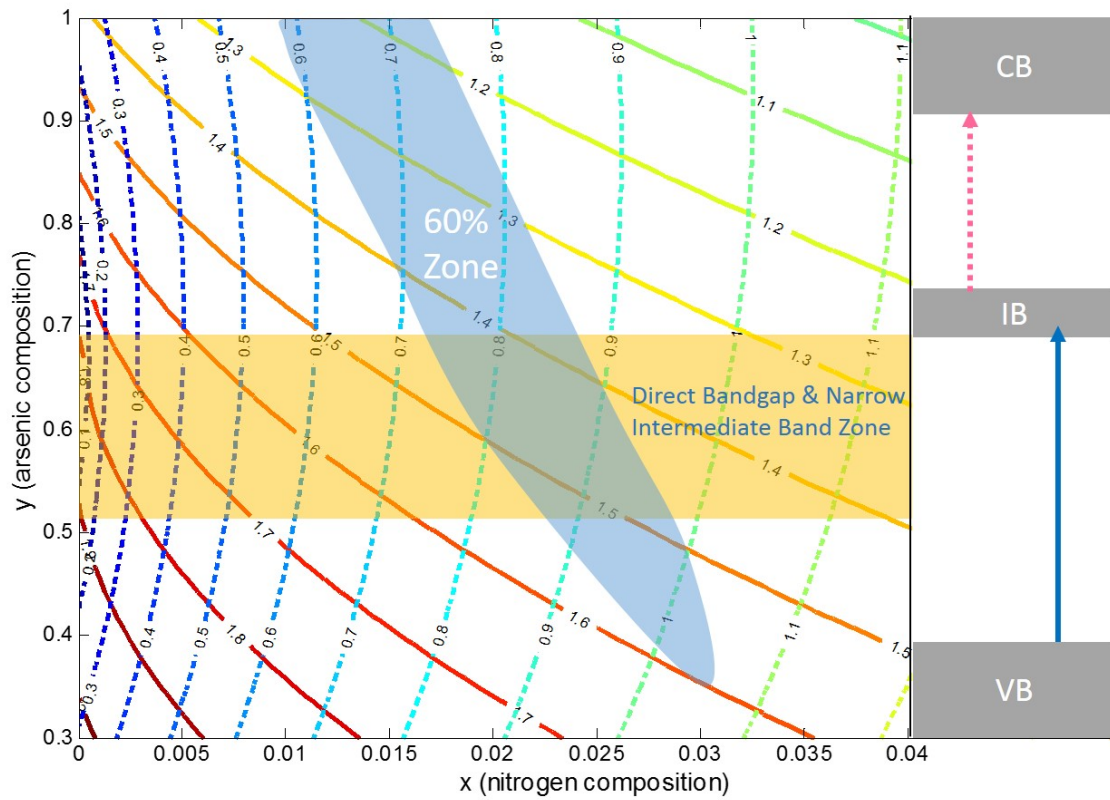
Figure 3.4: Energy contour of the two lowest energy transitions indicated on the right hand side of this figure. The blue zone is the 60% efficiency zone.

where h_C is the critical thickness, b is the Burger's vector, ν is the Poisson ratio, α is the dislocation line and its Burger's vector, λ is the angle between the slip direction and that direction in the film plane which is perpendicular to the line of intersection of the slip plane and the interface. The critical thickness of GaNAsP will be smaller than 50 nm, be it grown on either GaAs or GaP. Such a small thickness cannot qualify the absorber requirement of solar cells. Therefore, to achieve the N and As composition desired, a graded metamorphic buffer layer needs to be introduced between the substrate and the GaNAsP layer.

Both InGaP and GaAsP can be graded to 5.56 Å. Grading GaAsP has clear advantages over grading InGaP. Firstly, growth of GaInP by epitaxy can be complicated by the tendency of GaInP to grow as an ordered material, rather than a truly random alloy. Secondly, thermal dynamic calculation predicts that there is a miscibility gap between GaP and InP. Although ordering was found in $GaAs_xP_{1-x}$ for $0.15 \leq x \leq 0.6$, GaP and GaAs have a miscibility gap only below $4°C$, for which they are thought to be completely miscible. In addition, it is more straightforward to grow GaNAsP on GaAsP than switching sources from InGaP to GaNAsP. Moreover, it its practically easier to lattice match GaNAsP onto the beneath GaAsP than onto InGaP. Therefore, growing GaNAsP on a GaAsP metamorphic buffer is preferred.

There are two options for growing a metamorphic GaAsP virtual substrate: on GaAs or on GaP. From the misfit point of view, grading to x $\sim$ 0.55 in $GaAs_xP_{1-x}$ from GaAs has less misfit to accommodate than on GaP. However, the strain endured by GaAsP is tensile on GaAs while compressive on GaP. Grading from GaAs generates cracks and micro twins in the metamorphic buffer [31] and results in inferior optical and electrical performance compared to grading from GaP. Such a microscopic defects are not observed in compressively strained GaAsP in our study [32, 33]. Therefore, growing GaAsP metamorphic buffer to lay the foundation for the GaNAsP growth atop is preferred.

The novel GaNAsP alloy is not a conventional semiconductor material because it has three group-V constituents. The As and N compositions cannot be determined in the traditional way by solely doing XRD on either bulk or superlat-

tice samples followed by computer simulation based on X-ray scattering dynamical theory. We have developed a method consisting of in situ RHEED intensity oscillation monitoring and ex situ XRD characterization to determine both As and N content in GaNAsP. Detailed explanation is described as follow.

All samples discussed in this section were grown in a Varian Gen-II MBE system modified to handle gas sources. Thermally cracked PH3 and AsH3 at 1000 $^\circ C$ and RF N plasma excited at 13.56 MHz were used for P, As and N sources, respectively. Solid elemental Ga was used to generate Ga atomic beam through an effusion cell. After GaP substrate surface oxide desorption, a 0.3 μm-think GaP buffer layer was grown at 580 $^\circ C$. And a 1.5 m-think linearly graded GaAs$_x$P$_{1-x}$ and 0.5 μm-thick GaAsP with uniform As content were grown at 520 $^\circ C$. Then the top 0.5 μm-thick GaN$_x$As$_y$P$_{1-x-y}$ layer was grown to be latticed matched to this GaAsP layer. A substrate temperature of 520 $^\circ C$ was selected because 1) As incorporation is not strongly dependent on substrate temperature in such a temperature range [34] and 2) this is about the highest growth temperature for good dilute nitride optical quality before phase separation is seen [35]. However, later studies suggests that such a growth temperature is not yet optimized for n-type doping by Si, which will be further discussed in the next chapter. For in situ monitoring of the As and P compositions, an optical fiber coupled to a photodiode with preamplifier was used to extract RHEED intensity oscillation, which was further acquired through a National Instrument^{TM} USB-6008 DAQ system.

A typical Ga and P induced RHEED intensity oscillation is shown in figure 3.5. After a growth interruption, Ga induced RHEED intensity oscillation was triggered when the Ga shutter was open, from which the Ga incorporation rate, R$_R$, was obtained. Then several monolayers of Ga were deposited on the substrate surface, on which Ga formed droplets on group-V rich surface reconstruction [36]. The group-V induced RHEED intensity oscillation is a result of the dynamic equilibrium of the diffusion between droplets and group-III rich area when group-V flux impinges. When the P shutter was opened, the P-induced RHEED oscillations indicate the P incorporation rate. In figure 3.5, one can see two parts of oscillation after the P shutter was closed. The oscillation with a lower

frequency during the P shutter being closed was due to the P shutter being not leak-tight. From the oscillation with higher frequency on the right hand side, one can obtain the P incorporation rate, R_P. The same procedure was repeated with both As and P shutters open (figure 3.6). And from the oscillation with higher frequency, the As and P combined incorporation rate was obtained, R_{As+P}. The reason that As incorporation rate cannot be independently obtained is due to the surface roughening quickly because of the large 3.7% lattice mismatch between GaAs and GaP. According to the growth kinetic model our group developed [34] that As has a sticking coefficient about 40 times higher than that of P, the As content is expressed as follow when the As flux is kept smaller than the Ga flux,

$$[As] = \frac{R_{As+P} - R_P}{R_{Ga}} = \frac{R_{As}}{R_{Ga}}. \tag{3.4}$$

Three samples with different As composition were grown to verify the legitimacy of the relation above (figure 3.7). The fitting was done with a restriction of zero interception. The slope of the fitting is almost unity (1.043). It shows that our in situ method of determining As composition is valid within reasonable error allowance. However, since As and P are under nonlinear growth kinetics in GaAsP, to make this in situ composition determination accurate in GaAsP on GaP substrate it is required that 1) substrate temperature is high enough to see group-V induced RHEED oscillation but low enough to be in the temperature-independent region for As incorporation; 2) As flux is smaller than Ga flux, or strictly speaking, the As incorporation rate is smaller than that of Ga; 3) P flux should not be too high, easing the incorporation competition between the two group-V species. During the growth of the dilute nitride layer, it is assumed that the As incorporation is unaffected by the N incorporation in the top GaNAsP layer based on the fact that the P vapor pressure is much higher than that of As[37, 38].

An XRD $\omega/2\theta$ line scan on the (004) plane is shown in figure 3.8. Signals from the GaP substrate, GaAsP linearly graded buffer and the 0.5 μm-thick GaAsP and 0.5 μm-thick GaNAsP are marked in the figure. Starting from the right hand side, a strong signal peak is seen from the GaP substrate. As the linearly graded buffer layer comprises more and more As content, the signal moves to the left hand
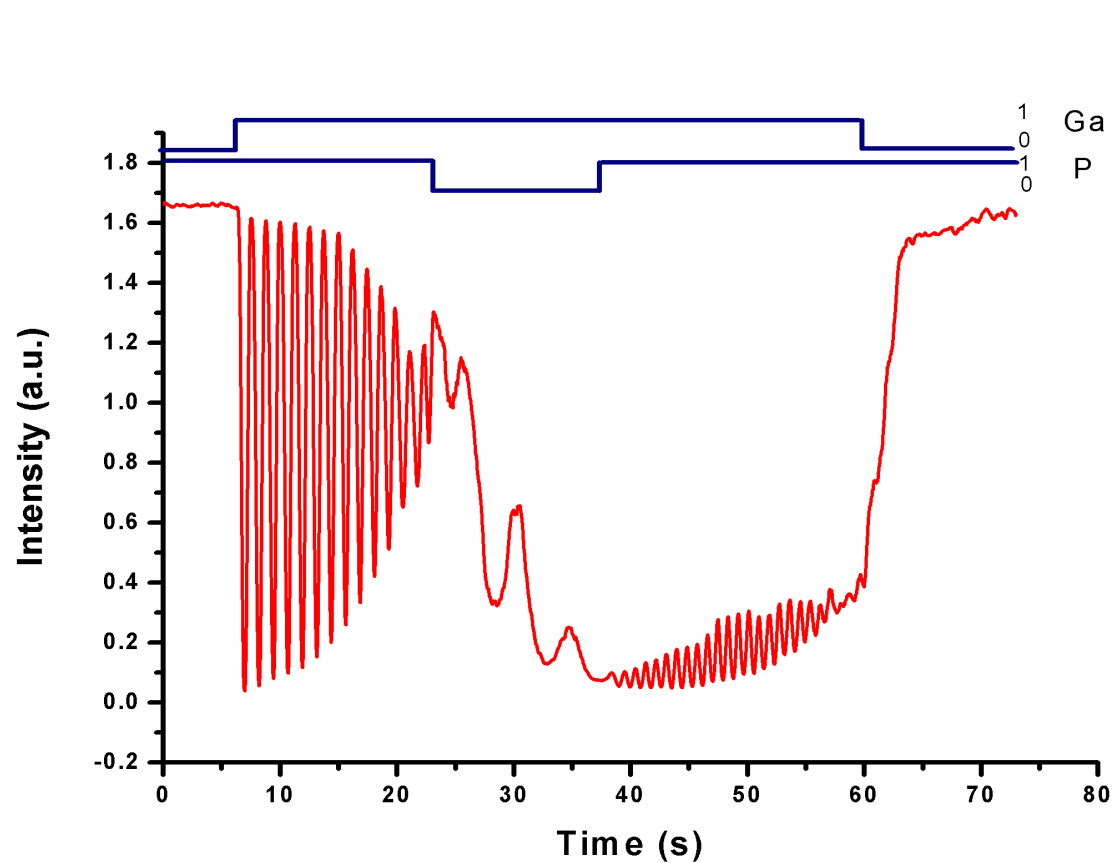
Figure 3.5: Ga and P induced RHEED intensity oscillation. The time series on top show the status of Ga and P shutters, where 0 stands for closed and 1 stands for open. The oscillation with larger frequency before the P shutter open is due to shutter gas leak.
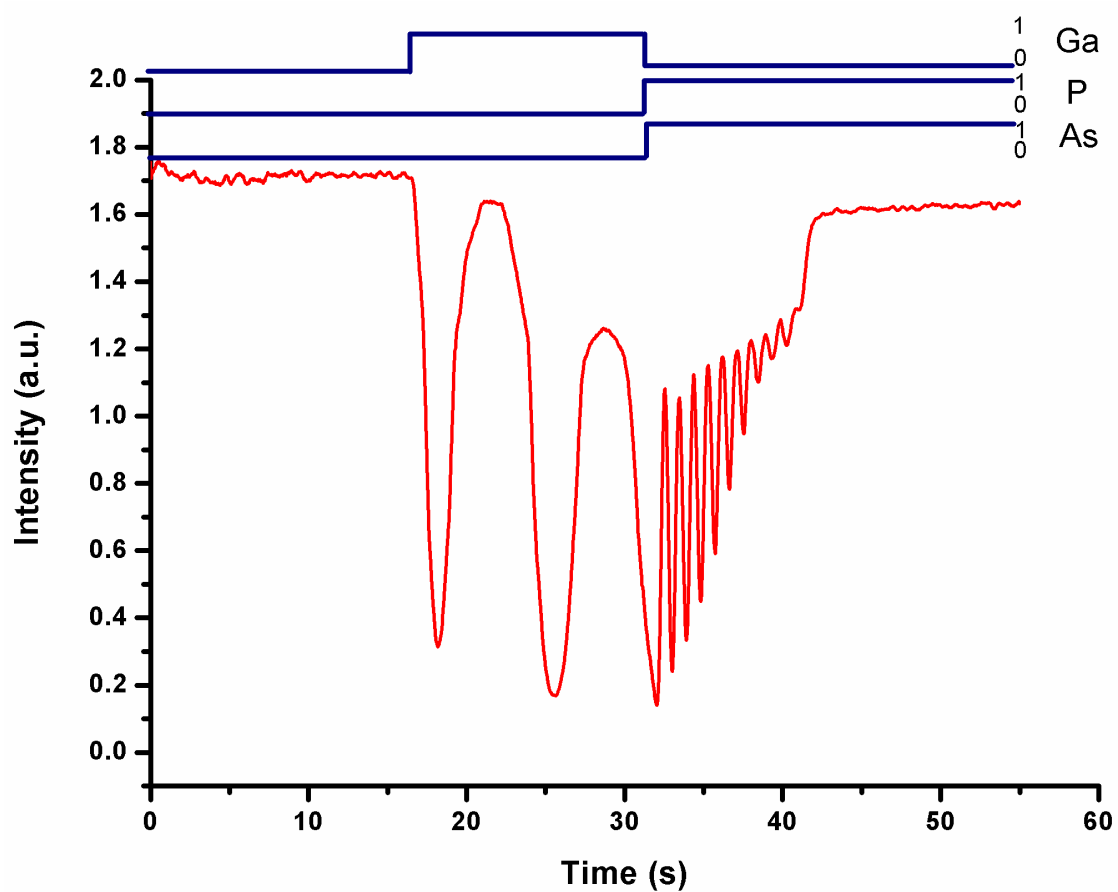
Figure 3.6: As and P induced RHEED intensity oscillation. The time series on top show the status of Ga, As and P shutters, where 0 stands for closed and 1 stands for open. The oscillation with larger frequency before the As and P shutters open is due to shutter gas leak.
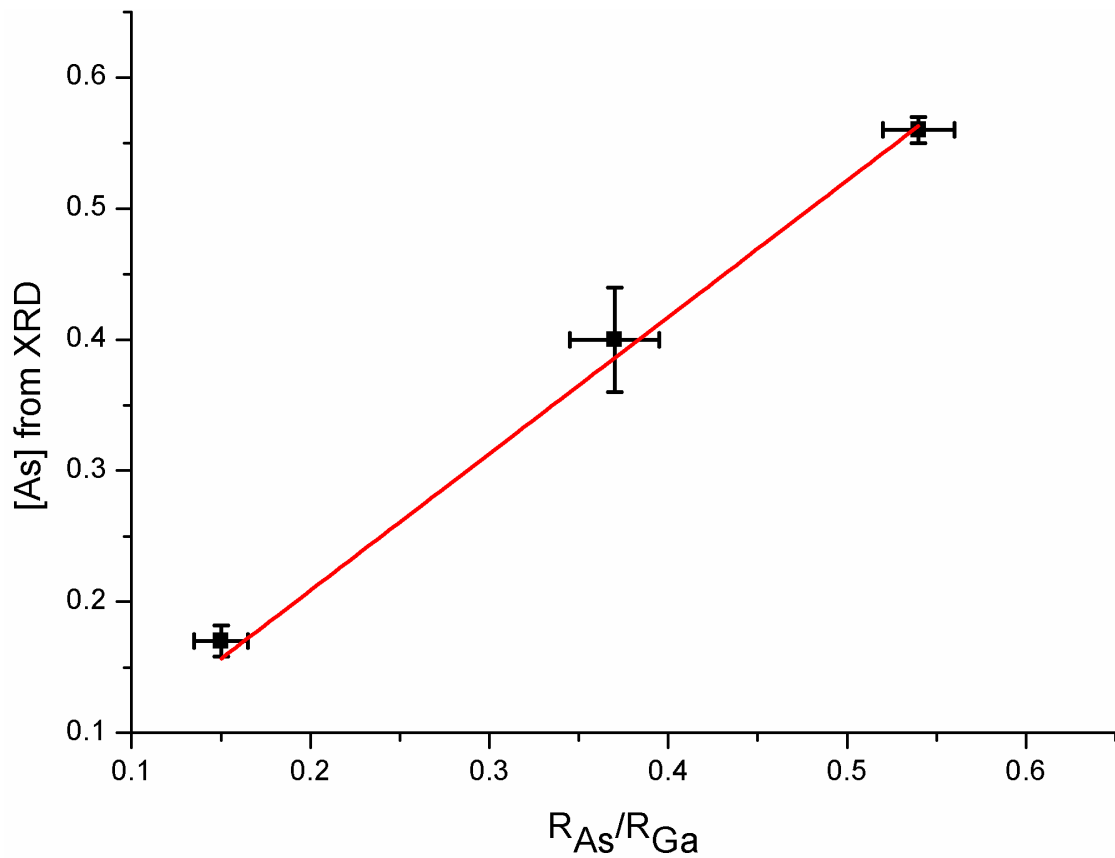
Figure 3.7: The comparison of between As content from in situ RHEED monitoring and that from XRD. The linear fit with 0 intercept and almost unity slope shows a good agreement between the two methods and equation (1) is valid under the condition that As flux is smaller than Ga flux at substrate temperature no higher than 530 $^\circ C$.
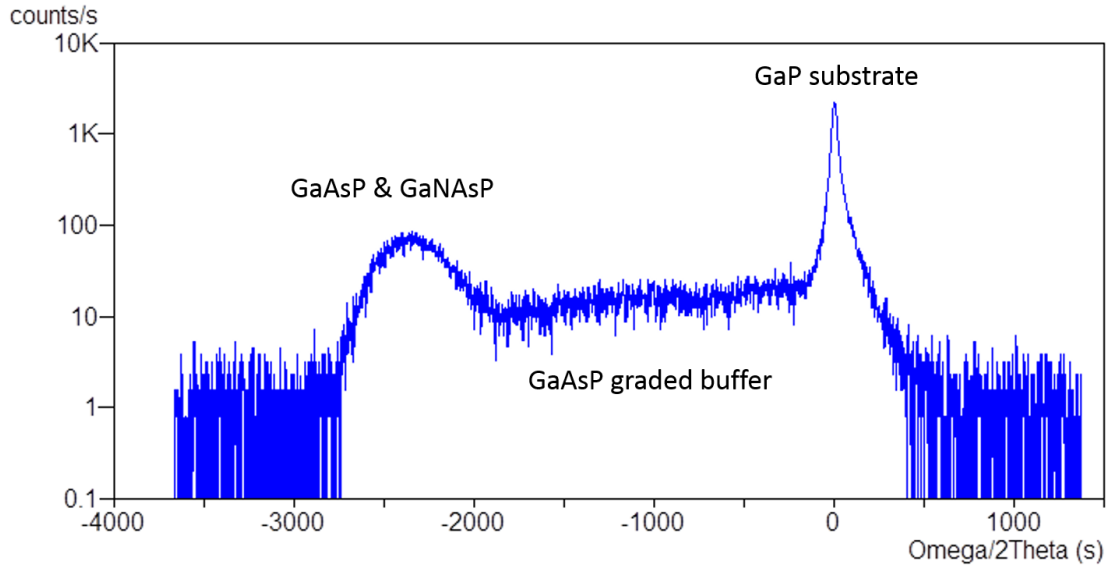
Figure 3.8: X-ray diffraction $\omega/2\theta$ line scan on a GaNAsP sample grown on GaAsP metamorphic buffer.

side towards the GaAs (004) plane signal peak. And after the linearly graded buffer, the GaAsP and GaNAsP peaks are clearly seen. However, the two layers are lattice matched or almost lattice matched to each other, signals from each layer cannot be deconvoluted into two distinct peaks. The strain information as well as composition information cannot be extracted solely from a line scan on the (004) plane since it only contains out of plane crystal lattice structural information. The reciprocal space mapping technique is applied to get the strain and composition.

A set of (224) reciprocal space map (RSM) is shown in figure 3.9, where the black lines are 100% relaxation lines. A mosaic structure resulting from the plastic relaxation that occurred in the metamorphic linearly graded GaAsP buffer can be seen between the GaP layer and the GaAsP uniform composition layer. The pseudomorphic growth of GaNAsP on the GaAsP layer results in a single peak on the reciprocal space maps. A nearly full relaxation is seen along both [110] and [1-10] directions, indicating that the GaAsP layer undergoes a symmetric biaxial relaxation. This is in agreement with the atomic force microscopy (AFM) data showing typical cross-hatch pattern with corrugations along [110] and [1-10] directions (figure 3.10). When a plastic relaxation occurs, an imbalance between the dislocation

glide systems may appear. The occurrence of a tilt of the crystallographic planes can be triggered by such an imbalance. The peak positions in both (004) and (224) RSMs can be significantly affected by the tilt. It further misguides the estimation on lattice parameter. Therefore, adjustment on the tilt must be considered before the lattice constant is derived from the set of asymmetric (224) RSMs [19]. The tilt components can be directly deduced from the (004) RSM by

$$tan(\alpha) = \frac{\Delta q_y^{004}}{\dfrac{4}{a_{substrate}} - |\Delta q_z^{004}|},$$ (3.5)

where Δq_y^{004} is the peak splitting in $< 110 >$ directions measured on the (004) symmetrical map. After the α angle is obtained, the tilt adjustment is done by rotating the diffraction nodes around the (000) origin in both the symmetric (004) and asymmetric (224) RSMs. From the symmetric (004) RSM shown in figure 3.9, the GaNAsP/GaAsP layers are directly below the GaP substrate, i.e., the peak splitting of the diffraction rods, Δq_y^{004}, is zero, indicating no tilt in the epitaxial layer with respect to the substrate. The lattice mismatch in the [001] growth direction can then be calculated by

$$(\frac{\Delta a}{a})_\perp = -\frac{\Delta q_z^{004}}{\dfrac{4}{a_{substrate}} + \Delta q_z^{004}},$$ (3.6)

where Δq_z^{004} is the peak splitting in the [004] directions. The in plane lattice mismatch measured along the [110] or [1-10] directions is given by

$$(\frac{\Delta a}{a})_{<110>} = -\frac{\Delta q_y^{224}}{\dfrac{2\sqrt{2}}{a_{substrate}} + \Delta q_y^{224}},$$ (3.7)

where Δq_y^{224} is the peak splitting on the (224) RSM in the $< 110 >$ directions. If the lattice cell quadraticity prevails, the lattice mismatch f can be calculated by

$$f = (\frac{a_{GaAsP} - a_{GaP}}{a_{GaP}}) = (\frac{1-\nu}{1+\nu})(\frac{\Delta a}{a})_\perp + \frac{\nu}{1+\nu}[(\frac{\Delta a}{a})_{[110]} + (\frac{\Delta a}{a})_{[1-10]}],$$ (3.8)

where ν is the Poisson coefficient. The relaxation information can then be extracted by assuming Vegard's law. Since the As composition has been obtained from
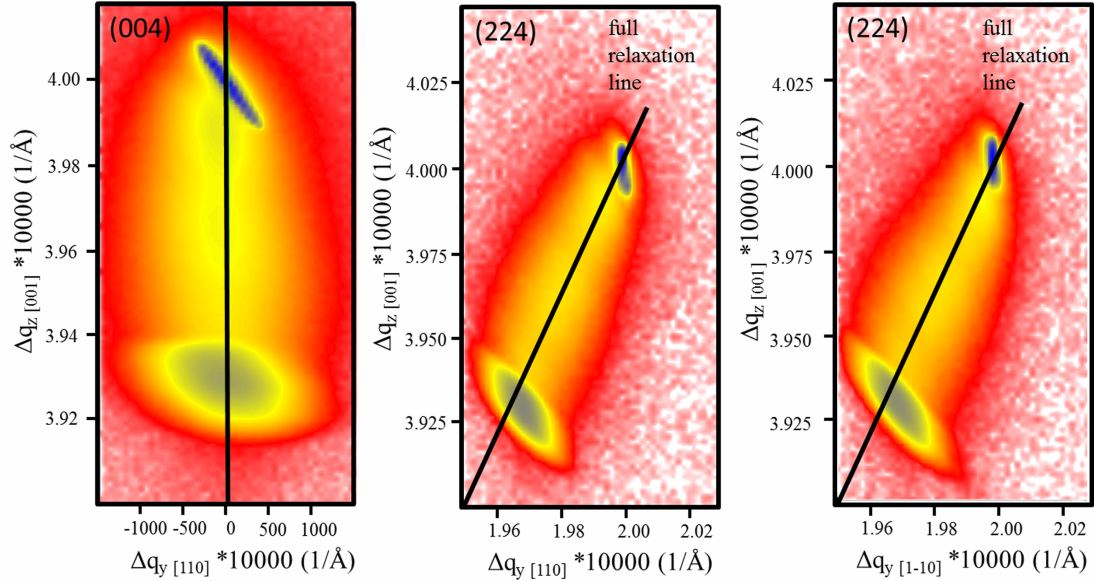
Figure 3.9: a

nd [1-10] directions and symmetrical (004) reciprocal space map.] Asymmetric (224) reciprocal space maps along [110] and [1-10] directions and symmetrical (004) reciprocal space map. The black lines in asymmetric map are 100% relaxation lines and the one in symmetric map is the line scan profile line used to compare to computer simulations.

RHEED intensity oscillation during the growth, the As composition is pre-obtained and it is assumed it should remain the same during the GaNAsP layer growth. The fitting and comparison between (004) symmetrical scan line profile and dynamical theory simulation can finally extract the N composition in the top GaNAsP layer. In the sample of which the RSMs are shown in figure 3.9, the relaxation is calculated to be 98%. By fixing the As content at 56% from RHEED oscillation, a 2.2% is obtain for the N composition.

The in situ incorporation rate monitoring based on group-III and group-V induced RHEED oscillation is of particular importance because it eliminates the need for growing several calibration samples. Unlike the beam equivalent pressure, it provides accurate growth information that is helpful for tuning growth parameters independent of MBE chamber design. However, there are several limitations on such a method. First, group-V induced RHEED intensity oscillation is not as
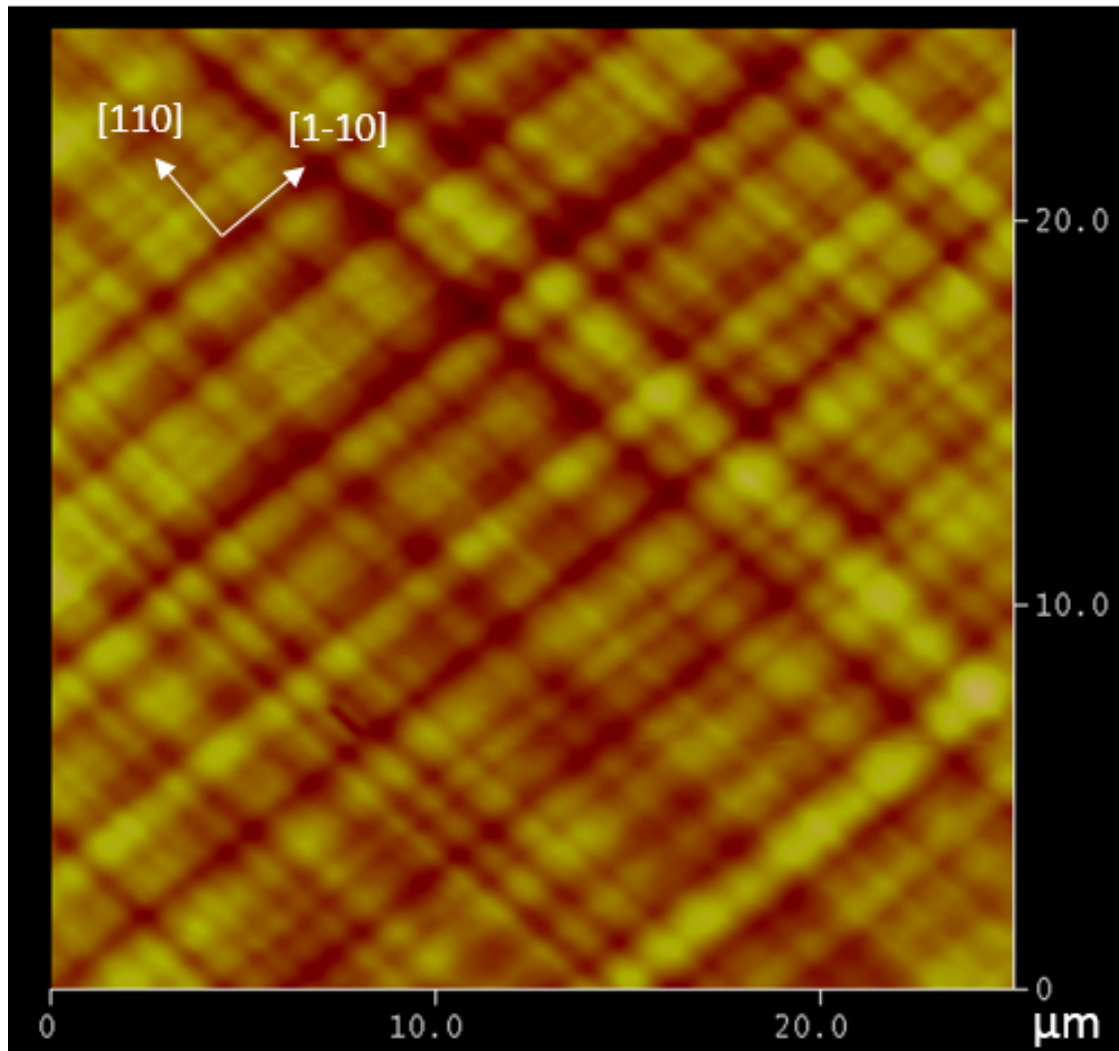
Figure 3.10: A 25 μm full scale AFM scan. The corrugations along both along [110] and [1-10] directions form the typical cross-hatch patterns that indicate bi-axial relaxation.

easily seen as that induced by group-III. Second, thermal desorption is not included in this model and there is a discrepancy between the in situ results and the XRD results when substrate temperature goes higher than 520 $°C$. In this case, ignorance of thermal desorption will overestimate As content and subsequently N content. The discrepancy of the PL maxima with the BAC model suggests that As composition might be lower than what it shows. Third, this method requires established growth kinetic model for mixed group-V species, which is a key point for equation 3.4. Even some of the requirements are stringent, this method opens up a window for composition calibration of multiple mixed group-V materials.

Temperature dependent PL result of this sample is shown in figure 3.11. There are several points that are noteworthy. First of all, the 0.5 μm-thick GaNAsP top layer has PL signal at room temperature but the 0.5 μm-thick GaAsP does not show any PL signal until some temperature between 130K and 77K. And at 12K, a phonon replica can be slightly seen for the 0.5 μm-thick GaAsP peak, indicating the As content in this layer should be below the Γ and X crossover. Second, we can see a blue shift of the peak maximum at 130K from room temperature, followed by red shifts when the temperature reaches lower. Such an inverted S-shape of the peak maximum can be explained by the defect band filling effect [39]. At low temperature, electrons tend to fill the N related defect states in the bandgap when pumped from the valance band; while at higher temperature, electrons have enough thermal energy to hop into the above conduction band whose maxima follows the Varshni model,

$$E(T) = E(0) - \frac{\alpha T^2}{T + \beta}, \tag{3.9}$$

where E(T) is the bandgap at temperature T, E(0) is the bandgap at 0K, and α and β are Varshini coefficients defining the shape of the dependence. As a result, the peak maximum from dilute nitride in general exhibits an inverted S-shape [40]. To improve the optical quality of GaNAsP, specifically, to remove N related defect states that cause a wide band tails on PL spectra, rapid thermal annealing (RTA) is done on this GaNAsP sample. The sample is annealed at a series of temperatures for 60s under forming gas (5% hydrogen balanced with nitrogen).

Figure 3.12 shows the PL improvement for different temperatures along with the as-grown sample. The maximum PL intensity appears at the annealing temperature of 950 $°C$, where band tail is significantly reduced, indicating N related defects are effectively removed and the crystal quality is improved. Further increase in annealing temperature decreases the PL intensity due to generation of thermal process related defects and thermal desorption. Figure 3.13 shows the relative PL intensity improvement as a function of RTA temperature for two GaNAsP samples with different N content. The as-grown sample with higher N content has lower PL intensity due to more N-induced defects. It shows that the higher the N content is in the sample, the higher the RTA optimal temperature is. And the higher the relative PL intensity improvement is. RTA is essential for dilute nitride based solar cell device, as will be discussed in the next chapter, because the introduction of N into the crystal significantly reduces the minority carrier life time and hence the diffusion length. Such an effect is more significant on electron than on holes due to the high electron negativity of N. The introduction of N also introduces anti-site defects that trap or induce recombination for the photo-generated minority electrons, which could otherwise diffuse to the junction and make it to become majority carriers. The optimal RTA condition is later discussed in the next chapter, taking into account the mutual passivation of N and Si doping in the dilute nitride layers.

To further study the effect of RTA on PL, temperature dependent PL study, from 290K to 15K, have been done on an as-grown sample and an RTA sample processed at 950 $°C$, as shown in figure 3.14 and figure 3.15. Blueshifts are seen on all temperature on the RTA sample. The blueshift on GaInNAs after RTA has been attributed to the alteration of the N nearest neighbor environment from Ga-rich to In-rich sites. However, in GaNAsP there is only one group-III constituent and the blueshift is more likely attributed to the decomposition of N paring. The S-curve on peak energy is seen on both the as-grown sample and RTA sample. However, there is a significant difference between the two samples in the temperature range from 150K to 230K. The PL on RTA sample clearly shows a much stronger double-peak feature, suggesting the onset of thermal activation of electron hoping from the N-

related states below the bandgap to the conduction band. Radiative recombination is strong on both the band-band and through lower N-related states transitions. Thanks to the removal of some of the non-radiative recombination centers below the band edge (DD1 centers) by RTA, radiative recombination through lower N-related states is comparable to band to band transitions at the thermal hopping onset temperature (190K and 210K). Once the temperature goes beyond the thermal activation temperature, radiative recombination through band to band transition or N-related states closer to the band edge would become much stronger since lower N states and non-radiative recombination channels are suppressed. This point is manifested by figure 3.16. The peak energy of RTA sample climbs up faster than that of as-grown sample. Such a mechanism causes a more curvy S dip in the peak energy-temperature plot around the activation temperature.

As mentioned in the previous discussion, an in situ As composition determination by RHEED oscillation is quick and convenient. And by knowing the As composition, the N composition can be extracted by RSMs. However, this technique is highly limited by the growth kinetics on the growth front and it is based on a few assumptions, including the As composition calibrated from RHEED oscillation during the beginning of GaAsP growth should stay the same during the GaNAsP layer growth. Group-V induced RHEED oscillation can be clearly seen at a substrate temperature of 520 $^\circ C$ but it is hardly seen below 500 $^\circ C$. The growth temperature for GaNAsP solar cell device cannot be as high as 520 $^\circ C$ because of doping efficiency consideration. The As composition would become obscure at low growth temperature. Therefore, a more accurate method is needed to probe the As and N composition in a GaNAsP sample. The following discussion is devoted to the study of the characterizations on the GaNAsP composition and its optical properties as a solar absorber.

The GaNAsP samples discussed below were grown in a Gen-II MBE system modified to handle gas phase AsH_3 and PH_3 which were thermally cracked to be As_2 and P_2 sources. Elemental Ga and rf-plasma activated N were used as group-III and N sources. Starting from a GaP (100) substrate, a linearly graded GaAsP buffer layer with $\sim 0.03\%$/nm As rate was grown to slowly expand the lattice
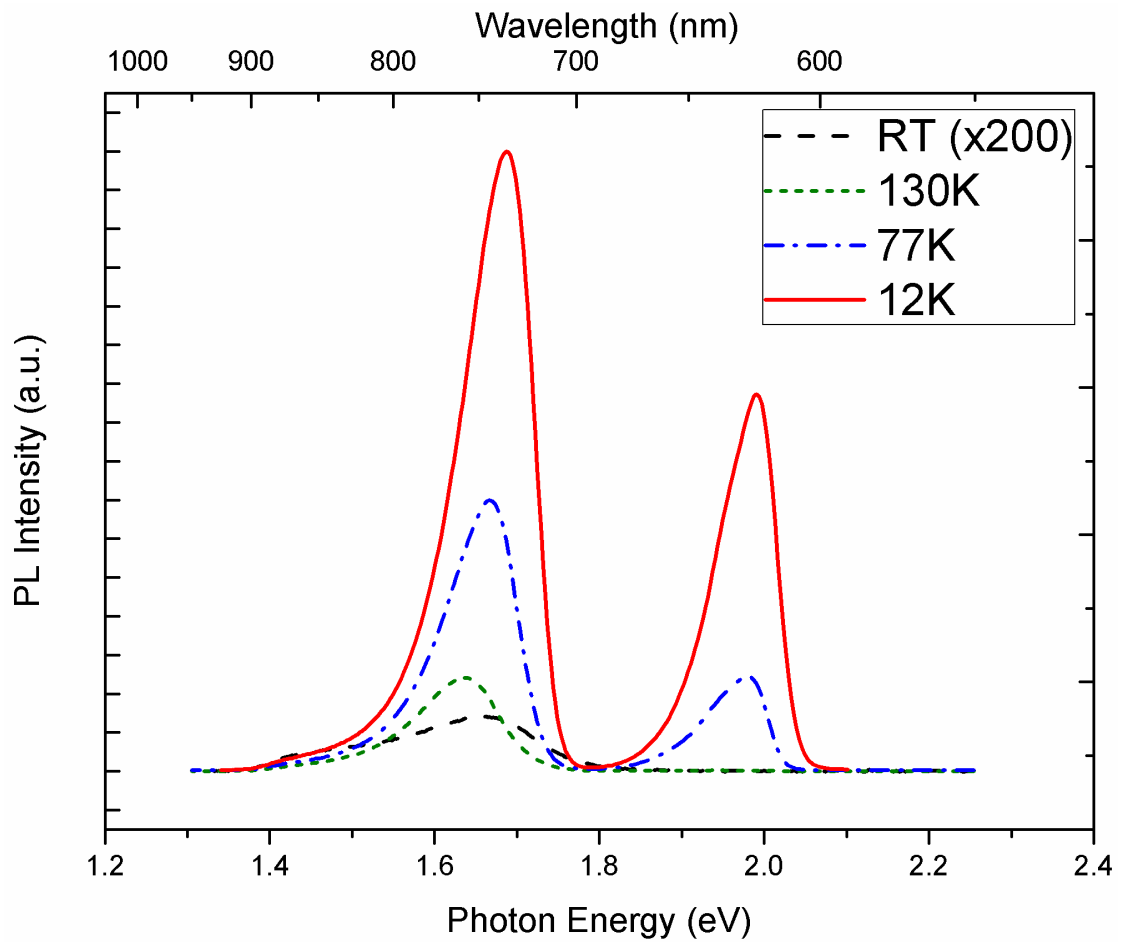
Figure 3.11: Temperature dependent PL (300K, 133K, 77K, 12K). GaNAsP has PL signal at 300K while the GaAsP layer below it has signal only at temperature lower than some temperature between 133K and 77K. Energy maxima of GaNAsP show S-shape characteristic.
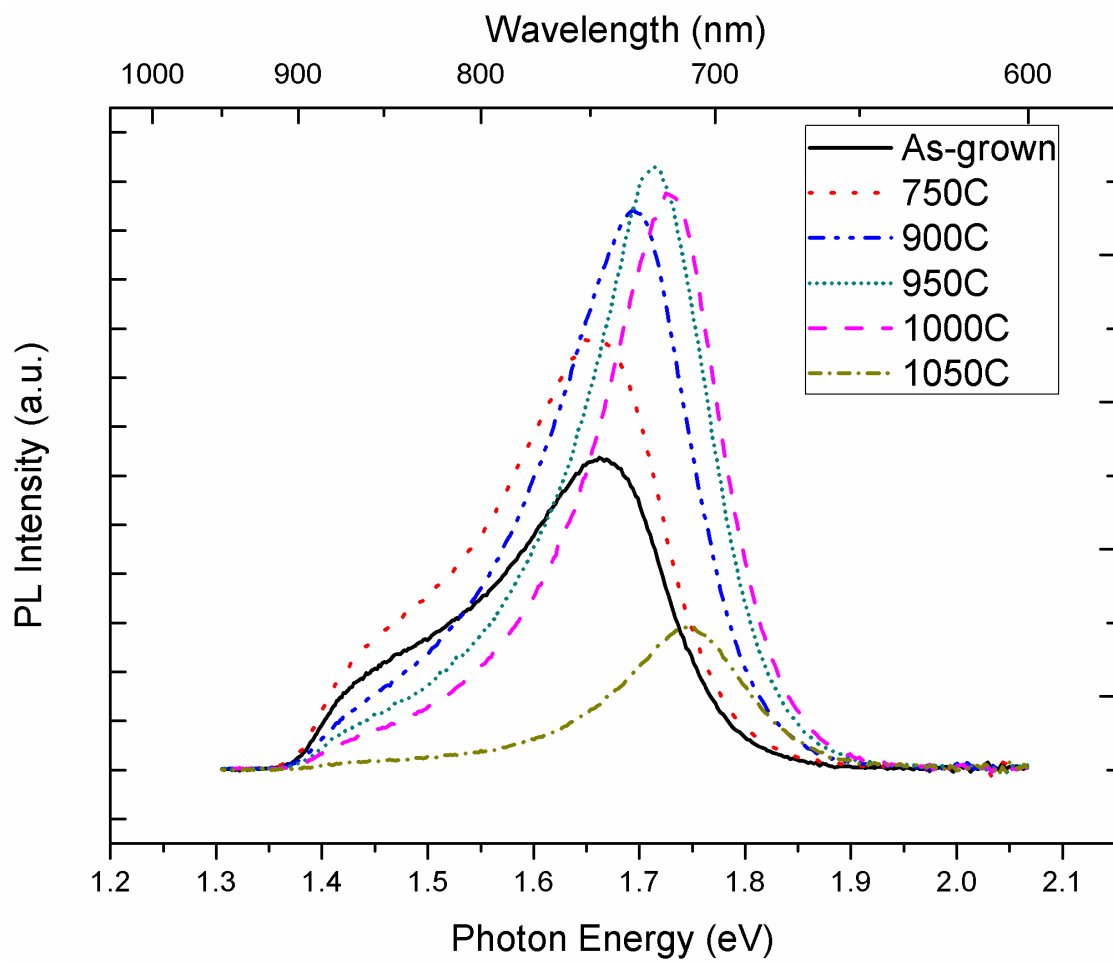
Figure 3.12: PL performance after RTA. For this $GaN_{0.023}As_{0.56}P_{0.417}$, the optimal RTA temperature is around 950 $°C$. Band tail due to N induced defects is significantly reduced.
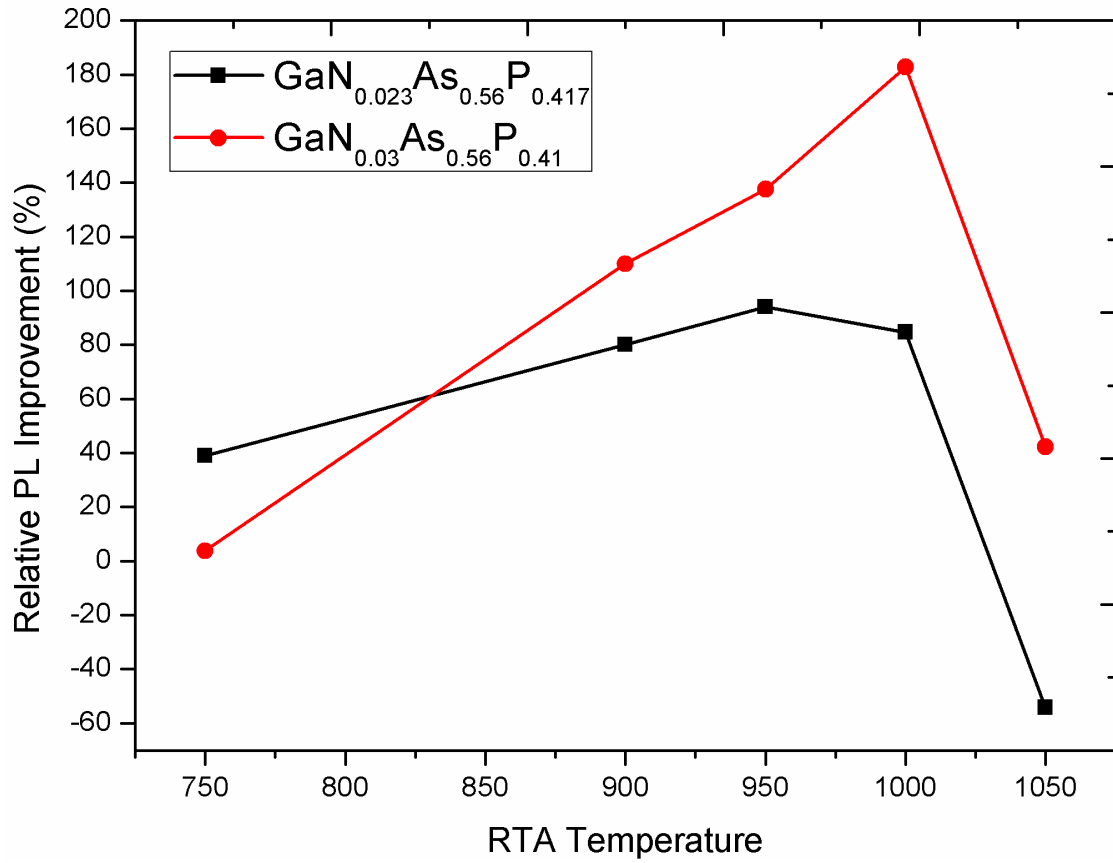
Figure 3.13: Relative PL intensity improvement vs. RTA temperature for two samples: $GaN_{0.023}As_{0.56}P_{0.417}$ and $GaN_{0.03}As_{0.56}P_{0.41}$.
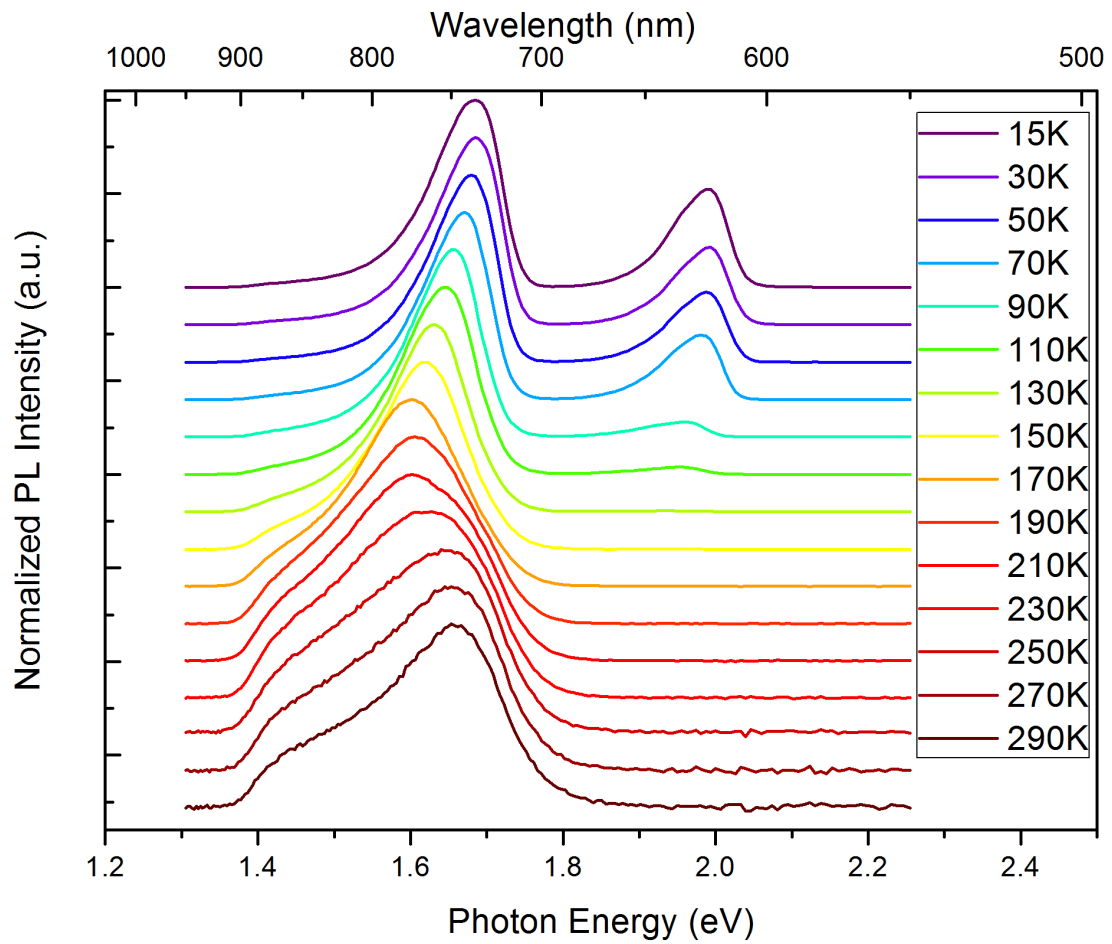
Figure 3.14: Temperature dependent PL on GaNAsP as-grown sample from 290K to 15K. The activation energies extracted from the the reciprocal of the energy peak slope are 95 meV and 131 meV for GaAsP and GaNAsP at 15K.
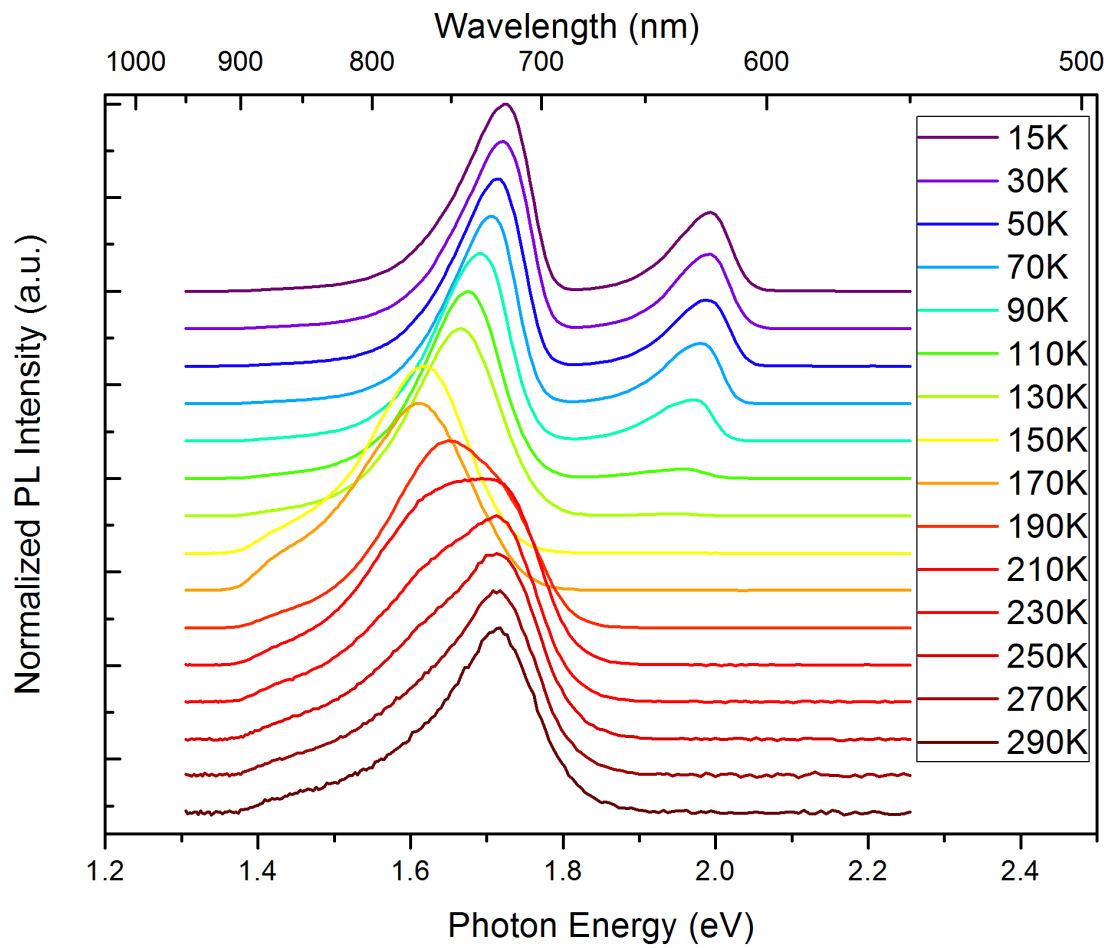
Figure 3.15: Temperature dependent PL on GaNAsP sample annealed at 950 $°C$ from 290K to 15K. The activation energies extracted from the the reciprocal of the energy peak slope are 95 meV and 130 meV for GaAsP and GaNAsP at 15K.
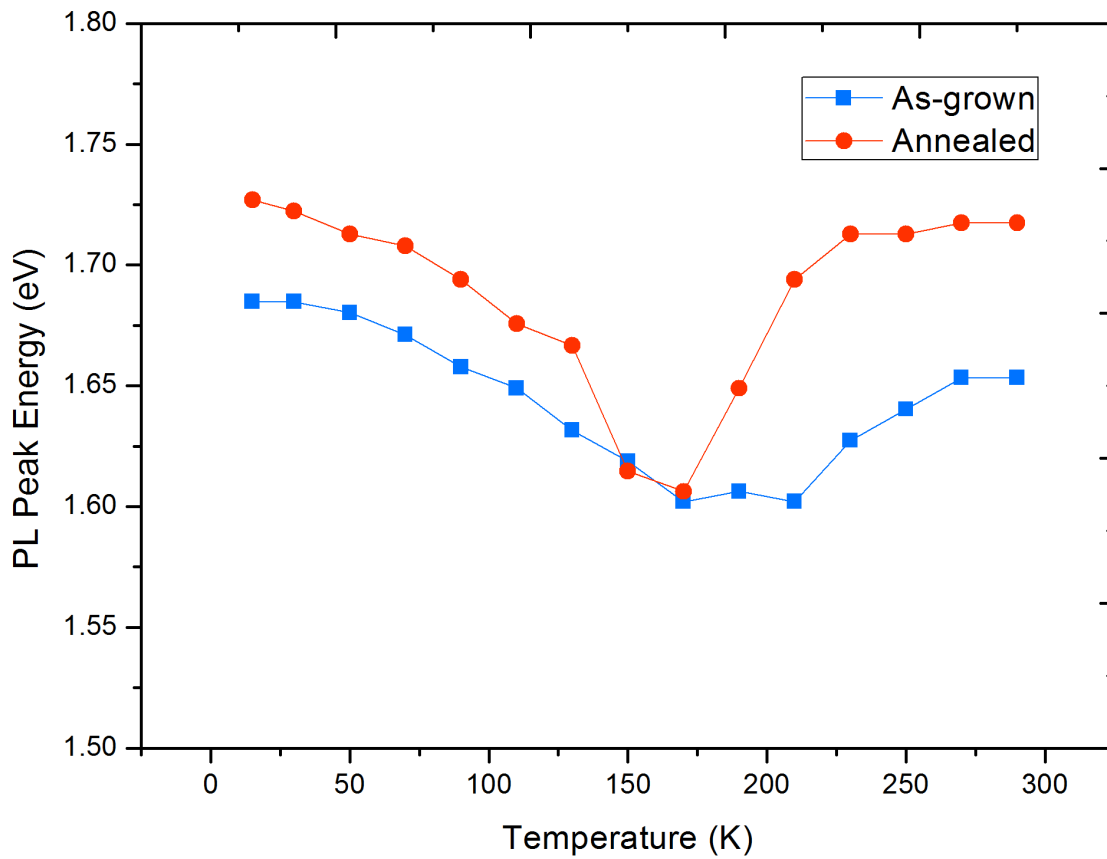
Figure 3.16: PL peak energies across from 15K to 290K.

constant to control misfit dislocations. Then a 0.5μm-thick GaAsP with constant [As] was introduced to relax the residual strain. The structure to this point is referred to as the "template" in the following discussion. Finally, a GaNAsP layer was grown atop the template. Samples with a top layer of GaAsP without N were also grown as the control group. It is important to note that composition of such III-V-V-V quaternary alloys is more complicated to control than the composition of more usual III-III-V-V alloys. In our MBE growth, in situ content measurement technique through group V-induced reflection high-energy electron diffraction (RHEED) oscillation was used to determine the P and As compositions. An example is shown in figure 3.17. Since As-induced RHEED oscillation cannot be seen on a highly strained GaP surface, [As] is calculated by equation 3.4. The N content was then characterized through high-resolution X-ray reciprocal space mapping, as discussed previously. Such preliminarily characterized compositions were indicated in the designed structure in figure 3.19. Throughout the growth RHEED was also deployed to monitor the surface reconstruction pattern to evaluate surface morphology. An example is shown in figure 3.18. After the growth of the linearly graded GaAsP, pattern changes induced by the surface strains can be seen yet the RHEED patterns are still streaky (a and b). After the growth of the constant [As] layer, dotty features appear overlaying on top of the RHEED streaks, indicating that the layer is undergoing a relaxation and surface roughening (c and d). This is in agreement with the RSM discussion above. However, the RHEED pattern streaks recover after the GaNAsP layer growth is finished (e and f). This may be attributed to 1) the lattice quality improves overall leading to a smoother surface after the 0.5μm-thick GaNAsP growth and 2) dilute nitride has been proposed to control misfit dislocations and it helps to improve surface morphology when the misfit relaxation is slowed and threading dislocations are redirected.

Composition profiles of the films were measured by channeling Rutherford backscattering spectroscopy (c-RBS) together with nuclear reaction analysis (NRA). The $^{14}N(\alpha,p)^{17}O$ reaction with a 3.72 MeV $^4He^{2+}$ beam was used for detection of nitrogen. A 150 mm^2 passivated implanted planar silicon (PIPS) detector with a $3 \times 12mm$ slit was used to detect the emitted protons at 135° with
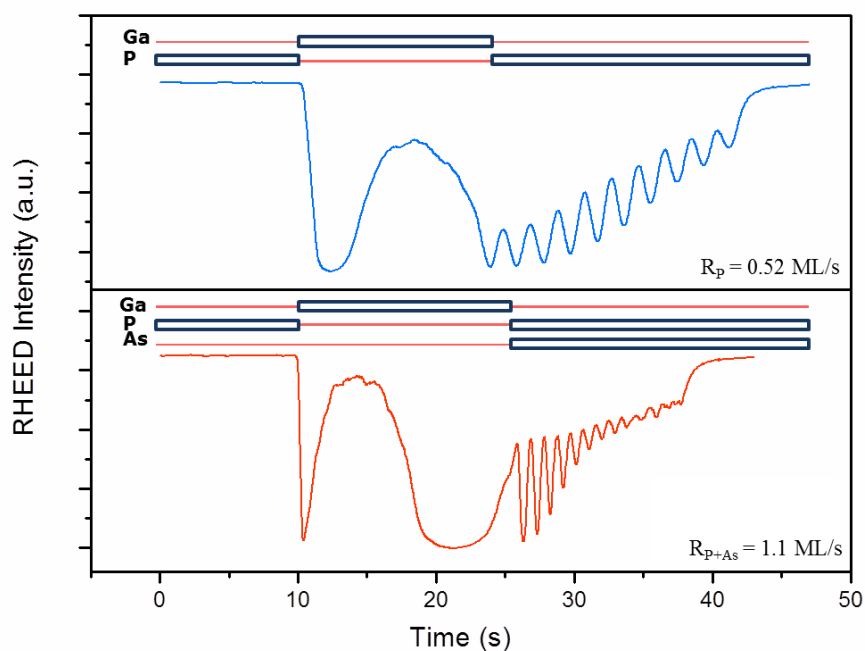
Figure 3.17: Group V induced RHEED oscillation. The top lines indicate the shutter status sequence, with lines (red) as closed and open bars (dark blue) as open. During the time when Ga shutter was open (between 10s and 25s), about 10 monolayers of Ga were deposited on the sample surface. The growth rates of P and (P+As) are then obtained from the quick oscillation period after group V shutters were open. The much slower oscillations (big bumps) during the Ga shuttle opening come from inevitable group V gas leak since they are gas sources.
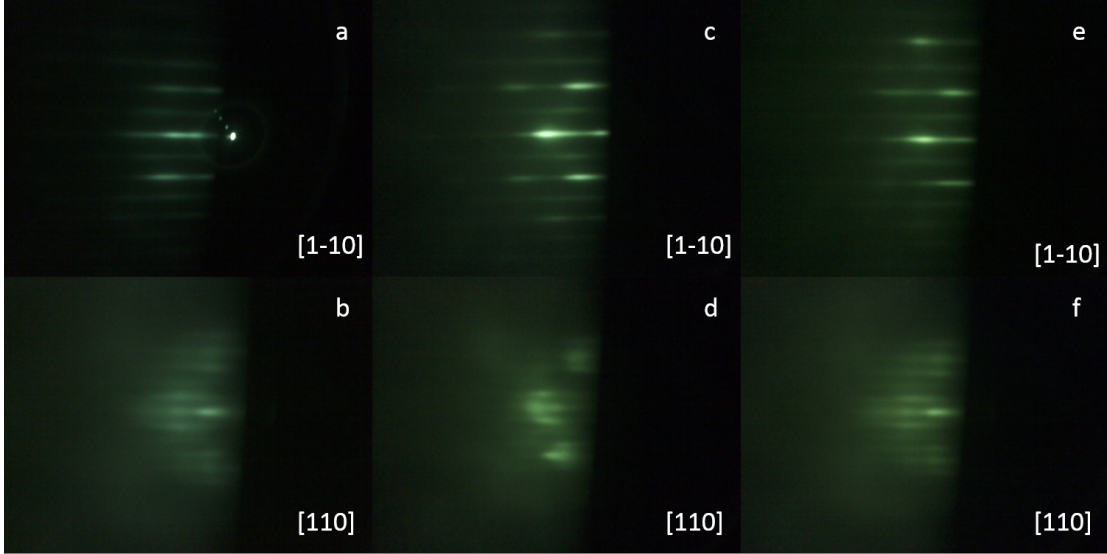
Figure 3.18: RHEED pattern of the (2×4) surface reconstruction during the growth of Ga(N)AsP. a and b: RHEED patterns after the linearly graded GaAsP buffer growth. c and d: RHEED patterns after the GaAsP relaxation layer growth. e and f: RHEED patterns after the GaNAsP layer growth.

respect to the incident beam. A 25μm-thick mylar foil was placed in front of the detector to absorb the backscattered alpha particles. RBS spectra were also obtained simultaneously at $168°$ with another PIPS detector. Both RBS and NRA measurements were carried out in random and $< 100 >$, $< 110 >$, and $< 111 >$ axial channeling directions. The fraction of substitutional nitrogen atoms in the films was obtained by comparing the random and channeling yields of the RBS and the NRA measurements. Figure 3.19 shows the design schematics and atomic profiles of the structure of one of our samples as determined by fitting of the RBS results using the SIMNRA and SIMTarget software packages. The channeling c-RBS shows that samples grown in such a structure are of good crystalline quality with minimum channeling yield of $\sim 5\%$. The linear increment of As content are well distinguished from 0 in the GaP substrate to $\sim 40\%$ at the graded buffer end. The [As] in the top GaN$_x$As$_y$P$_{1-x-y}$ layer is $\sim 54\%$ and the [N] is $\sim 1.5\%$, as compared to 62% and 2.2% by RHEED oscillation and x-ray diffraction, respectively. Channeling RBS and NRA revealed that the substitutional N fraction is $\geq 80\%$ for all samples.
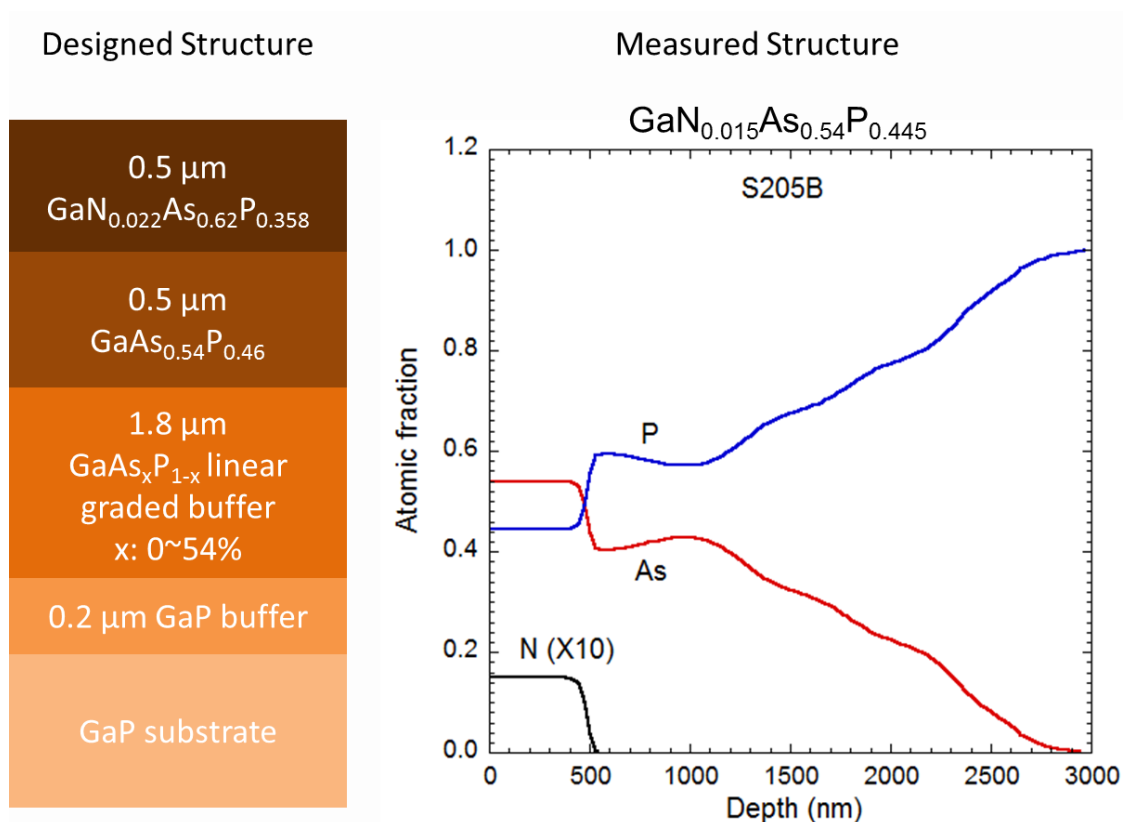
Figure 3.19: The designed structure (left) of GaNAsP and the measured composition profile by Rutherford back scattering spectrometry and nuclear reaction analysis (right).

The discrepancy in the As content determined from RBS and RHEED oscillations combined with x-ray diffraction comes from the assumption that all the As adatoms react with Ga adatoms before the rest of Ga atoms reacts with P atoms (the As flux was kept smaller than the Ga flux throughout the growth). The measured atomic profiles reveal that at the growth front As and Ga reactions are influenced by the impingement of P flux at the sample growth temperature of 520 $^{\circ}C$. Since the As-induced RHEED oscillation could be not directly observed due to the highly strained surface the As incorporation rate was indirectly obtained by subtracting the P incorporation rate from the measured P+As incorporation rate. The As content was overestimated by 8% in this case. The overestimation of As content leads to an overestimate of [N] to compensate for the lattice constant in x-ray diffraction simulation. Although not perfectly accurate, the in situ [As] and [P] monitoring provides an overall guidance for composition control in this III-V-V-V alloy growth, where the usual growth control by solely beam flux tuning and post-growth x-ray characterization is laborious and unreliable. Furthermore, once the offset between in situ RHEED and channeling RBS As content is determined, it can be used as as a reference for later growth runs under similar conditions.

Research has shown that the non-substitional N atoms can form N2 clusters, N-(group V) or N-N defect complexes [41] that usually act as non-radiative centers. The detrimental effect of N-(group V) bonding defects on optical quality have been recently confirmed by Ishikawa et. al. using x-ray photoelectron spectroscopy [42]. In general the fraction of non-substitutional N atoms depends on the growth temperature. Our high substitutional N fraction (≥ 80 %) suggests that our growth temperature is in the right regime. In addition there is no indication that N incorporation behavior is affected by mix of two group V beam fluxes (As and P) in the arsenide-phosphide compound, compared to single group V beam fluxes during the growth of ternary GaNAs [43] or GaNP [44] alloys. The highly non-equilibrium growth condition makes MBE a very effective technique to incorporate N in GaAsP, compared to previously reported results from ion-implantation and pulsed laser melting method [45].

We have used a number of experimental techniques including PL, pho-

toreflectance (PR) and photoabsorption (PA) to study optical properties of the GaNAsP samples. Figure 3.20 shows the room temperature PL of $GaN_{0.015}As_{0.54}P_{0.445}$ sample (S205B) along with a reference $GaAs_{0.59}P_{0.41}$ sample (S205A). At this As composition in GaAsP sample the minimum at Γ point is located at about 2 eV above the valence band edge and slightly below the minimum of the X band. The incorporation of N results in admixing of the Γ component to the lowest CB states, enhancing the oscillator strength for radiative recombination that significantly increases the PL intensity of the dilute nitride sample (S205B). N also redshifts the PL peak, broadens the line width and heaves up a band tail on the low energy side, which is believed to be a thermal distribution of N-related states below the newly formed conduction band edge (E_-). However, the PL peak position coincides with the E_- signal from PR that generally detects band to band transitions (Figure 3.21). Although the N level lies below the Γ valley in both GaP and GaAsP within composition range aforementioned, this good agreement indicates that the major contribution to PL is not attributed to recombination of excitons trapped to N-related deep centers below the bandgap but to band-to-band transitions. This can be further elaborated by the synchronized blueshift of the PL peak position and E_- position on the sample subjected to rapid thermal annealing (at 900 $°C$ for 60s in 95% N_2 and 5% H_2 forming gas ambient). The 3-fold increase in PL intensity suggests that N-related centers do exist in the as-grown sample but mainly serve as non-radiative recombination centers, and RTA effectively removes them and suppresses the non-radiative channels.

PR was performed on the same sample group with the modulation of band bending by the 442nm line from a HeCd laser. In the GaAsP sample, only two transitions are seen, i.e., from valance band to conduction band and from split-off (SO) band to conduction band. In the GaNAsP sample, however, the interband transitions valance band $->E_-$ and valance band $->E_+$ as well as their SO counterparts are clearly resolved in the PR spectrum (figure 3.21). According to the BAC model 3.1, the theoretical values of E_- and E_+ for S205B are plotted as grey bars in figure 3.21. By using the linear interpolated values for matrix conduction band, N energy level and interaction coefficient based on previously
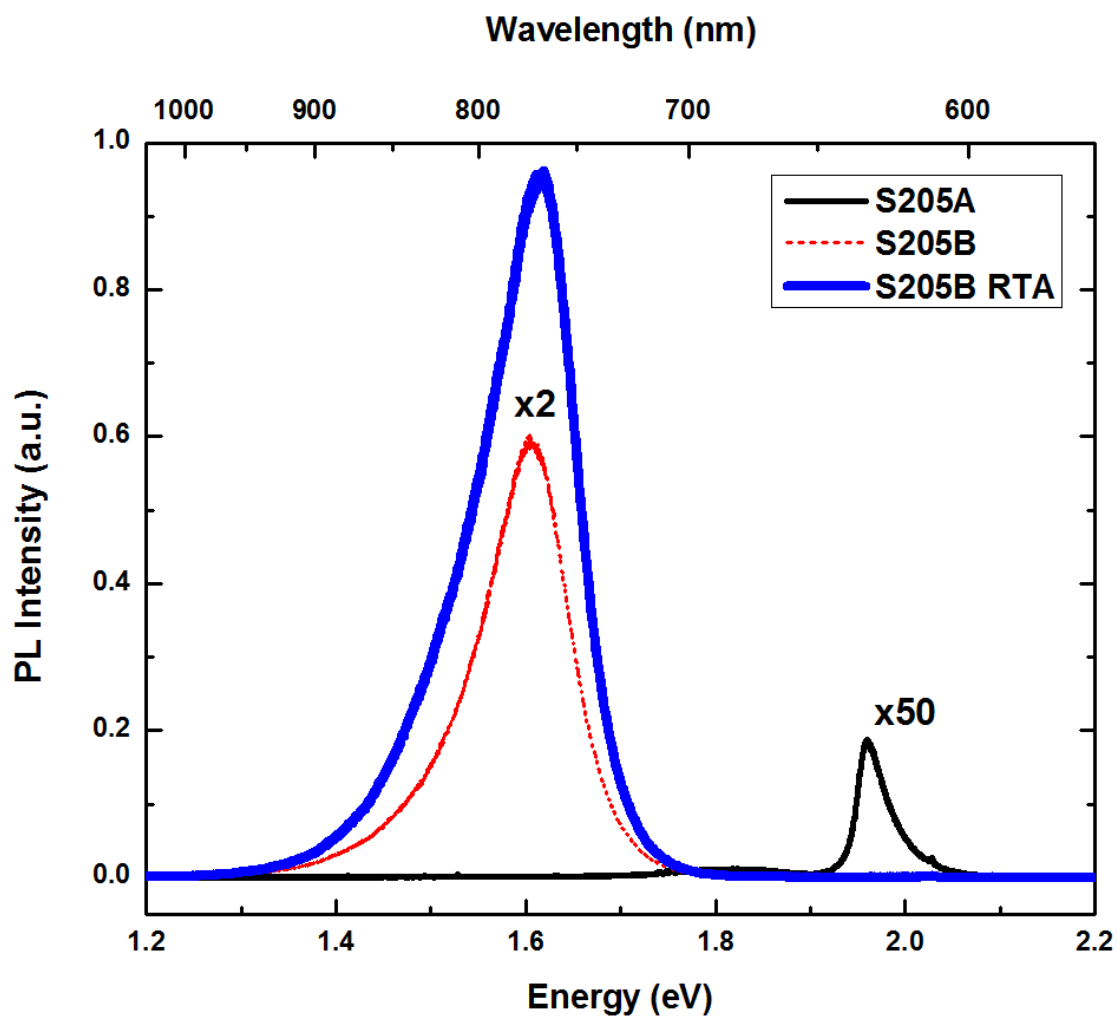
Figure 3.20: Room Temperature photoluminescence of GaAsP (S205A), GaNAsP (S205B) and GaNAsP after rapid thermal annealing (S205B RTA).

well-studied GaNAs and GaNP, (E_-, E_+) from BAC agree well with experimental results. This has an important technical implication since the IB solar cell efficiency changes drastically as (E-, E+) varies. From the material growth perspective, the well predicted (E_-, E_+) by the BAC model greatly decreases the difficulty in IB position tuning, hence makes it easier to grow the material in the optimal compositions.

Figure 3.22 shows the absorption coefficients of the same sample group, both of which show multiple absorption edges corresponding to different layer in the samples. In the GaAsP sample (S205A), absorption takes off at 1.95eV, from the $\Gamma_V - \Gamma_C$ transition, in good agreement with the PL data. The small amount of N incorporation clearly redshifts the absorption edge from ~ 1.95eV to ~ 1.6eV in S205B. The position of the absorption edge also is in good agreement with the PL and PR data, suggesting its origin from the valance band $->E_-$ transition. Note that for all of our GaNAsP samples the intermediate band (E_- band) exhibits strong absorption with $\alpha > 2 \times 10^4 cm^{-1}$. This suggests that using GaNAsP layers as the absorber in an IB solar cell requires only a layer thickness 1 μm. The PR spectra along with PA spectra clearly demonstrate the intermediate band behavior of GaNAsP sample.

To evaluate the RTA effect on the optical quality improvement of Ga(N)AsP samples, the PR and PA are compared side by side in figure 3.23. As is shown in figure 3.23 a significant reduction of the linewidth is observed in the PR spectra of annealed GaNAsP layers. Narrowing of optical transitions in modulated reflectance spectra was also observed for other dilute nitrides and has been attributed to an improvement of the alloy homogeneity and/or reduction of point defects in these layers. Note that RTA causes not only a blueshift on E_- but also a redshift on E_+. This may also be attributed to the decomposition of the N pairing. Since the conversion efficiency of a GaNAsP-based solar cell is sensitive to the E_+ and E_+ levels, it is suggested the RTA effect should be taken into account when the composition of As and N are designed.
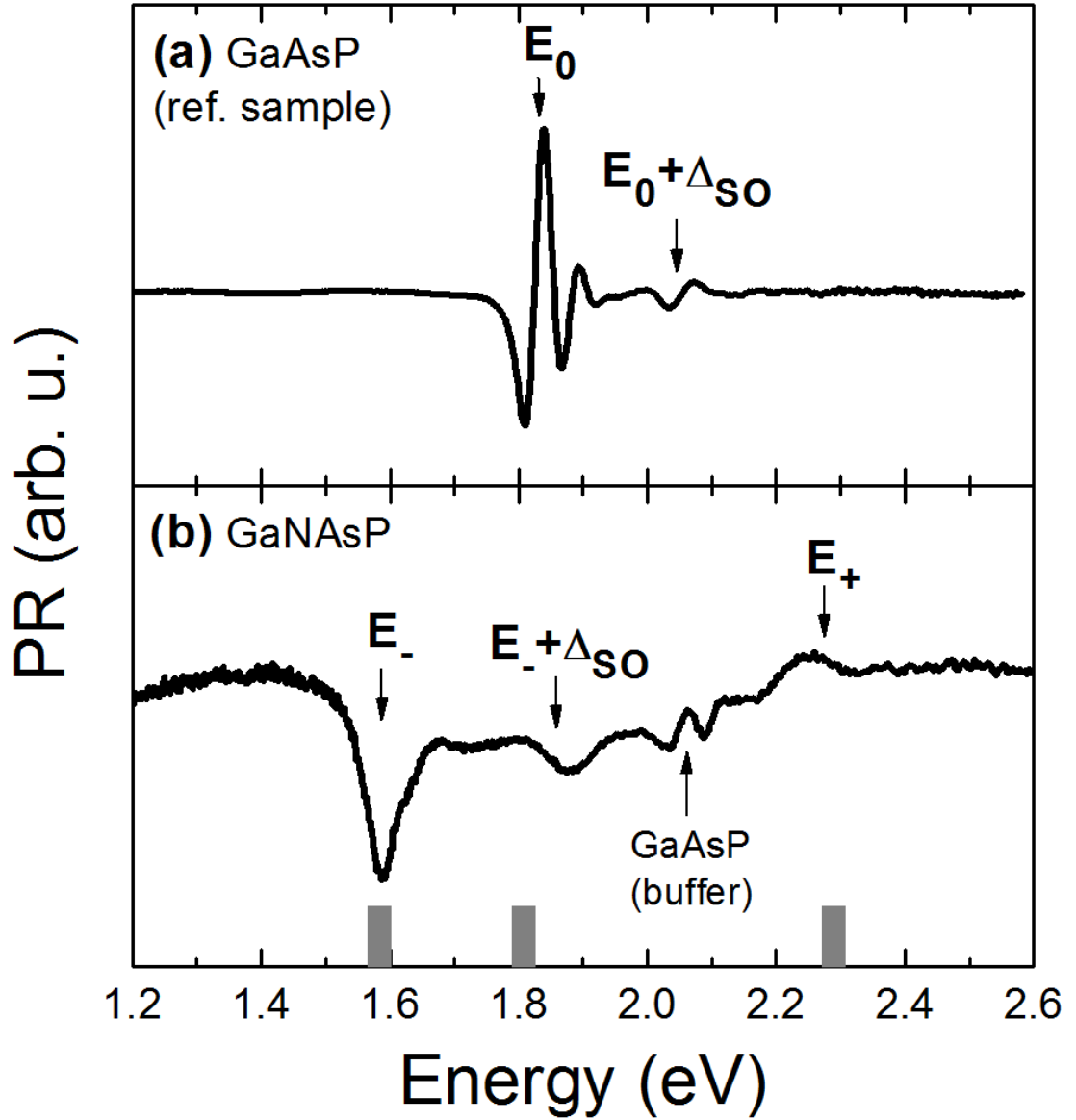
Figure 3.21: Photoreflectance spectra of a GaNAsP sample (b) and a reference GaAsP sample (a). The grey bars show energies of optical transitions in GaNAsP predicted within the BAC model with E_N=1.86eV and C_{NM}=2.84eV obtained by linear interpolation of BAC parameters for GaNAs and GaNP.
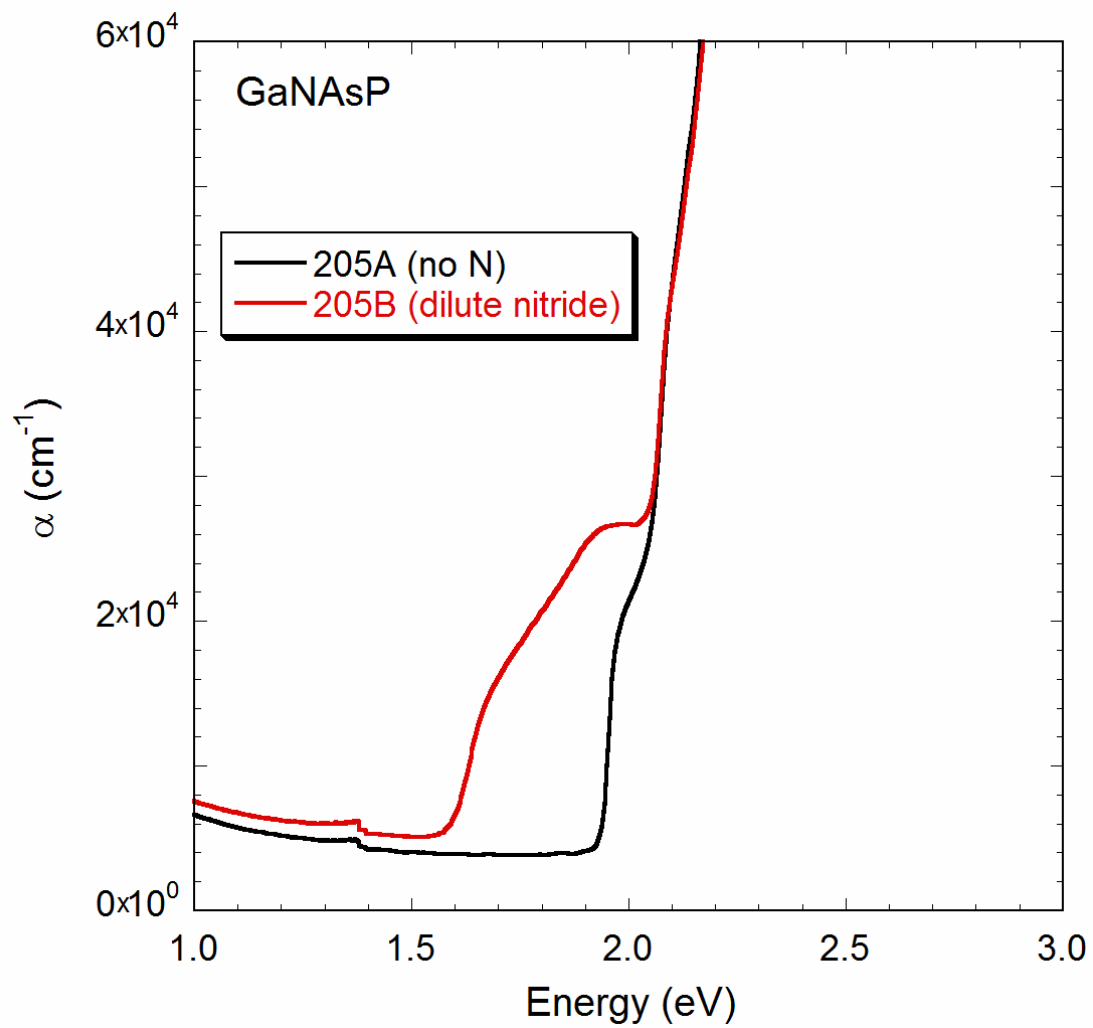
Figure 3.22: Absorption coefficients of GaAsP (S205A) and GaNAsP (S205B) samples.
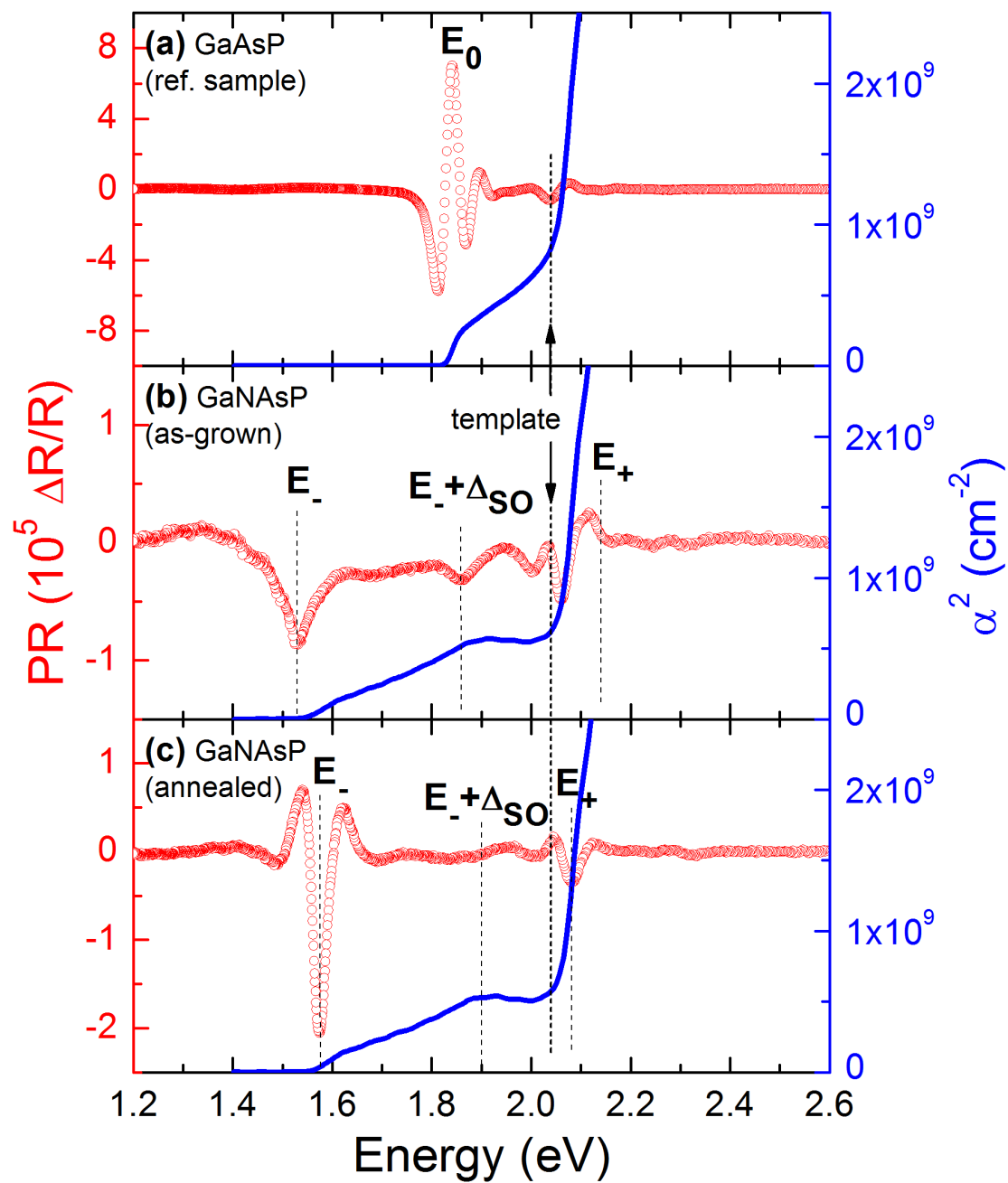
Figure 3.23: Room temperature photoreflectance and absorption spectra for $GaAs_{0.62}P_{0.38}$ (a), as-grown $GaN_{0.012}As_{0.608}P_{0.38}$ (b), and annealed $GaN_{0.012}As_{0.608}P_{0.38}$ (c) samples.

3.4   Conclusion

GaNAsP has clear advantages over GaNAs as an IBSC material with a narrow and well-separated IB. The GaNAsP alloy bands, E_+ and E_+, can be well modeled and predicted by BAC model and based on the calculation of these two energy levels the desired As can N are marked out on a band energy contour map as a guidance for material growth. GaNAsP was grown by GSMBE through a GaAsP metamorphic buffer on GaP substrates. In situ RHEED monitoring, RSMs, AFM, and Channeling NRA-RBS were used to measure and characterize the structural properties and surface morphology of the GaNAsP films while PL, PR and PA were used to characterized the optical properties. All these measurements have confirmed that GaNAsP films grown with such a metamorphic structure are of high quality and clearly demonstrate the intermediate band characteristics. The high absorption coefficient of the IB suggests that this material is suitable as an absorber for IB solar cell application.

3.5   Acknowledgment

4 GaNAsP intermediate band solar cell device

Things out of hope are compass'd oft with venturing.

—William Shakespeare

4.1 Overview

This chapter is devoted to the GaNAsP intermediate band solar cell (IBSC) device design, growth, fabrication and testing. There are a variety of requirements on the device structure given IBSC's specialty. The IB needs to be half-filled so that there will be electrons available to be promoted from IB to the conduction band and available states to receive promoted electrons from the valence band. Such a requirement leads to high doping in the n-region of the p-n junction. Some preliminary doping experiments on GaNAsP and GaNAs lead to a systematic study on the low doping efficiency for Si in dilute nitrides. Lattice constant, band structure and alignment also has to be well designed, so that misfit dislocations are controlled and the IB is well isolated from the adjacent layer's conduction band to prevent electron tunneling. For fabrication, both metal and liquid contacts are used and the one with higher current density is chosen. Iterations on device structures have been run to optimize device performance. This chapter will address the above topics one by one.

4.2   Intermediate band solar cell device design

In chapter 3, some requirements on the material for IBSC, such as narrow IB and band energy spacing, are discussed. The N and As composition range is pinned down. Besides the general requisites for solar cells, to make a GaNAsP based IBSC the following guideline on device structure design needs to be followed.

1. The IB is half-filled. This is a basic requirement for an IBSC device to exhibit IBSC effect. If the IB is not occupied by electrons, the transition from the valence band to the IB could still take place but these electrons generally have a life time on the order of ns. They are either swept away by the internal electric filed in the junction or recombine before a two-photon absorption process can take place that promotes these electrons onto the conduction band. On the other hand, if the IB is fully occupied by electrons, the transition from the valence band to the IB could not occur due to the lack of available states. Therefore, the doping in the IB region in an IBSC has to be carefully chosen. It implies that the Fermi level should be placed above the E_- band edge in GaNAsP. In other words, the absorber region will be degenerately doped by n-type dopants, since the E_- band is still acting as the fundamental bandgap in GaNAsP. A calculation done by the Fermi integral indicates that it takes a doping level from low-$10^{19} cm^{-3}$ to mid-$10^{19} cm^{-3}$ to make the E_- an effective IB with a sufficient population of electrons.

2. The quasi-Fermi level of IB is well separated from those of the conduction band and the valence band. This requirement is mainly to preserve a high V_{OC} of an IBSC. The open circuit voltage, V_{OC}, is determined by the splitting of the quasi-Fermi level of the conduction band and the valence band. If the quasi-Fermi level of an IB is connected to the quasi-Fermi level of the conduction band or the valence band of the adjacent layers, those electrons with higher potential energy in the conduction band of the IB region will firstly take a downward transition to the lowest quasi-Fermi level before they are collected by the electrodes. Quantum dot IBSCs generally suffer from this because of the strong thermal connection at room temperature between the quasi-Fermi level of the IB (ground states of the

quantum dot confinement states) and the conduction band [46]. In the case of GaNAsP, the IB is well below the conduction band so thermal connection with the upper conduction band is not an issue. However, the IB also has to be separated from the conduction band in the adjacent layer and an electron blocking layer needs to be inserted.

The 1st guideline is basically a doping requirement and the 2nd guideline involves bandgap engineering. Both lead to interesting studies on the GaNAsP material nature. The following sections will focus on how to achieve high doping in dilute nitides and effective electron blocking in the IBSC device. To simplify the study on Si doping efficiency in GaNAsP, simulations and experiments were based on GaNAs. Since similar results were actually seen in GaNAsP and As adatoms were not directly involved in the study, the conclusion drawn from the study on GaNAs could be directly applied to GaNAsP.

4.3   Doping in dilute nitride

The study on n-type doping in dilute nitrides has led to interesting findings. Since N has a much larger electron negativity (3.04) than its counterparts (2.19 for P and 2.18 for As)[47], electrons are subjected to severe scattering and behave differently than their conjugate, holes. Hence the mobility of electrons plummets by an order of magnitude even for a small atomic fraction of N in the crystal [48]. More interestingly, Yu et. al. reported a drastic decrease of free electron concentrations and a slight increase of bandgap in GaNAs:Si after post-growth rapid thermal annealing (RTA) [49]. They proposed a mutual passivation model that Si atoms are mobilized during annealing to form bonds with N, turning into Si-N defect complex which sacrifices the free carriers and reducing the effective portion of N. Li et. al. believed that it is $Si_{Ga} - N_{As}$ that is formed during RTA based on a super cell simulation [50], while Janotti et. al.s proposed a $(Si - N)_{As}$ split interstitial model which is more energetically favorable and reasonably accounts for the 0.8eV photoluminescence (PL) peak observed on the annealed samples [51]. Early studies on GaAs:Si have suggested that both V/III ratio and growth

temperature will affect Si doping efficiency based on the law of mass action [52]; however, they cannot account for the amount of efficiency decrease observed in our GaNAs samples as well as those in the literature [53, 54]. In this section, we apply the mutual passivation model to the growth surface and calculated the doping efficiency by Monte Carlo simulation during molecular beam epitaxy (MBE), where the number of $(Si - N)_{As}$ is calculated. The simulation results are compared to experimental results of doping efficiency. It is believed that the encounter of N with Si during N adatom surface diffusion mainly contributes to the drastic decrease in Si doping efficiency.

All samples studied were grown in a Varian Gen-II MBE system modified to thermally cracked gas-phase AsH_3 to As_2 and H_2. Elemental Ga, solid Si and rf-plasma activated radical N were used as group-III, n-type dopant and N sources. A 200-nm-thick undoped GaAs buffer was grown on a semi-insulating GaAs substrate for all samples before the Si-doped N-containing layer was grown at various temperatures ranging from $460°C$ to $570°C$. The V/III incorporation ratio was kept at $\sim$1.5 for all samples while the N flow rate was varied from 0.45 sccm to 1.2 sccm to change the N composition. N composition was characterized by high-resolution x-ray diffraction in the (511) asymmetric reflection geometry [55]. GaAs:Si samples were also grown to calibrate Si doping level for various Si cell temperatures as a reference. Predicted doping levels in GaNAs:Si samples, based on the GaAs:Si calibration, varied from mid-$10^{17}cm^{-3}$ to low-$10^{18}cm^{-3}$, below the auto-compensation limit for GaAs:Si [52]. Such a limit can be exceeded by increased As_2 flux and low growth temperature techniques [56, 57, 58]; however, our study tried to minimize the decreased doping efficiency effect from the amphoteric nature of Si and concentrate on the effect of N passivation on Si. Therefore, Si fluxes from mid-$10^{17}cm^{-3}$ to low-$10^{18}cm^{-3}$ were chosen. The actual electron concentration was measured using Van der Pauw method. The Hall measurement was done on square samples with a typical size of 0.5×0.5 cm^2. The In-Sn contacts were applied on the four corners and the samples were annealed at 400 $°C$ for 3 min in N_2 ambient. (1 T, -1T) magnetic field and 0.01-1 mA current were used during the Hall measurement at room temperature. The electron concentration results were

compared to separate measurements in thermoelectric devices using the same samples [43, 59]. The results are in agreement within 5% of systematic error. Because Si is a shallow donor in GaAs (5.8 meV below the conduction band minima), all Si donors should be activated at room temperature, and their amount should also represent the free electron concentration in GaAs. The doping efficiency is then the quotient of the actual free electron concentration measured in the GaNAs:Si samples divided by the predicted doping level. On the other hand, Monte Carlo simulation is based on a single monolayer during growth where initially randomly distributed N adatoms with thermally activated diffusivity perform random walk with isotropic direction preference. Although there is no direct data available for Si and N diffusivity on GaAs surface, N diffusivity is about 2-3 order of magnitude higher than that of Si in bulk GaAs [60, 61]. It is also suggested that the motion of Si on GaAs surface can be neglected [62]. Therefore, in the simulation, we assume Si adatoms are randomly distributed and static. Each N adatom resumes random walk until it either encounters a Si adatom on the surface to form a $(Si - N)_{As}$ defect complex or incorporates into the lattice after a particular displacement, i.e. diffusion length, is reached. The Si adatom density is set to be $1.0 \times 10^{18} cm^{-3}$, while the N adatom density varies for different computation scenarios. The computed doping efficiency is given by $1 - N_{comlex}/N_{Si}$, where $N_{complex}$ is the number of $(Si - N)_{As}$ defect complex formed and N_{Si} is the total Si adatom amount. The simulation traces the trajectories of 100,000 N adatoms on the growth surface for each run and averages over 10 ensembles or, in other words, 10 monolayers.

The simulated doping efficiency in GaN_xAs_{1-x} for x=0.5%, 1%, 2% and 3% is shown in figure 4.1. The general trend for each N composition is that the doping efficiency decreases as N adatom diffusion length increases (or substrate temperature increases, indicated by the top x-axis). Take x=0.5% for example, the doping efficiency starts from ~66% when the N adatom diffusion length is 0.5 nm and quickly decreases to < 4% when N diffusion length is 50 nm. This is expected because longer N diffusion length makes it more likely for N to encounter a Si atom on the surface. Another trend on the doping efficiency is that the higher the N content it, the faster the percentage decays, as it is expected that more populated

N species should have a higher probability of Si encounter statistically. Hence more $(Si - N)_{As}$ complexes, acting as electron traps, are formed during a random diffusion process and less Si, as donors, are counted in the final configuration. These two trends are elaborated more clearly in a semi-logarithmic plot (inset of figure 4.1). The doping efficiency decays exponentially as $P = a \ 10^{-L_N/L_{0.1}}$, where a is a constant, L_N is the N diffusion length and $L_{0.1}$ is the decay length for which diffusion displacement the N adatom random walk renders Si only 10% still active as donors. $L_{0.1}$ are 38 nm, 19 nm, 9.4 nm and 6.4 nm for x=0.5%, 1%, 2% and 3%, respectively. It indicates that when there are more N adatoms (larger x) available on the surface, it takes less diffusion length for N to disable Si as active dopants. And statistically, N adatoms shorten the decay length in a reciprocal manner, i.e. if $[N_1] = \alpha[N_2]$ then $L_{0.1}^{N_1} = L_{0.1}^{N_2}/\alpha$, which causes the doping efficiency to slump faster when N incorporation increases.

The experimental data hold a similar trend as the growth temperature goes from low ($460 \,^\circ C$) to high ($550 \,^\circ C$) (figure 4.2). Samples grown at high temperature (beyond $520 \,^\circ C$) turn out to be highly resistive while the doping efficiency peaks around $480 \,^\circ C$ and somewhat plateaus below that. A straightforward model to transform the simulated data from figure 4.1 to compare with the experimental data is to assume that the diffusion coefficient of N adatoms follows the Arrhenius rule so that the diffusion length can be given as $L = C \ exp(-E_a/2k_BT)$, where C is a fitting constant, E_a is the activation energy, k_B is the Boltzmann constant and T is the growth temperature in Kelvin. Although studies on N diffusion are reported in the literature [60, 63], direct information of N surface diffusion length on Ga(N)As is absent. An empirical fitting with fitting constant $C = 1 \times 10^{12} nm$ and $E_a = 3.6 \pm 0.1 eV$ can reasonably emulate the experimental data trend. Note that the experimental data points in figure 4.2 do not all have exactly the same N composition: from low temperature to high, x=0.51%, 0.54%, 0.57%, 0.61%, 0.79%, 1.1% and 1.2%, respectively (The increase in N composition comes from the over-increase on the N flow rate to compensate lower N incorporation efficiency at higher temperature). Figure 4.2 suggests that N adatoms with shorter diffusion length, originated from smaller atom hopping rate at lower temperature, are more
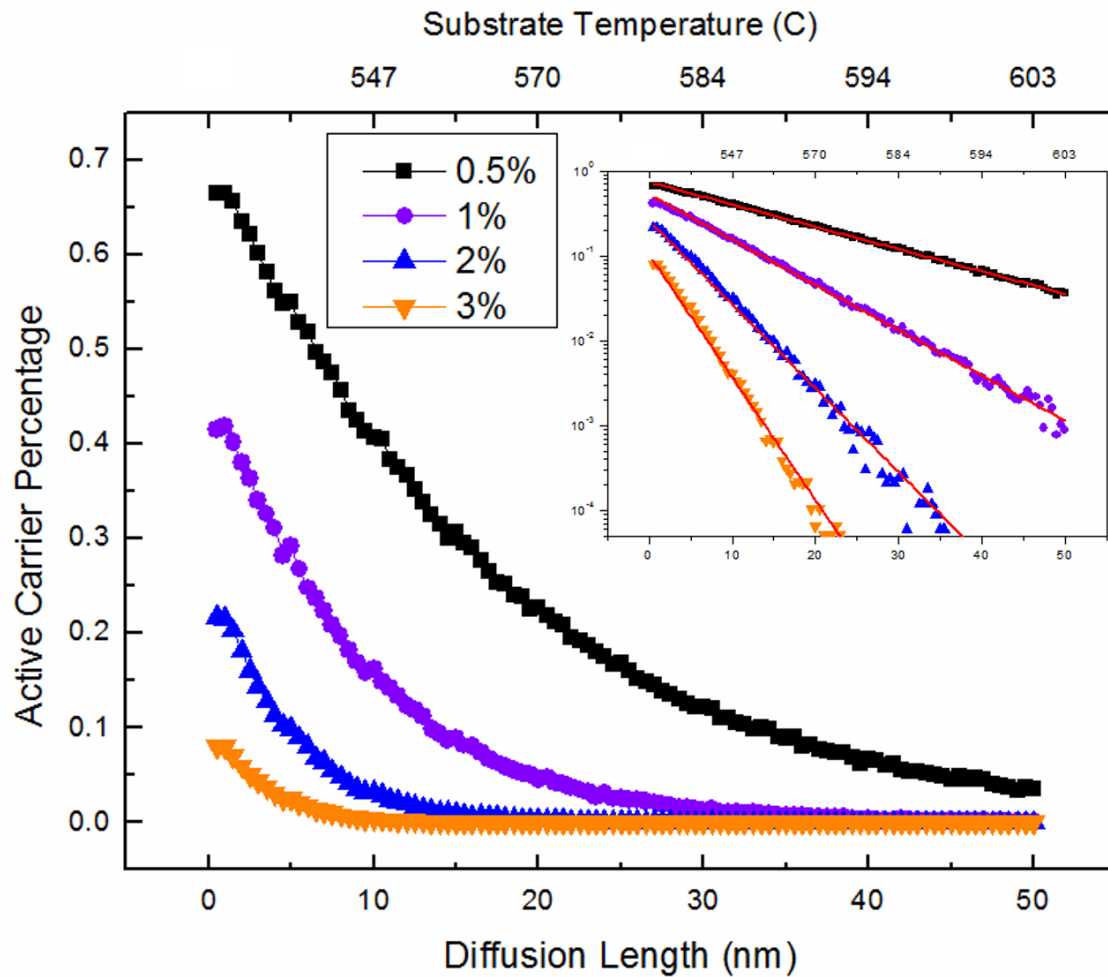
Figure 4.1: Monte Carlo simulation of the Si doping efficiency as a function of N diffusion length for various N contents (0.5%, 1%, 2% and 3%). The semi-log plot (inset) shows the linear fit and the different 10% decay length, $L_{0.1}$, 38 nm, 19 nm, 9.4 nm and 6.4 nm for different N contents in the same order mentioned. The corresponding substrate temperatures based on the diffusion model fitting are also displayed as the top x-axis.
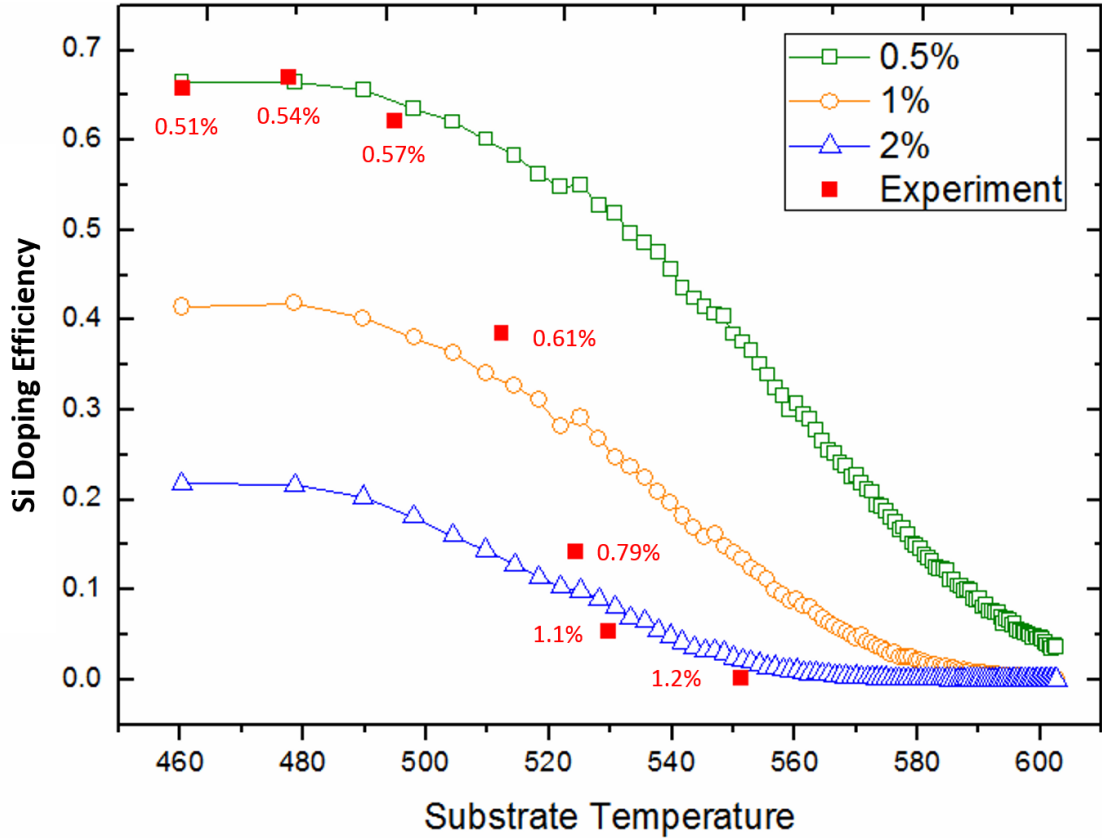
Figure 4.2: Monte Carlo simulation of the Si doping efficiency as a function of growth temperature for various N contents (0.5%, 1%, 2%). From low temperature to high, the N contents of the experimental data points are 0.51%, 0.54%, 0.57%, 0.61%, 0.79%, 1.1% and 1.2%, marked near the data points respectively.

likely to grant the Si adatom a higher survival rate — a higher possibility for Si to take the Ga sublattice position and not get in the vicinity of an active N atom and form Si-N bond. On the other hand, the higher substrate temperature drives N adatoms diffusion length longer that drastically kills the potential active donors on the surface. The large fitted parameter Ea may originate from the high hopping barrier for N adatom on GaAs surface due to its kick-out diffusion mechanism26 and local strain.

It is expected that Si doping efficiency in GaAs should increase as growth temperature decreases according to the law of mass action; however, the doping efficiency only decreases $< 7\%$ for the temperature range from 500 $°C$ to 560 $°C$ [52]. Hence it cannot account for the large difference in doping efficiency found

in this study. In addition, the V/III incorporation ratio was kept constant to minimize its influence on doping efficiency. The fact that a random work model is capable of reproducing such a declining trend on the doping efficiency suggests that it is governed by the Si-N encounter on the surface during growth. Reason et. al. reported that there is a "forbidden window for GaNAs growth starting from 520 °C [64]. Below the "forbidden window, layer-by-layer growth dominates because of short adatom diffusion length, leading to better surface morphology. Other ways to shorten N diffusion length, such as using Sb as a surfactant, to promote film surface morphology have also been reported. Both findings justify the diffusion model in the simulation that assumes no vertical diffusion in the lower temperature region. However, the discrepancy between simulation and experimental data for temperatures beyond 520 °C probably implies a mechanism more than lateral diffusion. When temperature is ramped up to inside the "forbidden window, it enters the multilayer growth mode that ends up with a much rougher surface [63, 64]. Therefore, it is reasonable to see the good agreement between Monte Carlo simulation and the experimental data below the "forbidden window when N adatom motion can be described by lateral diffusion, while the simulation cannot account for mechanisms, such as islands formed in multilayer growth mode [64] and higher density of available group-V lattice sites on a (2×4) surface reconstruction at higher substrate temperature (compared to (2×1) at lower) [53], that can facilitate the bond forming in $(Si - N)_{As}$ besides the longer diffusion length levitated by growth temperature. Therefore, the survival Si atoms in active dopant positions turn out to be smaller than what the diffusion model predicts. Yet the actual physical process in doping efficiency decrease, particularly at temperature >520 °C, is still open to debate. A high definition in-situ surface imaging technique that can resolve Si and N atoms can shed light on the actual microscopic process.

To further evaluate how change in N composition would affect the doping efficiency, we compare the Monte Carlo simulation results with the experimental results (samples grown at ~480 °C) for a range of [N] from 0 to slightly more than 3% (figure 4.3). Experimental data from Ref. [53] and Ref. [54] are also included for comparison. Starting from x=0, Si atoms are all activated as donor

as expected. Then any small amount of N added to the film drastically increases its encounter rate with Si during growth and propels the exponential decay of doping efficiency. The simulated curve captures this trend very well. This has several implications. First of all, it provides indirect proof that N passivates Si during surface diffusion, an assumption our Monte Carlo simulation starts with, and it is manifested by the severe decline in Si as active donors when more N are present. Secondly, it indicates once again that a random walk model that assumes only lateral N diffusion can well account for the major microscopic process on the surface during low temperature growth of GaNAs:Si. And finally but not least, besides the auto-compensation by the amphoteric nature of Si, Si doping efficiency is highly limited by $(Si-N)_{As}$ formation on the growth surface during epitaxy. While the auto-compensation can be exceeded by low temperature and high V/III ratio growth technique, it would be technically difficult to dope dilute nitrides by Si to highly n-type ($\geq 3 \times 10^{19} cm^{-3}$), demanded by dilute nitride based intermediate band solar cell, since the $(Si-N)_{As}$ has been shown to be the energetically favorable configuration [51]. Indeed, for 1% of N composition, the doping level has never exceeded mid-$10^{18} cm^{-3}$ in our GaNAs(P) growth even with the high doping techniques aforementioned (high V/III ratio and low growth temperature). It is predicted that the enhanced electron effective mass should increase the density of states and benefit applications such as thermoelectrics; nevertheless the benefit may totally be outweighed by the low doping efficiency of Si [43]. As Yu et. al. [49], Jin et. al. [53] and Janotti et. al. [51]suggest, group VI dopants are energetically unfavorable to form defect complex with N, and they are more practical to use when a high free electron concentration is desired.

Since the MBE machine used to grow the GaNAsP material is not equipped with group VI dopants, high doping level in the IB region is achieved with the prediction given by the Monte Carlo model.
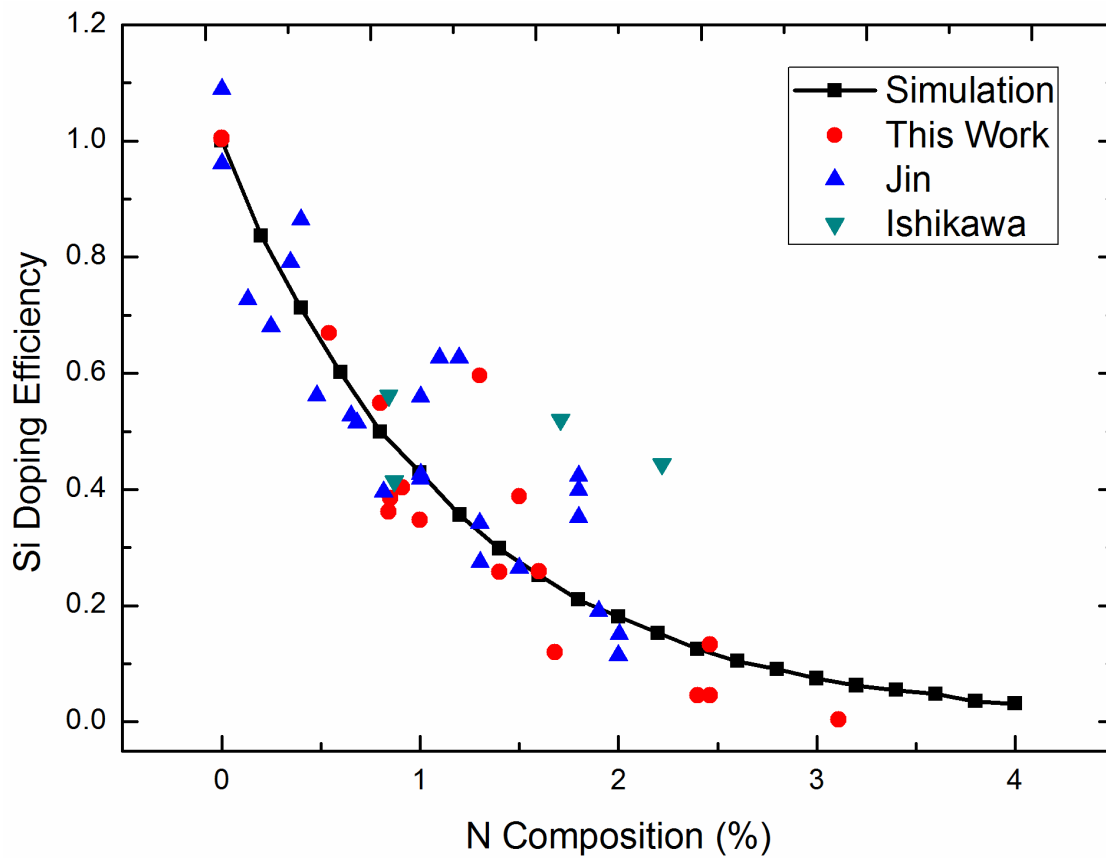
Figure 4.3: Comparison of Si doping efficiency between Monte Carlo simulation and experimental measurement on samples grown at $480°C$. Also included are data by Jin [53] and Ishikawa [54].

Table 4.1: Targeted material parameter in the GaNAsP IBSC device.

Materials	As	P	N	Affinity	Bandgap	Lattice Cons.
GaAsP (cap)	0.55	0.45		3.66 eV	1.98 eV	5.562 $\mathring{A}$
GaNAsP	0.61	0.378	0.012	4.11 eV	(1.51, 2.21) eV	5.563 $\mathring{A}$
AlAsP	0.5	0.5		3.74 eV	2.29 eV	5.562 $\mathring{A}$

4.4 Electron blocking

Based on the calculation in chapter 3 on theoretical efficiency, the following material parameters are targeted in the metamorphic cap layer and the device active layer (table 4.4). Also shown are the AlAsP material properties as a blocking layer. After grading the As composition to the GaAsP cap, the lattice constant is fixed in the subsequent layers to avoid misfit dislocations. Note that the electron affinity for GaNAsP is calculated by adding the bandgap shrinkage due to N incorporation to the electron affinity of GaAsP. Based on the parameters in table 4.4, the band diagrams for unblocked IB (UIB), blocked IB (BIB) by undoped GaAsP and BIB by undoped AlAsP are shown in figure 4.4.

In figure 4.4, a) shows the scenario when no electron blocking layer is inserted between the GaAsP cap and the IB region. An electron pathway is formed between the GaAsP cap and the IB layer and it facilitates electron tunneling. If an i-GaAsP layer or i-AlAsP layer is inserted in between, the electron pathway is cut off and the IB is then isolated. The difference between GaAsP and AlAsP is the effectiveness in electron blocking. AlGaAs was used in GaNAs IBSC because the conduction band offset in AlGaAs/GaAs is large. However, the conduction band offset in AlAsP/GaNAsP is 0.37 eV compared to 0.45 eV in GaAsP/GaNAsP, although AlAsP with 50% As has a bandgap of 2.29 eV. The reason is that the electron affinity in AlAsP is large and the bandgap difference is not dominated by the offset in conduction band (one can notice the large valence band offset in AlAsP/GaNAsP). In addition, inserting AlAsP between the GaAsP cap and the GaNAsP layer involves source changes during growth. It brings in complications in terms of lattice matching. Futhermore, if a Al-containing compound is not grown at the appropriate temperature (generally above $600°C$), it generates defects and the X-band below the Γ becomes a very good electron pathway. Therefore, growing
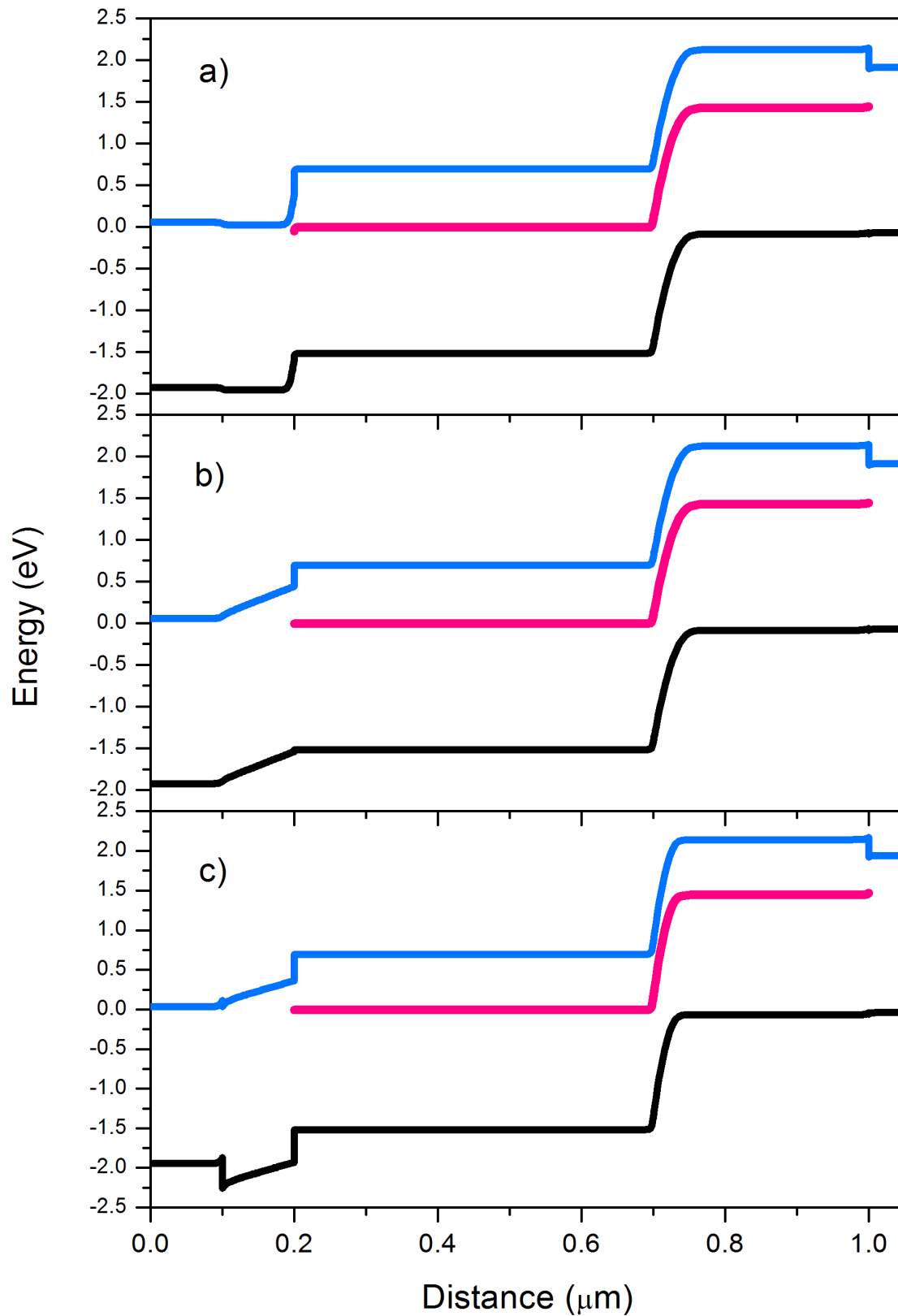
Figure 4.4: Band diagram of GaNAsP IBSC device. a) Unblocked IBSC. b) Blocked IBSC by i-GaAsP. c) Blocked IBSC by i-AlAsP.

Al-free GaNAsP IBSC by using i-GaAsP blocking layer is preferred.

4.5   Device growth, fabrication and performance

According to the 1st design guideline of IBSC, the IB region is doped to be degenerate. In the case of figure 4.4, the whole n-region is designed to be $10^{19}cm^{-3}$. To achieve a high quality metamorphic buffer and degenerate doping in the IB region, growth temperature was changed after the GaAsP cap layer. A 550 $^\circ C$ was used to grow the linearly graded buffer and the GaAsP relaxation cap layer to grow the template for the subsequent p-n junction. Then the substrate temperature was lowered to 400 $^\circ C$ to grow the N containing layers. The reason for lowering substrate temperature is mainly to exceed the doping limit set by autocompensation of the amphoteric dopant, Si, besides the consideration of the passivation of Si dopant by N during growth described in the previous section. Consider the following exchange reaction on the surface,

$$Si_{Ga} + V_{As} \leftrightarrow Si_{As} + V_{Ga}, \tag{4.1}$$
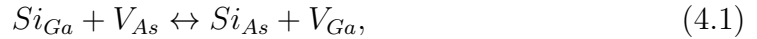
where Si_{Ga} and Si_{As} represent Si on a Ga site as a donor and As site as an acceptor, respectively. The autocompensation is set by the ratio of Si-acceptor concentration to Si-donor concentration, i.e. $[Si_{As}]/[Si_{Ga}]$. The law of mass action gives,

$$\frac{[Si_{As}][V_{Ga}]}{[Si_{Ga}][V_{As}]} = c \ \exp(-\frac{\Delta E}{k_B T}). \tag{4.2}$$

where ΔE is the activation energy. $[V_{Ga}]$ can be considered roughly as constant in the temperature involved, but $[V_{As}]$ increases exponentially with temperature. Therefore, decreasing the growth temperature will bring down not only the probability of Si-N passivation but also the autocompensation ratio. Furthermore, to decrease the As vacancy density on the surface, very high V/III ratio was used during the dilute layer growth. The growth rate of Ga was lowered to 0.5 ML/s to achieve high V/III ratio while maintaining the high vacuum. Samples of GaAsP were grown at 400 $^\circ C$ to find out the lattice matching condition between the GaAsP cap layer and the N containing layers.

Generally speaking, the longer the IB region is, the stronger the absorption is, hence higher current density of the device. However, if the degenerate high doping is put in the vicinity of the junction, it acts like a tunnel junction when reverse bias is applied. Since the tunneling probability is inversely proportional to the product of bandgap and depletion width, the reverse breakdown voltage is extremely small and the whole I-V curve looks symmetric (figure 4.5). Another drawback on the SC performance with a degenerate doping in the whole n-region is that the depletion region becomes extremely small. In dilute nitride material, the diffusion length of electrons as minority carriers suffers from the strong scattering from N and so far has not exceeded 0.5 μm. The photo-generated electrons are mostly collected in the fields aided manner instead of diffusion. If the depletion region is too short in p-n junction, most of the electrons cannot survive the high defect and trap density throughout the dilute nitride IB region. Therefore, the one for all doping profile in the IB n-region has to be replaced.

A straightforward amendment on the design of figure 4.4 is to break up the n-type IB region into two parts: a degenerate doping region farther from the junction and a lighter doping closer to the junction (figure 4.6 and figure 4.7). Another improvement on the device is to reduce the defect and trap density. RTA has been proven to be effective in terms of improving PL in chapter 3. However, the mutual passivation effect will sacrifice the active electron doping in the degenerate IB region. The diode I-V measurement on device structure in figure 4.7 b) after a series of RTA temperatures is shown in figure 4.8. The reverse breakdown voltage is significantly improved and the symmetric feature on figure 4.5 disappear. It is of significance to notice the change on the current density by different RTA temperatures. In the forward bias region, 700 $°C$ stands out with the highest current density followed by 750 $°C$. Both 800 $°C$ and 850 $°C$ turn out to have smaller current density than the as grown sample. This means RTA at 700 $°C$ and 750 $°C$ helps to improve the device material quality but at an RTA temperature between 750 $°C$ and 800 $°C$ the mutual passivation effect kicks in and increases the resistance in the device. Such a threshold temperature is in agreement with Yu et. al.'s first report on mutual passivation. Interestingly, however, the dark current
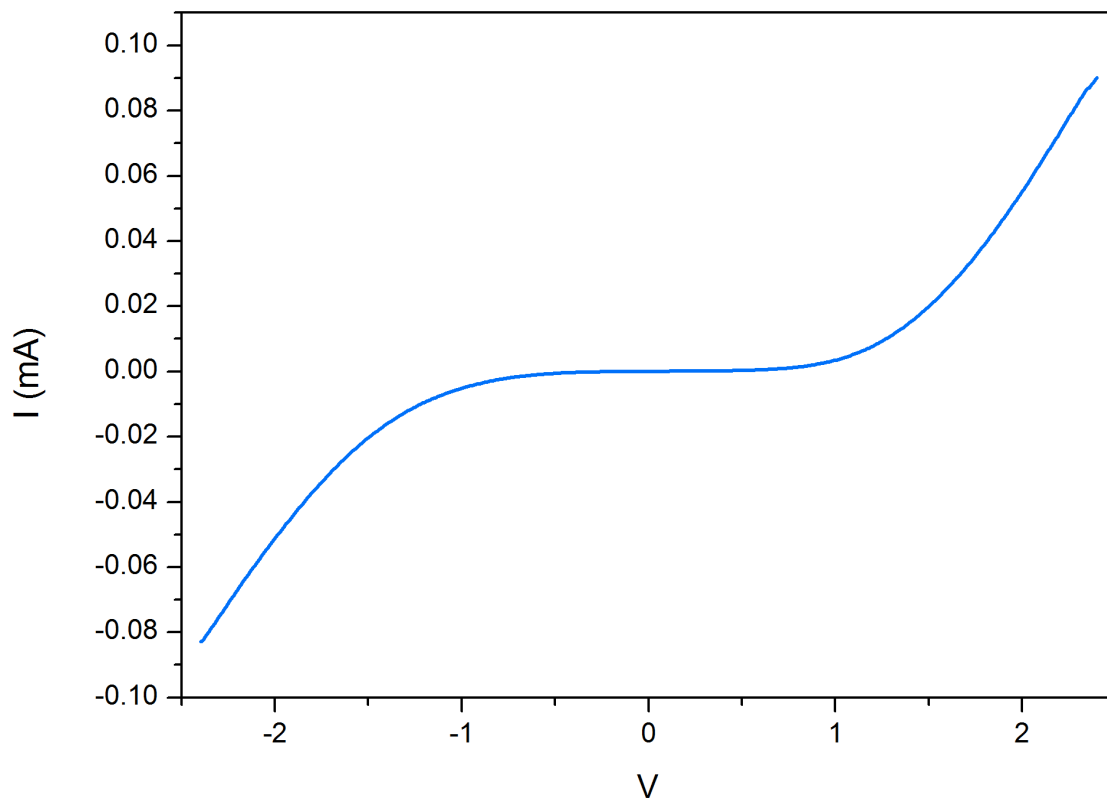
Figure 4.5: Current-voltage measurement in darkness on a IBSC with device structure in figure 4.4 b.
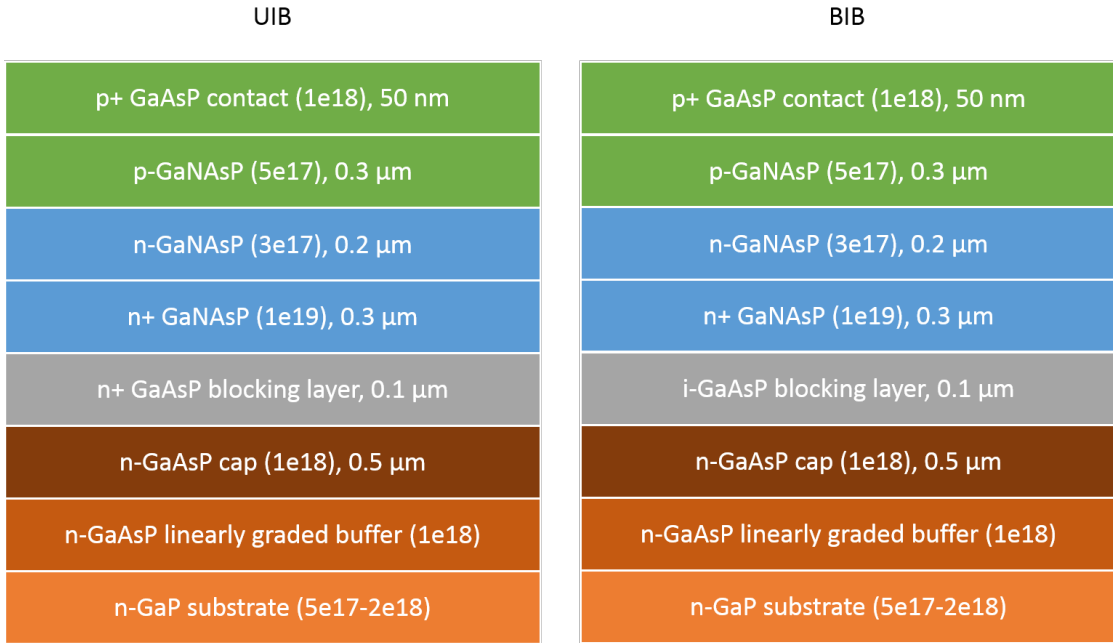
Figure 4.6: Schematic of GaNAsP IBSC device material structure. Drawings are not to the scale.

keeps on decreasing as RTA temperature increases. The dark current is a good indicator of defect or recombination trap density in the junction. In chapter 3, the optimization study on RTA temperature shows the best temperature to anneal a GaNAsP sample is around 950 $°C$. A smaller dark current would be expected should the RTA temperature increase further that steps into the mutual passivation zone. This is a trade-off between defect density and the active Si density. Based on the results from figure 4.8, the optimal temperature for RTA on a GaNAsP IBSC device should be around 750-800 $°C$.

Both metal contacts and liquid contacts were used to fabricate the IBSC device. $100/2000Å$ Ti/Au contacts were deposited trough a finger grid shadow mask as front metal contacts by e-beam evaporator on the p-side surface of the device. In was used to make the back side n-type contact. For liquid contact, the substrate with In as ohmic contact was attached to a coiled, tin-plated Cu wire using conductive Ag paint, and epoxy (Hysol 9460F) was used to seal, face-down, the assembly at the end of a segment of glass tubing. The active area of each electrode was determined by the epoxy, with a typical value of 0.1-0.2 cm^2.
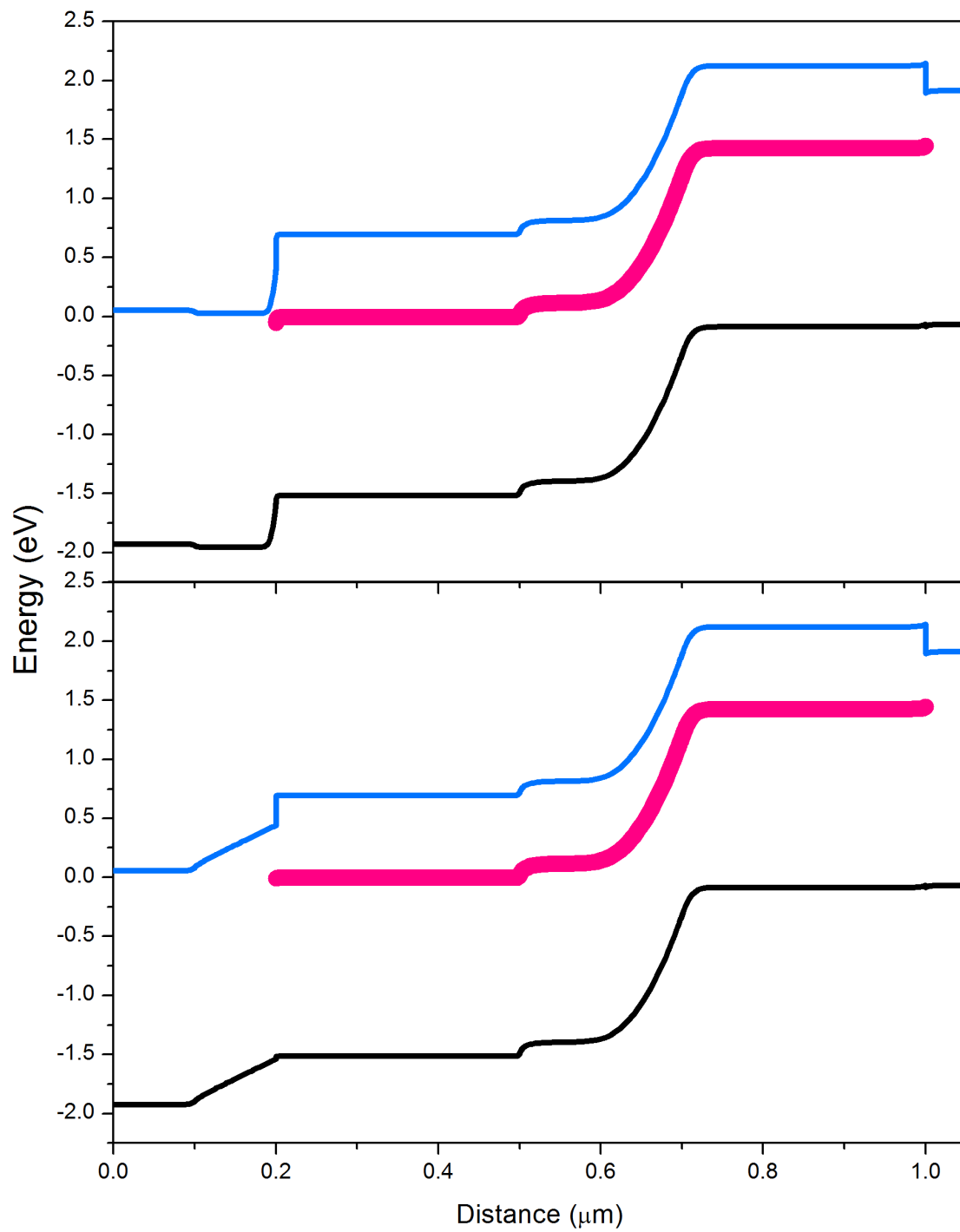
Figure 4.7: Band diagram of GaNAsP IBSC UIB and BIB structures with lighter n-doping near the junction interface.
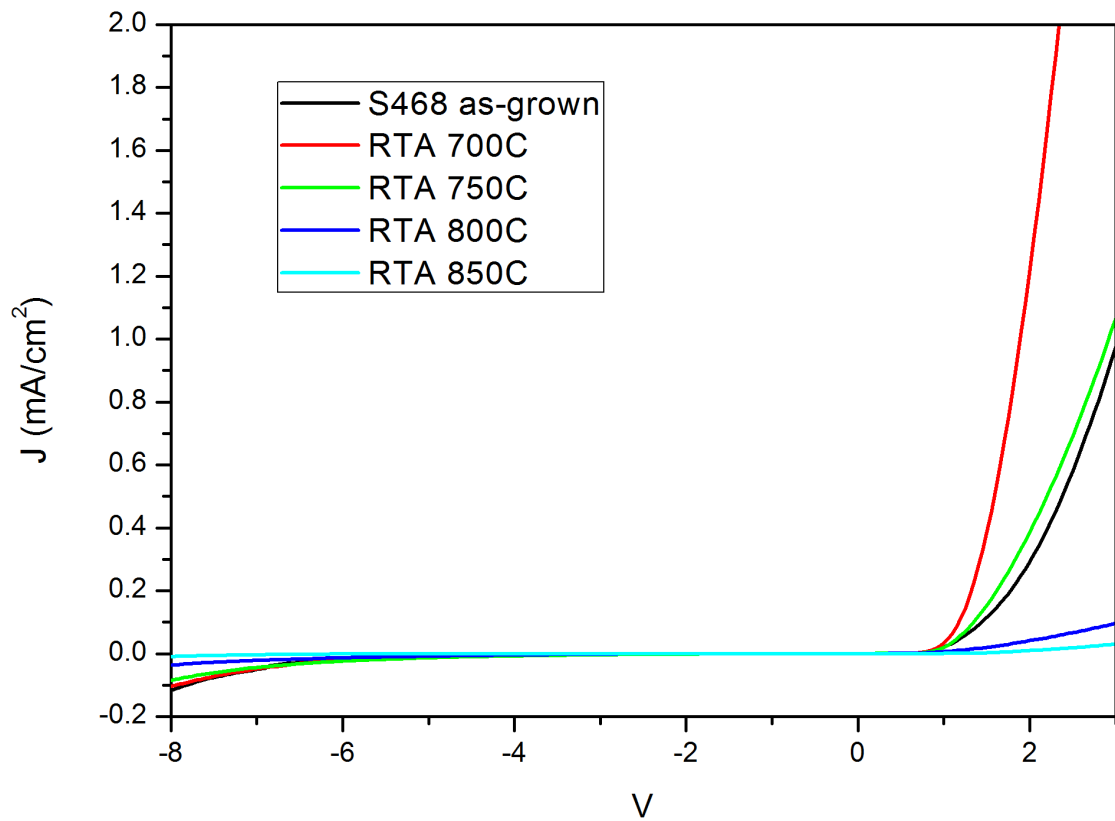
Figure 4.8: Band diagram of GaNAsP IBSC UIB and BIB structures with lighter n-doping near the junction interface.

Electrodes were left at room temperature to dry overnight. Prior to loading into the golvebox for photoelectrochemical measurement, the photoelectrodes were etched in a solution of 0.04% (v/v) Br_2 in methanol (CH_3OH, low water, J. T. Baker) for 15 s, followed by immersion in 1.0 M KOH(aq) for 30 s. Then the electrode was thoroughly rinsed with water and CH_3OH, then dried in a flow of $N_2(g)$ and quickly transferred into a glovebox that was continually purged with ultra-high purity argon. The non-aqueous photoelectrochemical method was employed to investigate the optoelectronic properties of the IBSC. A highly doped GaAsP with a carrier concentration of $1 \times 10^{18} cm^{-3}$ was in contact with the fast one-electron redox couple ($FeCp^{2+/0}$) forming an ohmic contact. Photogenerated holes diffuse or drift to the p+-GaAsP/liquid interface and oxidize the reduced species $FeCp_2^0$ to $FeCP_2^+$ and contributing to the photocurrents. The Pt reference electrode was poised at the solution potential and the Pt counter electrode regenerate the $FeCp_2^0$ species by reducing the oxidized $FeCP_2^+$. The kinetically facile, one electron, reversible $FeCP_2^{+/0}$ redox couple was chosen to ensure that the electron-transfer kinetics at the semiconductor/liquid interface were not rate-limiting, so that only the energy conversion properties of the IBSC were measured. A direct comparison between metal contacts and liquid contacts shows liquid contacts have a better performance on the device (higher photo-current). All the following discussion on the device performance will be based on measurement by liquid contacts. Figure 4.9 shows the I-V measurement on IBSCs with structure shown in figure 4.7. First of all, RTA helps to improve current density in both UIB and BIB structure by removing defects in the dilute nitride IB region. In particular, the J_{SC} of both UIB and BIB are improved to two-fold by RTA. Secondly the J_{SC} of BIB is smaller than UIB. Thirdly, the V_{OC} in UIB and BIB are similar, i.e. around 0.6 V. In other words, the electron blocking in BIB is not effective. It is easy to notice that the shunt resistance in both BIB and UIB devices are similar but the serial resistance in BIB is higher. This might lead to a smaller short circuit current in the BIB device. Another point to be worth noticing is that after RTA, the V_{OC} is slightly increased in both BIB and UIB. All these findings point the origin of the inferior performance of the BIB device to defects, particularly defects generated in the IB
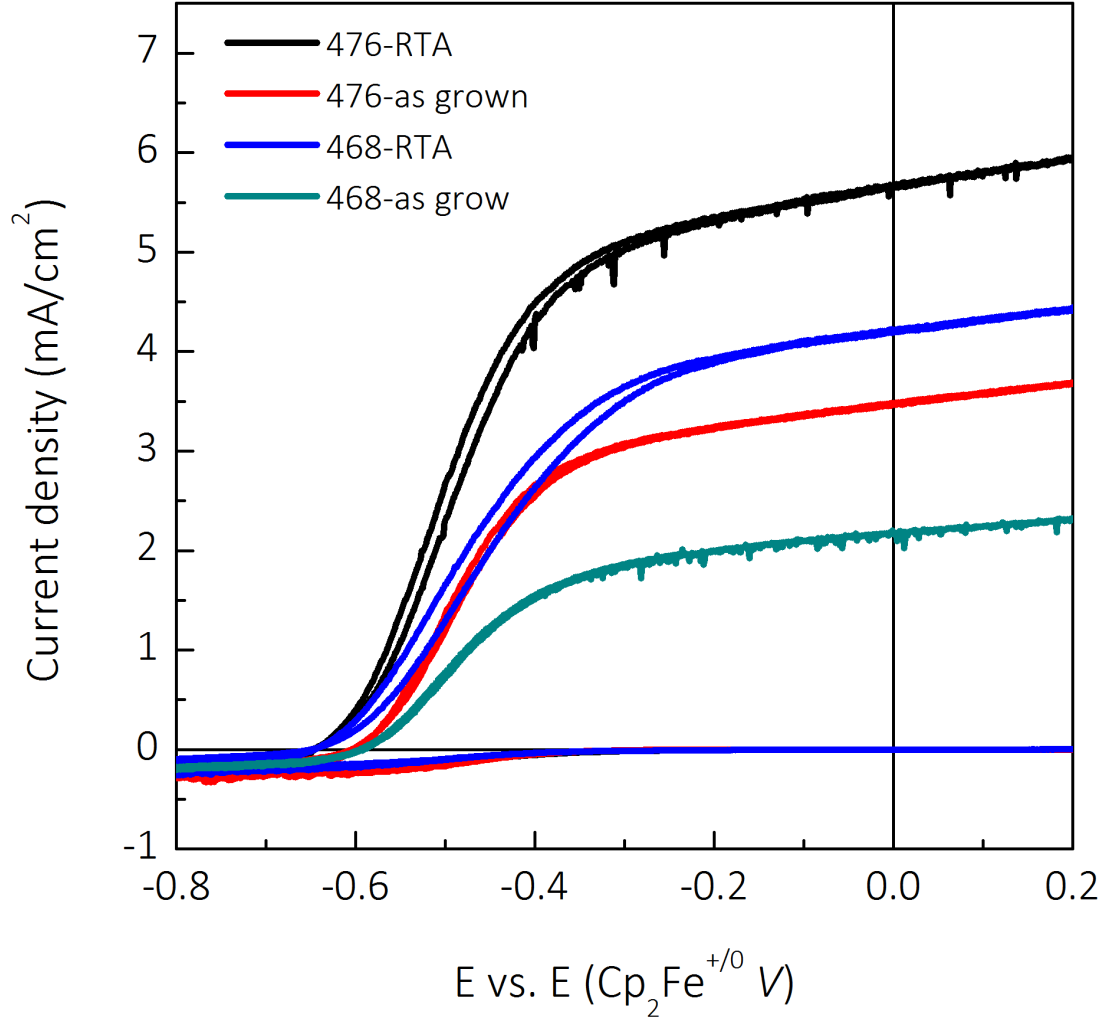
Figure 4.9: Current voltage measurement on IBSC device with structure design shown in figure 4.7.

region, junction interface and interface between N-free and N-containing layers. These interfaces underwent changes in type of sources and growth rate and it is likely misfit dislocation and were generated across theses interfaces. In particular, these misfit dislocations can serve as good electron pathways and recombination traps in the i-GaAsP blocking layer. That makes the i-GaAsP electron blocker not effective and renders the same V_{OC} for both UIB and BIB.

In addition to the complications due to growth temperature change across interfaces, there are a few disadvantages for the structure designs. According to the previous discussion, the IB characteristic shows only when the IB is half-

occupied so the IB is doped to be degenerate. This brings the attention to the IB in p-region of the p-n junction. In this region, the IB is rarely populated with electrons and it does not function as an IB. But forming an IB in this region requires N incorporation, which generates defects. Electrons as minority carriers in this region are subjected to defects scattering as well as strong induction of recombination. Another inferior properties the N brings in is the the band offset between the p-GaNAsP layer and the p+ GaAsP contact layer. Ideally, a window layer with positive conduction band offset should be placed between the p-GaNAsP layer and the contacts to avoid significant loss by surface recombination. The band alignment in figure 4.7, on the contrary, facilitate surface recombination due the negative band offset in the conduction band (in the growth direction).

The evaluation leads to refinement on the device structure design. Two sets of structures are proposed as follow. The first proposal is to remove the dilute nitride in the p-type region of the p-n junction and reduce the doping in the n-region closer to the junction (figure 4.10 and figure 4.11). A clear improvement on the band offset is seen near the surface. The surface recombination is expected to reduce in such a band setup. The reduction on n-type doping near the junction is to completely deplete this region and further partially deplete the degenerate IB region (although the depletion width within the degenerate IB region would be small). This is expected to enhance the photo-generated carriers collection by field aided mode. The second proposal is to remove the dilute nitride even in the lightly doped n-region. The IB characteristic absorption will not happen due to the $2 \times 10^{16} cm^{-3}$ doping so the N in this region is redundant. Having a dilute nitride material in the depletion region will increase the recombination center density. The doping in the lightly doped n-region is the same as in proposal one (figure 4.12 and figure 4.13). For discussion convenience, these device structures are referred to as structure 1 UIB and BIB and structure 2 UIB and BIB in the following discussion. For better IB isolation, the electron blocking layer increases to 200 nm for both structure 1 and 2. The growth recipes on structure 1 and 2 were also changed due to the difficulty of lattice matching across layer interface. After a 200 nm GaP buffer layer was grown, the whole subsequent layers of the device structures were

UIB	BIB
p+ GaAsP contact (1e18), 50 nm	p+ GaAsP contact (1e18), 50 nm
p-GaAsP (1e17), 0.3 µm	p-GaAsP (1e17), 0.3 µm
n-GaNAsP (2e16), 0.2 µm	n-GaNAsP (2e16), 0.2 µm
n+ GaNAsP (1e19), 0.3 µm	n+ GaNAsP (1e19), 0.3 µm
n+ GaAsP blocking layer (3e18), 0.2 µm	i-GaAsP blocking layer, 0.2 µm
n-GaAsP cap (1e18), 0.5 µm	n-GaAsP cap (1e18), 0.5 µm
n-GaAsP linearly graded buffer (1e18)	n-GaAsP linearly graded buffer (1e18)
n-GaP substrate (5e17-2e18)	n-GaP substrate (5e17-2e18)

Figure 4.10: Schematic of GaNAsP IBSC device material structure 1 (UIB and BIB). The p-region of p-n junction is N-free. Drawings are not to the scale.

grown at 460 $°C$.

RTA at 750 $°C$ were done on all these devices before their electrical properties were measured by the liquid contact method. There a few interesting findings on the I-V measurement. 1. The UIB and BIB of structure 1 do not show difference in V_{OC}. 2. In structure 1, BIB has higher J_{SC} than UIB. 3. In structure 2, BIB clearly sets itself apart from UIB with both higher J_{SC} and V_{OC}. 4. Structure 2 devices have larger shunt resistance than structure 1 (6.04 vs 4.74 Ωcm^2).

Many research studies on dilute nitrides suggest that the N incorporation introduce defects. These defects are found to be anti-sites and interstitials. Some of these N-relates states have an exponential distribution below E_-. Some of the deep states are plagued by inducing non-radiative recombination, a Shockley-Read-Hall process. Some of these states can be removed effectively by RTA at an optimal temperature. But since there is a restriction by mutual passivation, it is believed some of these N-relates states were not completely removed in these devices. The SRH recombination rate is given as follow,
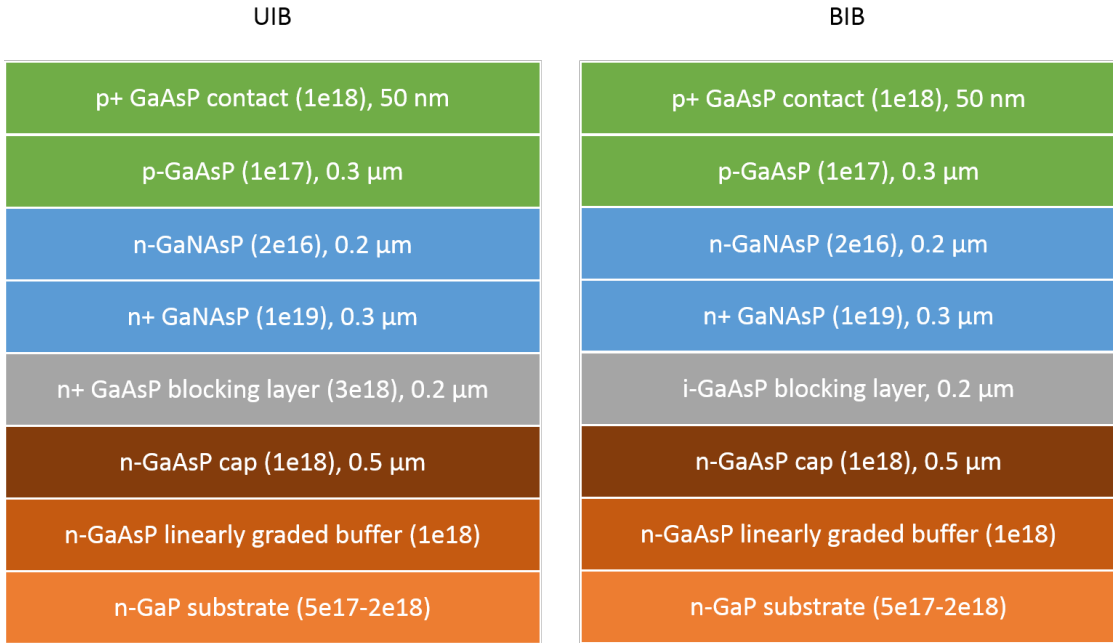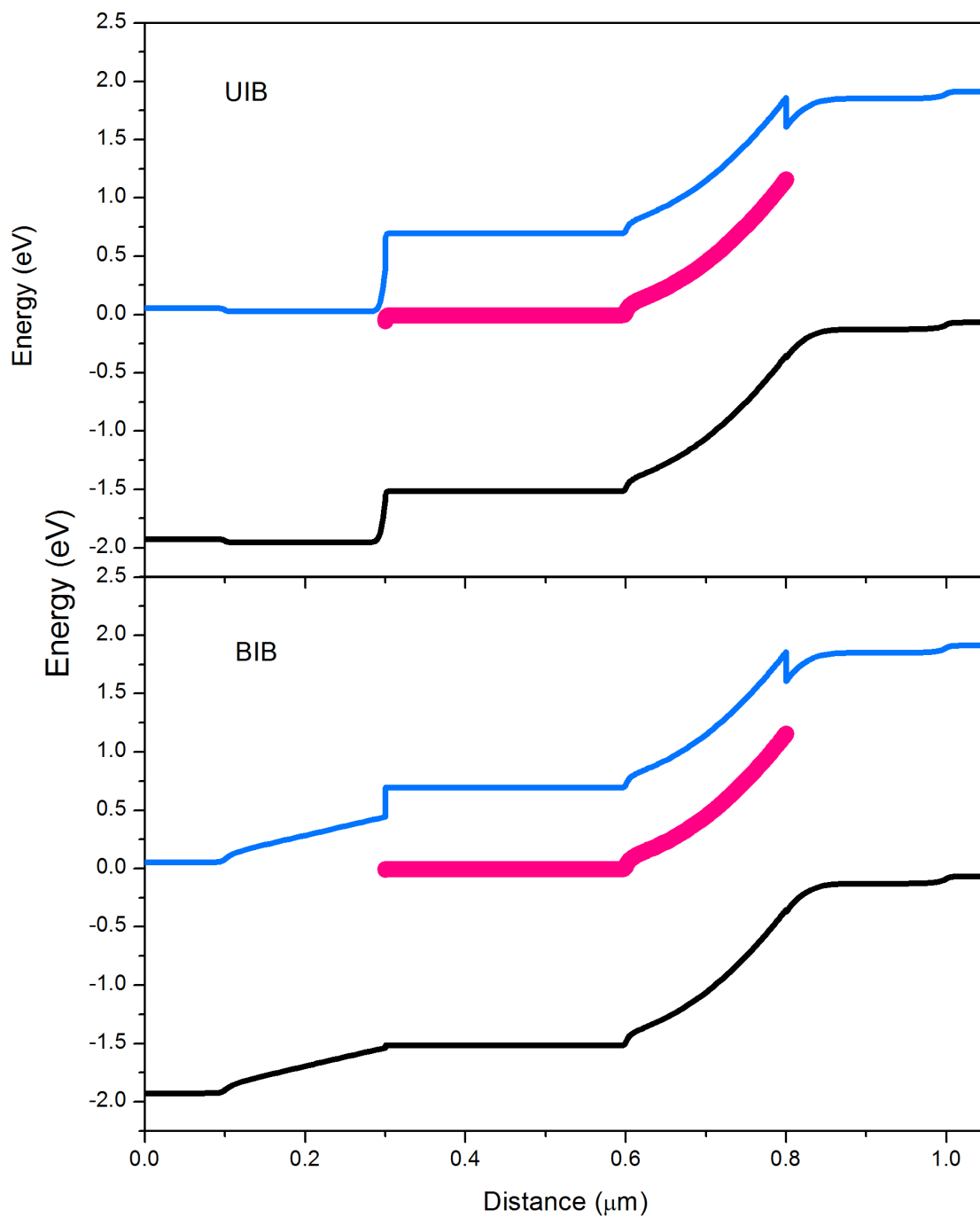
Figure 4.11: Band diagram of the device structure shown in figure 4.10.
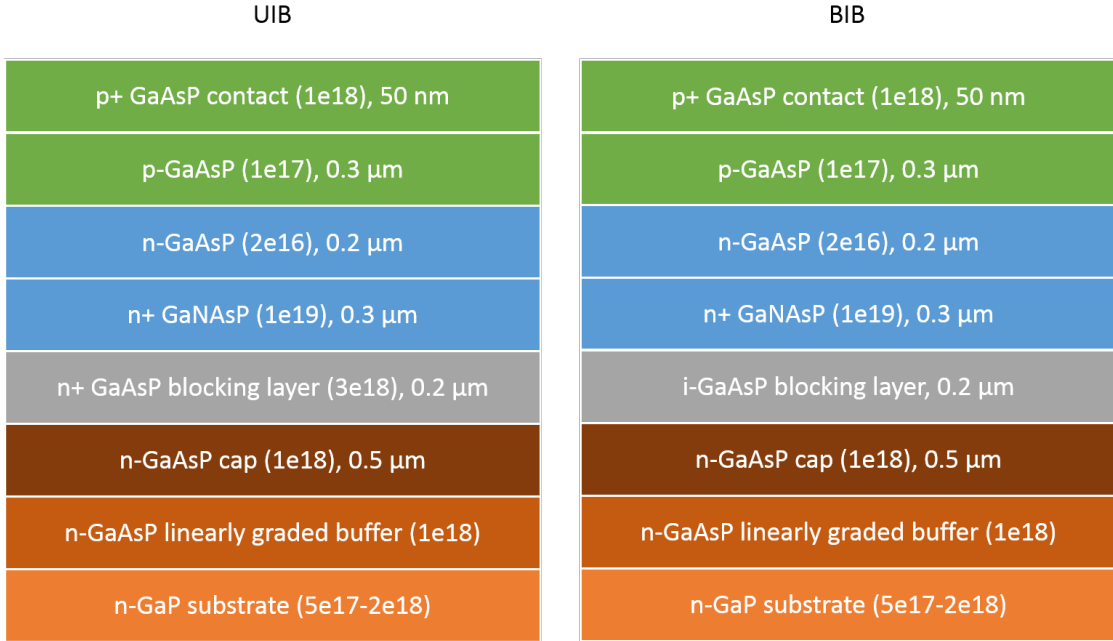
Figure 4.12: Schematic of GaNAsP IBSC device material structure 2 (UIB and BIB). The p-region of p-n junction and the lightly doped n-region are N-free. Drawings are not to the scale.

$$U_{SRH} = \frac{np - n_i^2}{\tau_{n,SRH}(p + p_t) + \tau_{p,SRH}(n + n_t)}, \qquad (4.3)$$

where $\tau_{x,SRH} = 1/v_x\sigma_x$ is the lifetime of a carrier captured by the trap. v_x and σ_x are the mean thermal velocity of a carrier and the capture cross section. n_t and p_t are the value of the electron and hole densities when their Fermi levels are equal to the trap level, respectively. According the expression above, the SRH recombination rate is highest in the depletion region because electrons and holes are similar in quantity and their densities are high due to the strong absorption in that region. Since the only difference between structure 1 and structure 2 is whether the lightly doped n-region has N, higher SRH recombination rate is expected in structure 1. A side proof is that higher shunt resistance in structure 2 than 1 indicates the filed aided carrier collection process dominate in structure 1 more than structure 2 (because as the bias goes more forward from zero bias the depletion region shrinks hence smaller current). So the carrier diffusion length is expected to be smaller in structure 1 than in 2. Even the J_{SC} are higher in
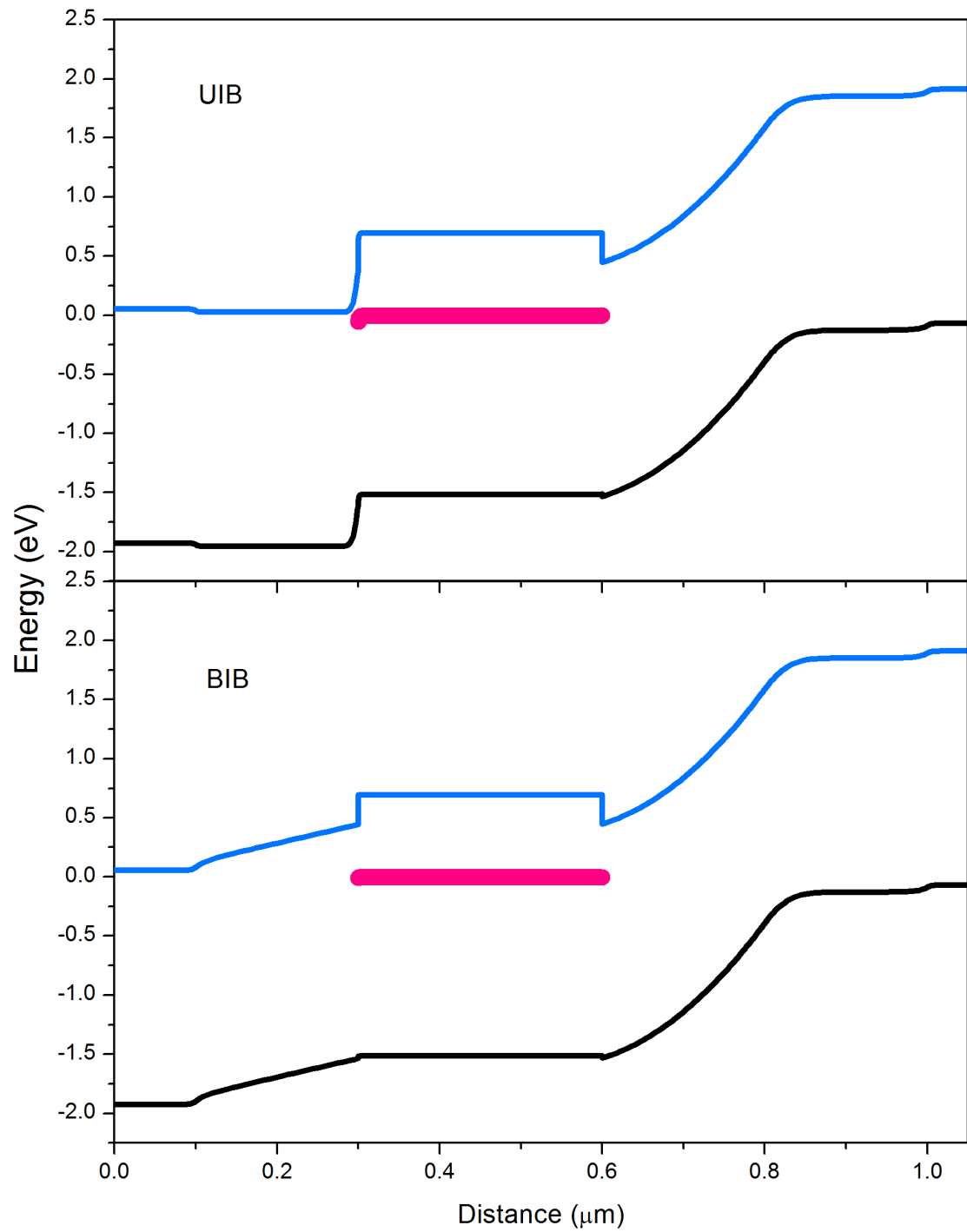
Figure 4.13: Band diagram of the device structure shown in figure 4.12.

Table 4.2: Solar cell performance of structure 1 and structure 2.

Device	$V_{OC}(V)$	$J_{SC}(mA/cm^2)$	FF	Efficiency (%)
Stuc 1 UIB	1.02	5.50	0.56	3.17
Stuc 1 BIB	1.02	5.87	0.59	3.51
Stuc 2 UIB	1.10	2.97	0.61	1.99
Stuc 2 BIB	1.20	3.46	0.66	2.73

structure 1, the inferior material quality in structure 1 gives them a larger dark current and hence a smaller V_{OC} than structure 2. The open circuit voltage is usually given by $V_{OC} = E_G/q - \Delta$, where Δ is an offset determined by the material and junction quality. It is likely that the higher N-related defect and trap density in the lightly doped n-region in structure 1 brings in a bigger offset to structure 1. And due to these defect and traps in the junction area, the electron blocking is not very effective so no difference is seen between UIB and BIB in structure 1. In structure 2, however, the junction depletion region area is almost N-free so the SRH is effectively suppressed. A higher V_{OC} is clearly seen in BIB than in UIB. A higher J_{SC} is also seen due to the extra absorption from the transition IB to conduction band. The smaller J_{SC} in structure 2 than in structure 1 is believed to be attributed to the thinner N-containing layers. All the GaAsP layers in the devices have As compositions around the $X - \Gamma$ crossover point. In the N-containing layer however, not only the As composition is higher due to strain balancing but also the N incorporation changes the band structure and increases the absorption. The smaller J_{SC} in structure 2 with thinner containing layer actually indicates the majority of the absorption happens in the IB area.

Table 4.5 lists the performance parameters (V_{OC}, J_{SC}, fill factor and efficiency under AM1.5) of the four devices. The $V_{OC}(V)$ achieved in structure 2 BIB (1.2 V) is the highest open circuit voltage compared to what have been reported in the literature so far. Even ZnTe has a higher bandgap of 2.25 eV, IBSC based on ZnTe:O have never been reported to have a V_{OC} higher than 0.38 V [65, 66]. Compared to GaNAs (2 eV bandgap with 0.92 V under 20 sun) [22], the V_{OC} offset in GaNAsP (1 V) is slightly less. Considering the GaNAsP devices were grown through a metamorphic structure, these results are significant. Figure 4.15
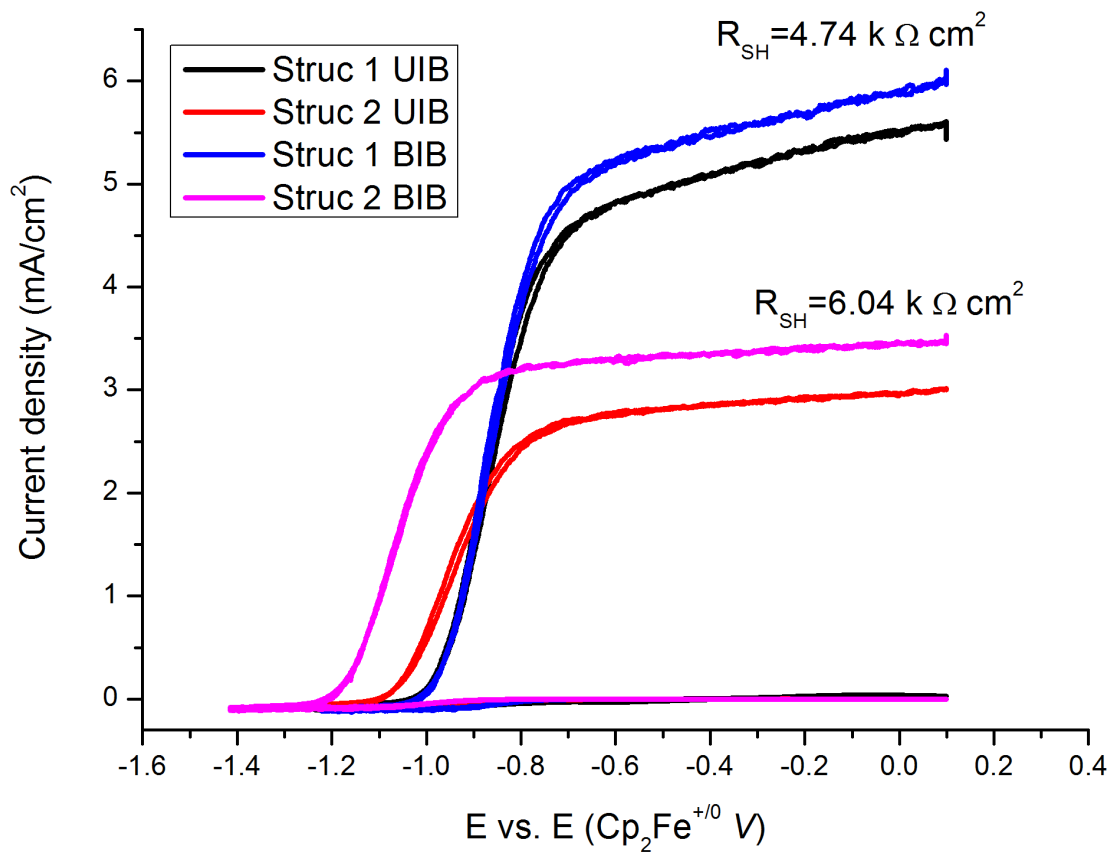
Figure 4.14: Current density vs voltage of structure 1 UIB and BIB and structure 2 UIB and BIB.
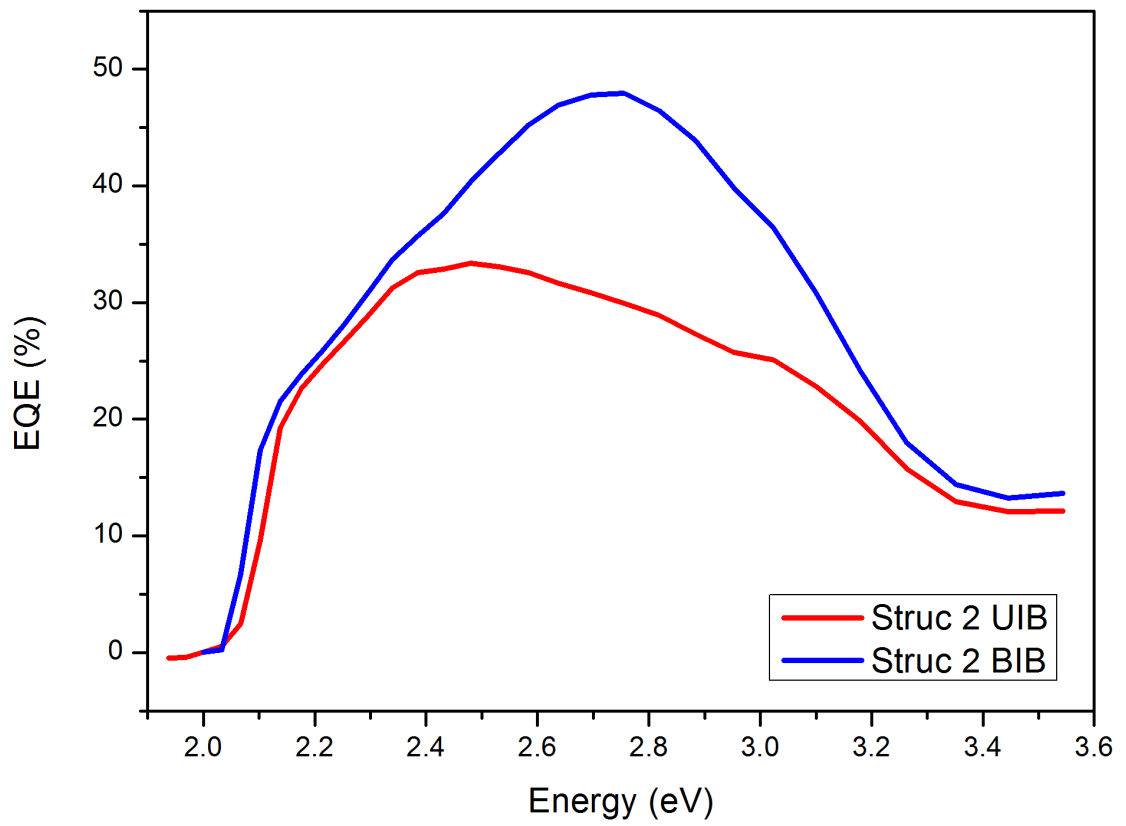
Figure 4.15: The external quantum efficiency of structure 2 UIB and BIB.

shows the external quantum efficiency of structure 2 UIB and BIB. There are a few thresholds in the EQE curve that correspond to different transitions. Due to long distance from the surface to the IB region, the threshold around 1.6 eV is too weak to see under AM1.5 condition. However, after the EQE takes off around 2 eV, the BIB structure clearly demonstrates the gain from the IB isolation. The EQE of BIB unambiguously deviates from that of UIB starting from around 2.2 eV, which is the E_+ energy relative to the valence band. The extra yield on EQE from the valence band to E_+ transition agrees with the higher V_{OC} and J_{SC} measurement seen in their I-V curve. Although the the power conversion efficiency for both structure 1 and 2 are still low ($< 4\%$), the well preserved V_{OC} opens up a broad opportunity and a bright future for GaNAsP IBSC since there is still plenty of room for device improvement.

4.6   Conclusion

Through a device structure design iteration, it is found that the best IBSC design on GaNAsP is to follow the BIB structure shown in figure 4.13. The removal of N in the p-region of the junction and in the lightly doped n-region significantly improves the material quality and device performance. With the structure 2 BIB device design shown in 4.13, a high V_{OC} (1.2 V) and fill factor (0.66) have been achieved. These numbers are the highest so far among all HMA IBSC reported in the literature.

5 Suggestions on future work

The best way to predict your future is to create it.

—Abraham Lincoln

The iteration on intermediate band solar cell (IBSC) structure design in chapter 4 has come down to a few critical points: 1) The n-region of the junction has to be broken down into two sections, a degenerate doping region and a lightly doped region. 2) No dilute nitride is needed in the p-region of the junction. 3) No dilute nitride is needed in the lightly doped n-region. These findings are very important aspects for GaNAsP based IBSC device. Given the superior open circuit voltage and fill factor of the structure 2 BIB IBSC, there is still plenty of room to improve device performance.

First of all, the IB region can be increased further to have better absorption. The structure 2 BIB design has an IB region only of 300 nm. According to the study on GaNAsP absorption coefficient, it is suggested that a 1 μm-thick absorber be used in the IBSC device. The argument does not take into account of the short diffusion length of electrons in dilute nitrides. The longest electron diffusion length in GaInNas is around 0.5 μm, and GaNAsP is expected to have a similar value. If a 1 μm-thick IB region is grown in the IBSC, electrons generated near the junction may not make it to the quasi neutral region, since no internal electric field is present in the majority area of the IB. A 0.5 μm-thick IB region should be the limit before a decay of excess electron density is seen.

Secondly, the Si doping efficiency is greatly limited at the presence of N. Due to the small amount N involved, a variation on N composition between each growth run will make the doping level in the IB region somewhat unpredictable.

Te is preferred as an n-type dopant in dilute nitride based IBSC. It can dope the IB region to a real degenerate level without complications. Furthermore, because the RTA temperature is limited by the mutual passivation between Si and N, RTA cannot be done at the optimal temperature if Si is used as a n-type dopant in a GaNAsP IBSC device. Te doped dilute nitrides are not subjected to such a limitation. A RTA temperature higher than 800 $°C$ can be done on a Te doped GaNASP IBSC.

Thirdly, if everything on the junction were to significantly improved, the obstacle for GaNAsP to find its path to commercialization or daily life application would be its metamorphic virtual substrate cost. Currently, about a 2-μm-thick graded buffer plus 0.5-μm-thick cap layer is grown to build such a virtual substrate with controlled defect density for devices. Such an epitaxial process costs time and money. If the metamorphic buffer can be thinned and if the whole IBSC can be grown from low-cost Si substrate, GaNAsP will definitely be a great candidate as an economic IBSC. Can these two be done? The answer is yes! Besides their interesting optical properties, dilute nitrides have intriguing structural properties as well. Due to the stronger bond from N, it has been found that they can slow strained film relaxation and effectively block threading dislocation [67, 68]. Our recent study on GaNAsP as a dislocation blocker shows that the graded layer could be thinned to less than 1 μm to have a virtual substrate with threading dislocation density less than the detection limit. The cap layer on top has very good crystal quality (figure 5.1). On the other hand, incorporating 2% of N into GaP can lattice match the alloy to Si. Good quality GaP on silicon templates have also been used for GaAsP solar cell study [69]. Combining the two promising techniques above, lowering the cost of manufacturing GaNAsP IBSC is indeed possible and should be around the horizon.
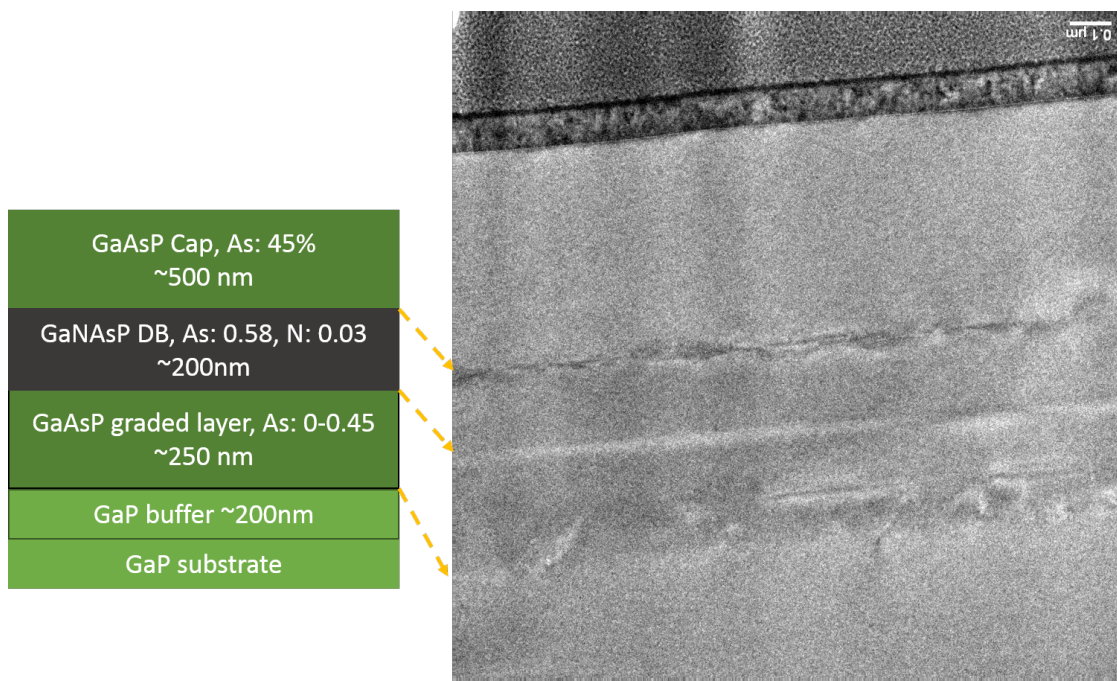
Figure 5.1: Transmission electron microscopy image of a GaAsP graded structure with GaNAsP as dislocation blocking layer.

Appendix

Growth and photoluminescence of GaP/GaNP core/shell nanowires

Recent development in the synthesis of one-dimensional (1D) semiconductor nanowire (NW) heterostructures has raised considerable interests for their potential applications as building blocks for nano-photonic and nano-electronic devices [70, 71, 72]. Radial core/shell or core/multishell heterostructures, formed by the growth of crystalline overlayers on a central NW core [73, 74, 75], are of particular significance amongst all NW heterostructures due to a) independent degrees of freedom of controlling the composition and the size of the core and the shells and b) the fact that the band offset across the radial heterostructure interface provides effective radial confinement[76] or separation[77] of carriers across the NW axis. And above all, the heteroepitaxial growth of III-V semiconductor core/shell or core/multishell heterostructures on silicon advances the integration of III-V semiconductors with silicon, making it cost-effective to utilize the special optical and electrical properties of III-V semiconductors on the mature silicon technology [78, 79].

Dilute nitride GaN_xP_{1x} alloy is a special semiconductor material. Our previous study shows that an incorporation of 0.5% of N into GaP changes the indirect bandgap to direct bandgap [35, 80]. The strong interaction of the N localized states and the GaP host extended states splits the conduction band into two sub-bands, i.e., E and E_+, with E being the fundamental bandgap [81]. Bi and Tu reported that up to 16% of N could be incorporated into GaP [82], which means that the

GaN_xP_{1x} bandgap is tunable from 1.22 eV to 2.15 eV, covering a wide range of the solar spectrum. Moreover, GaN_xP_{1x}/GaN_yP_{1y} heterostructure with x > y has a type-II stagger band alignment, where the built-in potential will automatically separate the photoinduced carriers across the heterostructure [83]. Therefore, growing GaN_xP_{1x}/GaN_yP_{1y} nanocrystal heterostructures on Si(111) substrate will be of particular interest regarding to photovoltaic applications. GaP NWs have been epitaxially grown on Si(111) [84]; however, GaP/GaN_xP_{1x} core/shell NWs have not been studied yet. In this letter, we are presenting the study on the epitaxial growth of vertical GaP/GaN_xP_{1x} core/shell NWs on Si(111).

All samples were grown in our Varian Gen-II MBE system modified to handle gas sources. Thermally cracked PH_3 at 1000 $°C$ and RF N plasma excited at 13.56 MHz were used for P and N sources, respectively. Solid elemental Ga was used to generate a Ga atomic beam through an effusion cell. The Si(111) substrate was dipped in an HF solution to remove the intrinsic oxide, resulting in a hydrogen-passivated surface [85]. The substrate was treated with ultrasonic bath cleaning in de-ionized water followed by nitrogen blow-dry. It was then immediately loaded into the load-lock chamber. Prior to growth, the Si substrate temperature T_{sub} was heated up to 750$°C$ to further clean the substrate thermally for 15 min. T_{sub} was subsequently lowered to 580$°C$ for the growth of GaP NW cores. Throughout the growth, the Ga flux was set at 0.8 monolayer/sec, calibrated by reflection high energy electron diffraction (RHEED) intensity oscillation [86] in the planar growth of GaP at the same substrate temperatures. The Ga shutter was opened for 5 sec to deposit Ga to form droplets as catalysts on the substrate surface. No extrinsic catalysts were used. PH_3 was injected into the growth chamber through a hydride injector, and both the Ga and P shutters were opened. The GaP NW cores were grown under the vapor-liquid-solid (VLS) mechanism [87] for 30 min with a V/III incorporation ratio of 1.5 [32] and at a substrate rotation speed of 5 RPM to ensure sample uniformity. The growth was then interrupted to ignite the N plasma and lower Tsub to 520$°C$. Lowering Tsub is also the same procedure for planar GaNP growth to increase N incorporation11. Moreover, decreasing Tsub and increasing V/III ratio reduces Ga adatoms mobility on the growth surface. A

large amount of Ga adatoms on the side wall of the already grown NWs will be kept from diffusing all the way to the Ga droplets on the NW tip, whichotherwise would contribute to the NW axial growth. Furthermore, higher V/III ratio lowers the heterogeneous activation energy. This decreases the mobility of Ga adatoms on the surface due to their relatively higher possibility of nucleation on the surface, which can further suppress the NW axial growth. However, it is worth noting that too high a V/III ratio could trigger faceted growth for dilute nitride, resulting in poor crystal quality [88]. Hence the shell layer was grown for another 30 min with a V/III incorporation ratio of 2.5 [32].

The scanning electron microscopy (SEM) images of the GaP NW cores (figure .2) show that uniform, vertical and straight GaP NWs were grown on the Si(111) substrate. The density of the GaP NWs ranges from 1×10^7 to $5 \times 10^8 cm^{-2}$ across the sample. On average, the GaP NWs are $\sim$ 2.3 μm long in axial length, which gives an axial growth rate of 78 nm/min. This is about six times as fast as the planar growth rate under the same growth condition. The typical diameter is $\sim$ 110 nm. The plan view SEM (figure .2 (b)) shows that these GaP NWs are hexagonal in shape, indicating that NWs were epitaxially grown following the Si(111) crystal orientation. Figure .3 shows SEM images of the GaP/GaNP core/shell NWs. There is no significant increase in the axial length ($\sim$ 0.2 μm increase on average), indicative of effective suppression of axial growth. On the contrary, the diameter of the NWs is doubled to $\sim$ 220 nm. Nevertheless, the radial growth rate in this case is only 1.8 nm/min, far less than the axial growth rate of the GaP NW core. The huge difference between the axial growth rate and the radial growth rate comes from the difference in the nature of the VLS growth and the step-mediated growth23. In VLS growth the Ga droplets serve as big nucleation collectors, where incoming adatoms can nucleate and incorporate into the NW once they are dissolved in the Ga droplets on the NW tip. On the other hand, in step-mediated growth Ga adatoms nucleate on step edges of which the number is limited on the side walls of the NWs, resulting in a much lower nucleation rate.

GaP NWs and GaP/GaNP core/shell NWs are distinguishable by their col-
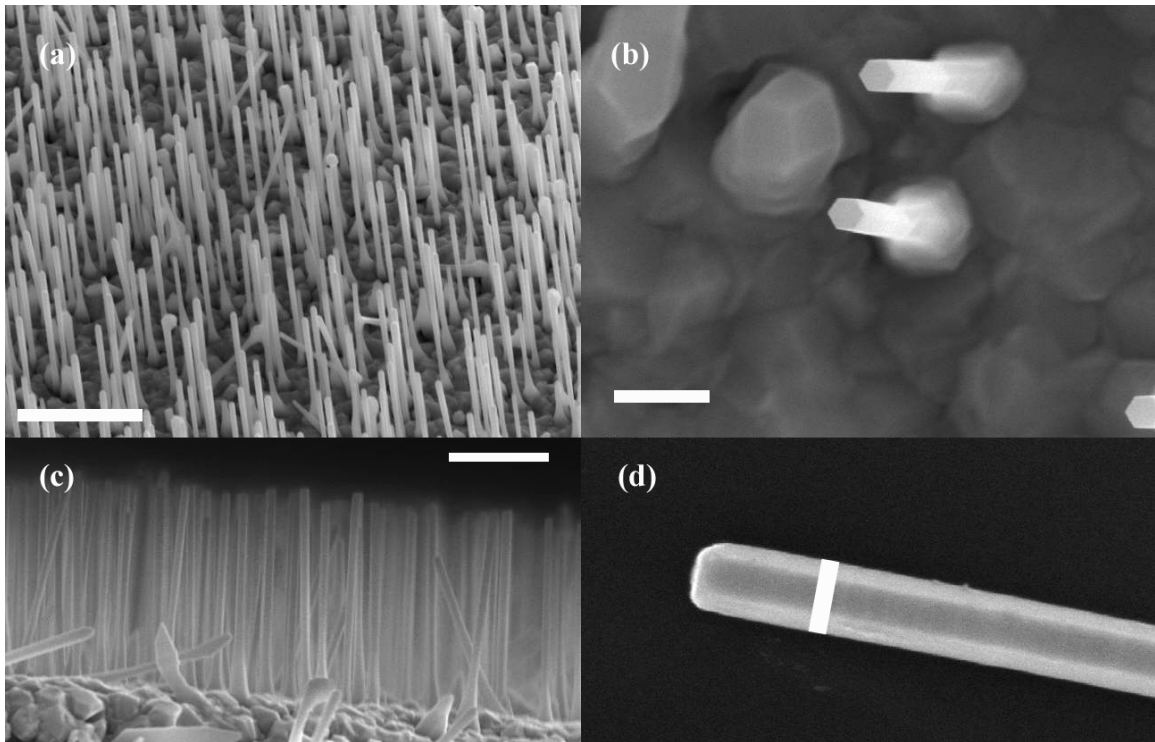
Figure .2: SEM images of GaP NWs on Si(111). (a) 45 ° tilted view. Scale bar: 2 m. (b) Plan view. Scale bar: 200 nm. (c) 90 ° side view. Scale bar: 1 μm. (d) A single GaP NW. Scale bar: 110 nm.
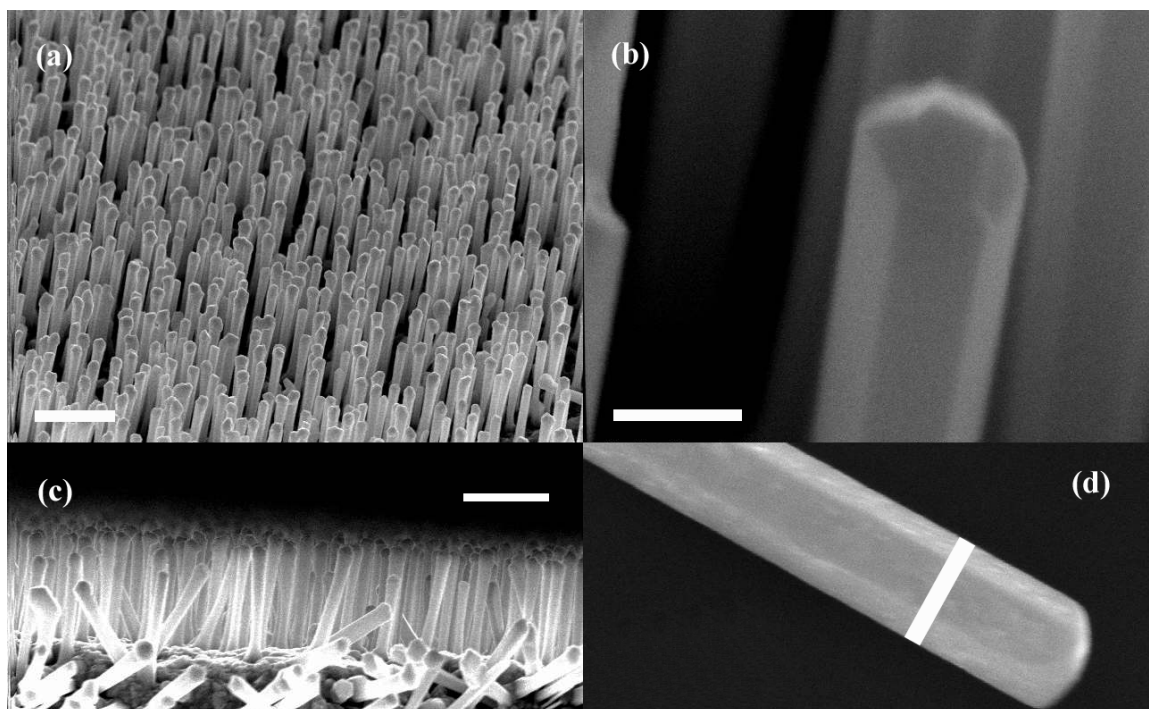
Figure .3: SEM images of GaP/GaNP core/shell NWs on Si(111). (a) 45 ° tilted view. Scale bar: 2 m. (b) 45 ° tilted view showing a core/shell NWs hexagon shape. Scale bar: 200 nm. (c) 90 ° side view. Scale bar: 2 μm. (d) A single GaP/GaNP NW. Scale bar: 220 nm.
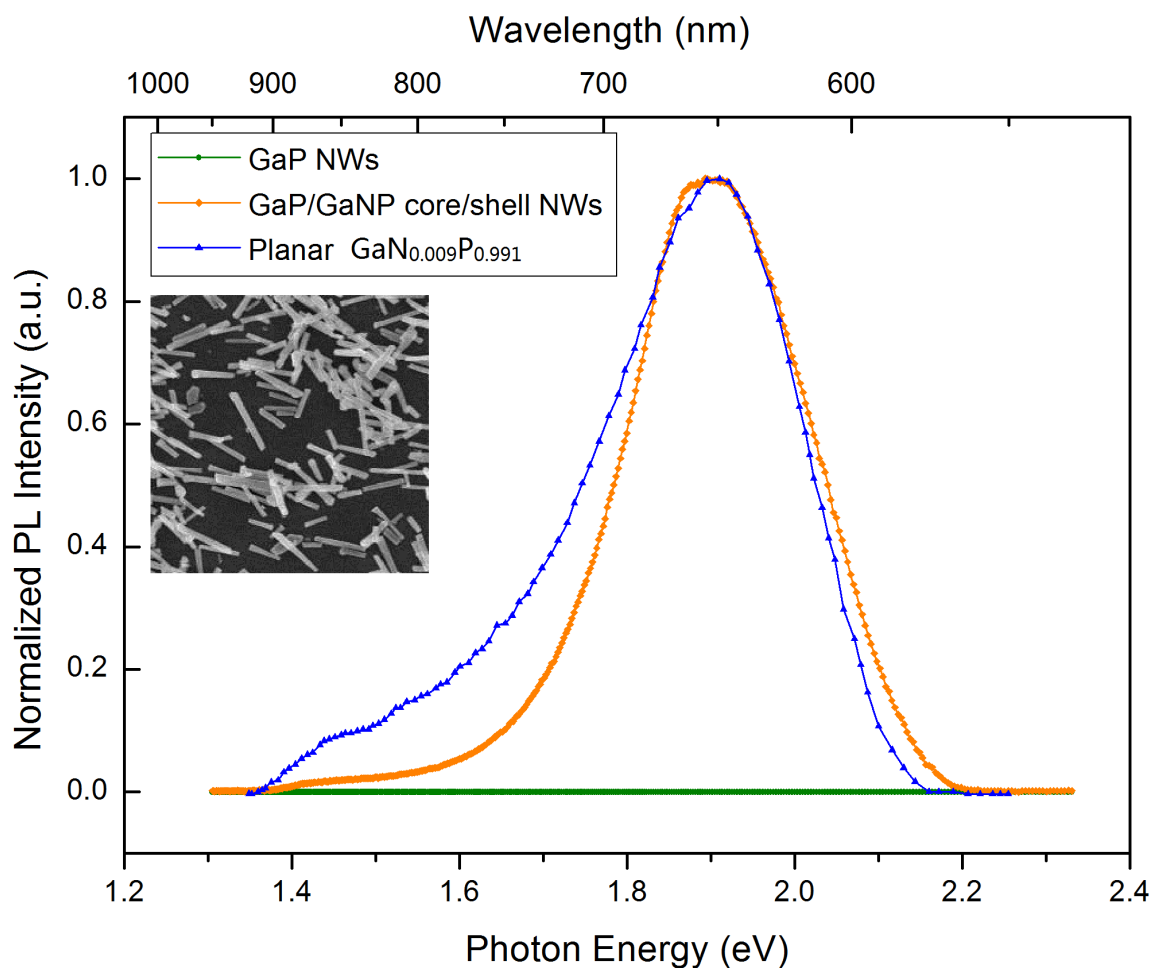
Figure .4: Room Temperature (300K) PL of GaP NW clusters (green curve) and GaP/GaNP core/shell NW clusters (orange curve). The blue curve, which shows larger band tail on the low-energy side, is from planar GaNP (Ref. [35]). Optical pumping: 500 mW, 532 nm semiconductor green laser. Inset: A 10 μm full scale SEM image of GaP/GaNP core/shell NWs after dry-transfer.

ors under naked eyes, with the former being green and the latter being orange due to nitrogen incorporation. To separate the NW photoluminescence (PL) signal from the planar layer underneath, the GaP NWs and the GaP/GaNP NWs were dry-transferred to a second Si substrate by sliding the grown sample on the second substrate face to face. A 532 nm semiconductor laser (500 mW) was collimated on a cluster of NWs (figure .4 inset) on the second substrate, from which the signal was dispersed through a SPEX 1870 spectrometer and collected by a Hamamatus R636-10 photomultiplier tube. No PL signal was seen on GaP NWs while GaP/GaNP core/shell NWs gave PL response at room temperature (Figure 3). Since P overpressure was provided and V/III ratio was kept larger than 1 throughout the growth process, no new Ga droplets were formed as new nucleation sites between and on already grown NWs during the switch from the NW core growth to the NW shell growth. Hence no new NW sites should exist. This is confirmed by the fact that after shell layer growth no NWs with smaller diameter and height or branches were seen (figure .3 (a) and (c)). Therefore, the room temperature PL signal along with the uniformity of NWs in diameter and height confirms the GaP/GaNP core/shell structure.

According to the band anti-crossing (BAC) model [81],the N content in the GaNP NW shell is $\sim$ 0.9% on average. Dilute nitride PL spectra peak widths are broad in general due to the newly formed bands nature as a convolution of all the nitrogen related bound states11. However, the large band tail on the low-energy side, usually conspicuous in room-temperature or even low-temperature PL of GaNP planar samples, is much reduced in the case of GaP/GaNP core/shell NWs. It is likely that nitrogen cluster related donorlike/acceptorlike deep centers are less formed during the growth of GaNP NW shell. This suggests that the impact of nitrogen incorporation on dilute nitride crystal quality is different for planar growth and NW growth and dilute nitride NWs are more likely to have better crystal quality.

In conclusion, we have epitaxially grown GaP NWs and GaP/GaNP core/shell NWs on Si(111) by GSMBE. From room-temperature PL data, N incorporated in the radial shell was determined to be $\sim$ 0.9% on average, according to the BAC

model. Growing GaNP into nanowire structure is a promising way to improve its crystal quality.

Materials in this chapter were partially published in *Appl. Phys. Lett.*, 100, 053108, (2013).

Bibliography

[1] *World energy resources and consumption*. Wikipedia.

[2] Martin A. Green. *Third Generation Photovoltaics: Advanced Solar Energy Conversion*. Springer, 2003.

[3] P. T. Landsberg and G. Tonge. Thermodynamic energy conversion efficiencies. *Journal of Applied Physics*, 51(7):R1–R20, 1980.

[4] William Shockley and Hans J. Queisser. Detailed balance limit of efficiency of pn junction solar cells. *Journal of Applied Physics*, 32(3):510–519, 1961.

[5] R. R. King, D. C. Law, K. M. Edmondson, C. M. Fetzer, G. S. Kinsey, H. Yoon, R. A. Sherif, and N. H. Karam. 40% efficient metamorphic GaInP/GaInAs/Ge multijunction solar cells. *Applied Physics Letters*, 90(18):183516, 2007.

[6] Masafumi Yamaguchi. Iiiv compound multi-junction solar cells: present and future. *Solar Energy Materials and Solar Cells*, 75(12):261 – 269, 2003.

[7] Antonio Luque and Antonio Marti. Increasing the efficiency of ideal solar cells by photon induced transitions at intermediate levels. *Physical Review Letters*, 78(26):5014–5017, 1997.

[8] I. Ramiro, A. Marti, E. Antolin, and A. Luque. Review of experimental results related to the operation of intermediate band solar cells. *Photovoltaics, IEEE Journal of*, 4(2):736–748, 2014.

[9] Gerd Keiser. *Optical Fiber Communications*. John Wiley and Sons, Inc., 2003.

[10] R Wyatt and WJ Devlin. 10 khz linewidth 1.5 μm ingaasp external cavity laser with 55 nm tuning range. *Electronics Letters*, 19(3):110–112, 1983.

[11] Jack L Jewell, YH Lee, JP Harbison, A Scherer, and LT Florez. Vertical-cavity surface-emitting lasers-design, growth, fabrication, characterization. *IEEE Journal of Quantum Electronics*, 27:1332–1346, 1991.

[12] Michael H MacDougal, P Daniel Dapkus, V Pudikov, Hanmin Zhao, and Gye Mo Yang. Ultralow threshold current vertical-cavity surface-emitting lasers with alas oxide-gaas distributed bragg reflectors. *Photonics Technology Letters, IEEE*, 7(3):229–231, 1995.

[13] Markus Weyers, Michio Sato, and Hiroaki Ando. Red Shift of Photoluminescence and Absorption in Dilute GaAsN Alloy Layers. *Japanese Journal of Applied Physics*, 31(Part 2, No. 7A):L853–L855, 1992.

[14] Masahiko Kondow, Shin'ichi Nakatsuka, Takeshi Kitatani, Yoshiaki Yazawa, and Makoto Okai. Room-temperature pulsed operation of gainnas laser diodes with excellent high-temperature performance. *Japanese Journal of Applied Physics*, 35(Part 1, No. 11):5711–5713, 1996.

[15] W. Shan, W. Walukiewicz, III Ager, J. W., E. E. Haller, J. F. Geisz, D. J. Friedman, J. M. Olson, and S. R. Kurtz. Band Anticrossing in GaInNAs Alloys. *Physical Review Letters*, 82(6):1221, 1999.

[16] J. R. Arthur. Molecular beam epitaxy. *Surface Science*, 500(1-3):189–217, 2002.

[17] Ayahiko Ichimiya and Philip I. Cohen. *Reflection high-energy electron diffraction*. Cambridge University Press, 2004.

[18] M. B. Panish and H. Temkin. Gas-source molecular-beam epitaxy. *Annual Review of Materials Science*, 19:209–229, 1989.

[19] J. M. Chauveau, Y. Androussi, A. Lefebvre, J. Di Persio, and Y. Cordier. Indium content measurements in metamorphic high electron mobility transistor structures by combination of x-ray reciprocal space mapping and transmission electron microscopy. *Journal of Applied Physics*, 93(7):4219–4225, 2003.

[20] B. Monemar and W. M. Chen. Electronic-structure of complex defects in semiconductors from luminescence perturbation spectroscopy. *Journal of Luminescence*, 40-1:59–63, 1988.

[21] Robert Kudrawiec and Jan Misiewicz. *Semiconductor Research: Experimental Techniques, Chapter 4 Optical Modulation Spectroscopy*. Springer, 2012.

[22] N. Lopez, L. A. Reichertz, K. M. Yu, K. Campman, and W. Walukiewicz. Engineering the electronic band structure for multiband solar cells. *Physical Review Letters*, 106(2):028701, 2011.

[23] Joel W Ager III, W Walukiewicz, and Kin Man Yu. Ultrahigh efficiency multiband solar cells final report for director's innovation initiative project dii-2005-1221. 2006.

[24] I. Vurgaftman, J. R. Meyer, and L. R. Ram-Mohan. Band parameters for iiiv compound semiconductors and their alloys. *Journal of Applied Physics*, 89(11):5815–5875, 2001.

[25] M. J. Seong, A. Mascarenhas, and J. F. Geisz. γ-x mixed symmetry of nitrogen-induced states in gaas1xnx probed by resonant raman scattering. *Applied Physics Letters*, 79(9), 2001.

[26] J. D. Perkins, A. Mascarenhas, J. F. Geisz, and D. J. Friedman. Conduction-band-resonant nitrogen-induced levels in $GaAs_{1-x}N_x$ with $x < 0.03$. *Phys. Rev. B*, 64:121301, 2001.

[27] J. Wu, W. Walukiewicz, K. M. Yu, J. W. Ager, E. E. Haller, Y. G. Hong, H. P. Xin, and C. W. Tu. Band anticrossing in GaNP alloys. *Phys. Rev. B*, 65:241303, 2002.

[28] J Wu, W Shan, and W Walukiewicz. Band anticrossing in highly mismatched IIIV semiconductor alloys. *Semiconductor Science and Technology*, 17(8):860, 2002.

[29] I. Vurgaftman and J. R. Meyer. Band parameters for nitrogen-containing semiconductors. *Journal of Applied Physics*, 94(6):3675–3696, 2003.

[30] J.W. Matthews and A.E. Blakeslee. Defects in epitaxial multilayers: I. misfit dislocations. *Journal of Crystal Growth*, 27(0):118 – 125, 1974.

[31] J. Simon, S. Tomasulo, P. J. Simmonds, M. Romero, and M. L. Lee. Metamorphic gaasp buffers for growth of wide-bandgap ingap solar cells. *Journal of Applied Physics*, 109(1):–, 2011.

[32] YanJin Kuang, San-Wen Chen, Hua Li, Sunil K. Sinha, and Charles Wuching Tu. Growth of GaNAsP alloys on GaP(100) by gas-source molecular beam epitaxy. *Journal of Vacuum Science and Technology B: Microelectronics and Nanometer Structures*, 30(2):02B121, 2012.

[33] Y. J. Kuang, K. M. Yu, R. Kudrawiec, A. V. Luce, M. Ting, W. Walukiewicz, and C. W. Tu. GaNAsP: An intermediate band semiconductor grown by gas-source molecular beam epitaxy. *Applied Physics Letters*, 102(11):112105–4, 2013.

[34] B. W. Liang and C. W. Tu. A kinetic model for as and p incorporation behaviors in gaasp grown by gas-source molecular beam epitaxy. *Appl. Phys. Lett.*, 74:255–259, 1993.

[35] H. P. Xin, C. W. Tu, Yong Zhang, and A. Mascarenhas. Effects of nitrogen on the band structure of GaN$_x$P$_{1-x}$ alloys. *Appl. Phys. Lett.*, 76(10):1267–1269, 2000.

[36] Masayuki Hata, Akiyoshi Watanabe, and Toshiro Isu. Surface diffusion length observed by in situ scanning microprobe reflection high-energy electron diffraction. *Journal of Crystal Growth*, 111(1-4):83–87, 1991.

[37] K. J. Bachmann and E. Buehler. Phase equilibria and vapor pressures of pure phosphorus and of the indium/phosphorus system and their implications regarding crystal growth of inp. *Journal of The Electrochemical Society*, 121(6):835–846, 1974.

[38] J. S. Sandhu and J. L. Reuter. Arsenic source vapor pressure kinetics and capsule diffusion. *IBM Journal of Research and Development*, 15(6):464–471, 1971.

[39] K. P. Lim, H. T. Pham, S. F. Yoon, C. Y. Ngo, and S. Tripathy. Effect of thermal annealing on properties of InSbN grown by molecular beam epitaxy. *Appl. Phys. Lett.*, 96:161903, 2010.

[40] C. Karcher, K. Jandieri, B. Kunert, R. Fritz, M. Zimprich, K. Volz, W. Stolz, F. Gebhard, S. D. Baranovskii, and W. Heimbrodt. Peculiarities of the photoluminescence of metastable Ga(N,As,P)/GaP quantum well structures. *Physical Review B*, 82(24):245309, 2010.

[41] I A Buyanova, W M Chen, and C W Tu. Defects in dilute nitrides. *Journal of Physics: Condensed Matter*, 16(31):S3027, 2004.

[42] F. Ishikawa, S. Fuyuno, K. Higashi, M. Kondow, M. Machida, H. Oji, J.-Y. Son, A. Trampert, K. Umeno, Y. Furukawa, and A. Wakahara. Direct observation of N-(group V) bonding defects in dilute nitride semiconductors using hard x-ray photoelectron spectroscopy. *Applied Physics Letters*, 98(12):121915, 2011.

[43] P. Pichanusakorn, Y. J. Kuang, C. J. Patel, C. W. Tu, and P. R. Bandaru. The influence of dopant journal article and carrier concentration on the effective mass and Seebeck coefficient of GaNxAs1-x thin films. *Applied Physics Letters*, 99(7):072114, 2011.

[44] Y. J. Kuang, S. Sukrittanon, H. Li, and C. W. Tu. Growth and photoluminescence of self-catalyzed GaP/GaNP core/shell nanowires on Si(111) by gas source molecular beam epitaxy. *Applied Physics Letters*, 100(5), 2012.

[45] K. M. Yu, W. Walukiewicz, J. W. Ager, D. Bour, R. Farshchi, O. D. Dubon, S. X. Li, I. D. Sharp, and E. E. Haller. Multiband GaNAsP quaternary alloys. *Appl. Phys. Lett.*, 88:092110, 2006.

[46] Pablo G. Linares, Antonio Marti, Elisa Antolin, Corrie D. Farmer, Inigo Ramiro, Colin R. Stanley, and Antonio Luque. Voltage recovery in intermediate band solar cells. *Solar Energy Materials and Solar Cells*, 98(0):240 – 244, 2012.

[47] Joel Irwin Gersten and Frederick William Smith. *The physics and chemistry of materials*. Wiley New York, 2001.

[48] S Fahy and EP OReilly. Intrinsic limits on electron mobility in dilute nitride semiconductors. *Applied physics letters*, 83(18):3731–3733, 2003.

[49] KM Yu, W Walukiewicz, J Wu, DE Mars, DR Chamberlin, MA Scarpulla, OD Dubon, and JF Geisz. Mutual passivation of electrically active and isovalent impurities. *Nature materials*, 1(3):185–189, 2002.

[50] Jingbo Li, Pierre Carrier, Su-Huai Wei, Shu-Shen Li, and Jian-Bai Xia. Mutual passivation of donors and isovalent nitrogen in gaas. *Physical review letters*, 96(3):035505, 2006.

[51] A Janotti, P Reunchan, S Limpijumnong, and CG Van de Walle. Mutual passivation of electrically active and isovalent impurities in dilute nitrides. *Physical review letters*, 100(4):045505, 2008.

[52] YG Chai, R Chow, and CEC Wood. The effect of growth conditions on si incorporation in molecular beam epitaxial gaas. *Applied Physics Letters*, 39(10):800–803, 1981.

[53] Y. Jin, R. M. Jock, H. Cheng, Y. He, A. M. Mintarov, Y. Wang, C. Kurdak, J. L. Merz, and R. S. Goldman. Influence of n interstitials on the electronic properties of gaasn alloys. *Applied Physics Letters*, 95(6):–, 2009.

[54] F Ishikawa, G Mussler, K-J Friedland, H Kostial, K Hagenstein, L Daweritz, and KH Ploog. Impact of n-induced potential fluctuations on the electron transport in ga (as, n). *Applied Physics Letters*, 87(26):262112–262112, 2005.

[55] WG Bi, F Deng, SS Lau, and CW Tu. High resolution x-ray diffraction studies of algap grown by gas-source molecular-beam epitaxy. *Journal of Vacuum Science & Technology B*, 13(2):754–757, 1995.

[56] M Heiblum, WI Wang, LE Osterling, and V Deline. Heavy doping of gaas and algaas with silicon by molecular beam epitaxy. *Journal of applied physics*, 54(11):6751–6753, 1983.

[57] RJ Malik, J Nagle, M Micovic, T Harris, RW Ryan, and LC Hopkins. Doping limits of c, be, and si in gaas grown by solid source molecular-beam epitaxy with a thermally cracked as2 source. *Journal of Vacuum Science & Technology B*, 10(2):850–852, 1992.

[58] Masaki Ogawa and Toshio Baba. Heavily si-doped gaas and alas/n-gaas super-lattice grown by molecular beam epitaxy. *Japanese journal of applied physics*, 24(8):L572–L574, 1985.

[59] P. Pichanusakorn, Y. J. Kuang, C. Patel, C. W. Tu, and P. R. Bandaru. Feasibility of enhancing the thermoelectric power factor in ganas. *Physical Review B*, 86(8), 2012.

[60] G Bösker, NA Stolwijk, JV Thordson, U Södervall, and TG Andersson. Diffusion of nitrogen from a buried doping layer in gallium arsenide revealing the prominent role of as interstitials. *Physical review letters*, 81(16):3443, 1998.

[61] E. Fred Schubert. *Doping in III-V semiconductors*. Cambridge University Press, 1993.

[62] Hopkins C. G. Evans C. A. Jr. Drummond T. J. Lyons W. G. Klem J. Colvard C. Fisher, R. and H. Morkoc, 1983.

[63] WM McGee, PA Bone, RS Williams, and TS Jones. Atomic scale morphology of thin ganas films: Effects of nitrogen content and growth temperature. *Applied Physics Letters*, 87(18):181905–181905, 2005.

[64] M Reason, NG Rudawski, HA McKay, X Weng, W Ye, and RS Goldman. Mechanisms of gaasn growth: Surface and step-edge diffusion. *Journal of applied physics*, 101(8):083520, 2007.

[65] Weiming Wang, Albert S. Lin, and Jamie D. Phillips. Intermediate-band photovoltaic solar cell based on znte:o. *Applied Physics Letters*, 95(1):011103, 2009.

[66] Tooru Tanaka, Masaki Miyabara, Yasuhiro Nagao, Katsuhiko Saito, Qixin Guo, Mitsuhiro Nishio, M Yu Kin, and Wladek Walukiewicz. Photocurrent induced by two-photon excitation in znteo intermediate band solar cells. *Applied Physics Letters*, 102(5):052111, 2013.

[67] J Schone, E Spiecker, F Dimroth, AW Bett, and W Jager. Misfit dislocation blocking by dilute nitride intermediate layers. *Applied Physics Letters*, 92(8):081905–081905, 2008.

[68] Yuxin Song, Shumin Wang, Zonghe Lai, and Mahdad Sadeghi. Enhancement of optical quality in metamorphic quantum wells using dilute nitride buffers. *Applied Physics Letters*, 97(9):091903, 2010.

[69] Jordan R Lang, Joseph Faucher, Stephanie Tomasulo, Kevin Nay Yaung, and Minjoo Larry Lee. Comparison of gaasp solar cells on gap and gap/si. *Applied Physics Letters*, 103(9):092102, 2013.

[70] J. Xiang, W. Lu, Y. J. Hu, Y. Wu, H. Yan, and C. M. Lieber. Ge/si nanowire heterostructures as high-performance field-effect transistors. *Nature*, 441(7092):489–493, 2006.

[71] Xiangfeng Duan, Yu Huang, Ritesh Agarwal, and Charles M. Lieber. Single-nanowire electrically driven lasers. *Nature*, 421(6920):241–245, 2003.

[72] Carl J. Barrelet, Andrew B. Greytak, and Charles M. Lieber. Nanowire photonic circuit elements. *Nano Lett.*, 4(10):1981–1985, 2004.

[73] Lincoln J. Lauhon, Mark S. Gudiksen, Deli Wang, and Charles M. Lieber. Epitaxial core-shell and core-multishell nanowire heterostructures. *Nature*, 420(6911):57–61, 2002.

[74] Niklas Sköld, Lisa S. Karlsson, Magnus W. Larsson, Mats-Erik Pistol, Werner Seifert, Johanna Trögårdh, and Lars Samuelson. Growth and optical properties of strained gaas-gaxin1-xp core-shell nanowires. *Nano Lett.*, 5(10):1943–1947, 2005.

[75] O. Hayden, A. B Greytak, and D. C Bell. Core-shell nanowire light-emitting diodes. *Adv. Mater.*, 17(6):701–704, 2005.

[76] Wei Lu, Jie Xiang, Brian P. Timko, Yue Wu, and Charles M. Lieber. One-dimensional hole gas in germanium/silicon nanowire heterostructures. *Proceedings of the National Academy of Sciences of the United States of America*, 102(29):10046–10051, 2005.

[77] Sandeep Kumar, Marcus Jones, Shun?S Lo, and Gregory?D Scholes. Nanorod heterostructures showing photoinduced charge separation. *Small*, 3(9):1633–1639, 2007.

[78] S. F. Fang, K. Adomi, S. Iyer, H. Morkoc, H. Zabel, C. Choi, and N. Otsuka. Gallium arsenide and other compound semiconductors on silicon. *J. Appl. Phys.*, 68(7):R31–R58, 1990.

[79] Thomas Måtensson, C. Patrik T. Svensson, Brent A. Wacaser, Magnus W. Larsson, Werner Seifert, Knut Deppert, Anders Gustafsson, L. Reine Wallenberg, and Lars Samuelson. Epitaxial III-V Nanowires on Silicon. *Nano Lett.*, 4(10):1987–1990, 2004.

[80] I. A. Buyanova, G. Pozina, J. P. Bergman, W. M. Chen, H. P. Xin, and C. W. Tu. Time-resolved studies of photoluminescence in GaN_xP_{1-x} alloys: Evidence for indirect-direct band gap crossover. *Appl. Phys. Lett.*, 81(1):52–54, 2002.

[81] W. Shan, W. Walukiewicz, K. M. Yu, J. Wu, J. W. Ager III, E. E. Haller, H. P. Xin, and C. W. Tu. Nature of the fundamental band gap in ganp alloys. *Appl. Phys. Lett.*, 76(22):3251–3253, 2000.

[82] W. G. Bi and C. W. Tu. N incorporation in GaP and band gap bowing of GaN_xP_{1-x}. *Appl. Phys. Lett.*, 69(24):3710–3712, 1996.

[83] Sungjee Kim, Brent Fisher, Hans-Jürgen Eisler, and Moungi Bawendi. Type-II Quantum Dots: CdTe/CdSe(Core/Shell) and CdSe/ZnTe(Core/Shell) Heterostructures. *J. Am. Chem. Soc.*, 125(38):11466–11467, 2003.

[84] P. K. Mohseni, C. Maunders, G A Botton, and R R LaPierre. Gap/gaasp/gap corecmultishell nanowire heterostructures on (111) silicon. *Nanotechnology*, 18(44):445304, 2007.

[85] D. B. Fenner, D. K. Biegelsen, and R. D. Bringans. Silicon surface passivation by hydrogen termination: A comparative study of preparation methods. *J. Appl. Phys.*, 66(1):419–424, 1989.

[86] J. H. Neave, B. A. Joyce, P. J. Dobson, and N. Norton. Dynamics of film growth of GaAs by MBE from Rheed observations. *Appl. Phys. A: Materials Science & Processing*, 31(1):1–8, 1983.

[87] R. S. Wagner and W. C. Ellis. Vapor-liquid-solid mechanism of single crystal growth. *Appl. Phys. Lett.*, 4(5):89–90, 1964.

[88] M. Adamcyk, S. Tixier, B. J. Ruck, J. H. Schmid, T. Tiedje, V. Fink, M. Jeffries, D. Karaiskaj, K. L. Kavanagh, and M. Thewalt. Faceting transition in epitaxial growth of dilute GaNAs films on GaAs. *J. Vac. Sci. & Tech. B*, 19:1417–1421, 2001.